

The Use of Anionic and Cationic Clays in Adsorption Processes and its Potential Applications

Lead Guest Editor: Juan A. Cecilia

Guest Editors: Francisco Franco Duro and Enrique Vilarrasa-García



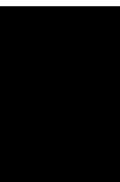


The Use of Anionic and Cationic Clays in Adsorption Processes and its Potential Applications

**The Use of Anionic and Cationic Clays in
Adsorption Processes and its Potential
Applications**

Lead Guest Editor: Juan A. Cecilia

Guest Editors: Francisco Franco Duro and Enrique
Vilarrasa-García



Copyright © 2023 Hindawi Limited. All rights reserved.

This is a special issue published in "Adsorption Science & Technology" All articles are open access articles distributed under the Creative Commons Attribution License, which permits unrestricted use, distribution, and reproduction in any medium, provided the original work is properly cited.

Chief Editor

Ashleigh J. Fletcher , United Kingdom


Academic Editors

Chinenye Adaobi Igwegbe , Nigeria
Adrián Bonilla-Petriciolet, Brazil
Mohammad Hadi Dehghani, Iran
Tony Hadibarata, Malaysia
Ming Hua, China
Muhammad Raziq Rahimi Kooh, Brunei
Darussalam
Monoj Kumar Mondal , India
George Kyzas, Greece
MU NAUSHAD, Saudi Arabia
Hai Nguyen Tran , Vietnam
Walid Oueslati , Tunisia
Szabolcs Pap , United Kingdom
Sami-Ullah Rather , Saudi Arabia
Anjani Ravi Kiran Gollakota , Taiwan
Eloy S. Sanz P rez , Spain
Stefano Salvestrini , Italy
N. Selvaraju , India
Rangabhashiyam Selvasembian , India
P. Senthil Kumar , India
Lingzhi Yang , China

Advisory Board Member(s)



Contents

Partial Purification of Anthocyanins (*Brassica oleracea* var. *Rubra*) from Purple Cabbage Using Natural and Modified Clays as Adsorbent

Darlyson Tavares Guimarães, Liana Maria Ramos Mendes, Luiz Bruno de Sousa Sabino, Edy Sousa de Brito, Enrique Vilarrasa-García, Enrique Rodríguez-Castellón, Juan Antonio Cecilia , and Ivanildo José da Silva Junior

Review Article (14 pages), Article ID 2724122, Volume 2023 (2023)

Adsorption Study and Removal of Basic Fuchsin Dye from Medical Laboratory Wastewater Using Local Natural Clay

Fuad Hama Sharif Radha, Dler M. S. Shwan , and Stephan Kaufhold 




Research Article (13 pages), Article ID 9398167, Volume 2023 (2023)

Mesoscopic Process Simulation of In Situ Leaching of Ionic Rare Earth Based on NMRI Technology

Fuyu Wu , Dan Wang , Yunzhang Rao , Meidao Zhang, Liang Shi , Min Han, and Wei Xu

Research Article (13 pages), Article ID 8348431, Volume 2023 (2023)

Adsorption of Arsenic, Lead, Cadmium, and Chromium Ions from Aqueous Solution Using a Protonated Chabazite: Preparation, Characterization, and Removal Mechanism

Laura Alejandra Pinedo-Torres, Adrián Bonilla-Petriciolet , María Elena García-Arreola , Yenetzi Villagrana-Pacheco, Ana G. Castañeda-Miranda, and María Selene Berber-Mendoza 

Research Article (21 pages), Article ID 2018121, Volume 2023 (2023)

Review Article

Partial Purification of Anthocyanins (*Brassica oleracea* var. *Rubra*) from Purple Cabbage Using Natural and Modified Clays as Adsorbent

Darlyson Tavares Guimarães,^{1,2} Liana Maria Ramos Mendes,^{1,2}
Luiz Bruno de Sousa Sabino,¹ Edy Sousa de Brito,² Enrique Vilarrasa-García,¹
Enrique Rodríguez-Castellón,³ Juan Antonio Cecilia ³ and Ivanildo José da Silva Junior¹

¹Department of Chemical Engineering, Universidade Federal do Ceará, Av. Mister Hull, 2977, Campus Universitário do Pici, Fortaleza, Ceará 60356-000, Brazil

²Embrapa Tropical Agroindustry, R. Dra Sara Mesquita, 2270, Fortaleza, Ceará 60511-110, Brazil

³Department of Inorganic Chemistry, Crystallography and Mineralogy, Faculty of Sciences, Universidad de Málaga, Campus of Teatinos, 29071 Málaga, Spain

Correspondence should be addressed to Juan Antonio Cecilia; jacecilia@uma.es

Received 16 January 2023; Revised 2 August 2023; Accepted 29 November 2023; Published 13 December 2023

Academic Editor: Senthil Kumar Ponnusamy

Copyright © 2023 Darlyson Tavares Guimarães et al. This is an open access article distributed under the Creative Commons Attribution License, which permits unrestricted use, distribution, and reproduction in any medium, provided the original work is properly cited.

This research is aimed at evaluating strategies for the adsorption and recovery of anthocyanins present in purple cabbage using natural and modified clays as adsorbent. In the batch adsorption experiments, the anthocyanin extracts were put in contact with the adsorbents, and different parameters were evaluated to determine the best conditions for their adsorption and recovery. It was noted that the highest levels of adsorption (28.0 mg g^{-1}) occurred using a porous clay heterostructure (PCH) material as adsorbent, with a mass of 25 mg and 120 min of contact. Under the same conditions, the sepiolite only presented an adsorption capacity of 14.0 mg g^{-1} . The desorption results showed that the 60% methanolic solution recovered 60% of the anthocyanins adsorbed on PCH, while the 80% ethanolic solution recovered 35% of those adsorbed on sepiolite. The eluted anthocyanin solutions showed a 98% lower sugar concentration than the crude extract, indicating the low affinity of the adsorbents for sugars. Six types of acylated cyanidins were identified via UPLC-QToF-MSE in the extract, and it was confirmed from the FTIR analyses that the highest affinity of the clays occurred with the anthocyanins that presented more organic acid in their structure. The results show that PCH and sepiolite have high selectivity for anthocyanins and low affinity for the sugars present in the plant extract, facilitating the process of partial purification and application of these pigments.

1. Introduction

Anthocyanins (ACNs) are flavonoids widely distributed in nature, being responsible for the color of different flowers, fruits, and leaves, and also acting to protect the plant. Due to their variety of colors and recognized biological actions (e.g., antioxidant, anticancer, and anti-inflammatory actions), there is scientific interest in applying ACNs in several biomedical and technological applications [1]. Nowa-

days, the industrial applications of ACNs are limited, basically, by two factors. The absence of available and cheap substrates for their extraction and their marked instability to processing conditions, such as light, oxygen, and high temperatures, which can result in a loss of color. As a potential alternative, acylated ACNs are known to be a class of these pigments that display natural stability, presenting interesting potential for the industry. In this research, purple cabbage (*Brassica oleracea* var. *Rubra*) was used as a substrate for

the extraction of ACNs, which, beyond being an available and cheap raw material, presents in its constitution different types of acylated ACNs [2].

Depending on the application, purified ACN extracts are required, since the presence of coextracted substances, such as sugars and organic acids, can lead to pigment degradation [3]. Several techniques have been used to obtain purified ACNs. Thus, purification methods range from simple alternatives, such as solid-phase extraction (SPE) and liquid-liquid extraction, to the use of more sophisticated chromatographic techniques, such as countercurrent chromatography (CCC) and medium pressure liquid chromatography [4]. Generally, these methods exhibited unsatisfactory performance or make the process more complex and expensive. Adsorption is a widely used separation method due to its simplicity and economic viability [5].

To achieve a sustainable and competitive process, it is necessary to search for and develop materials that attain a good adsorption capacity and, in turn, are economically viable. Focusing on the ACN adsorption, synthetic and natural adsorbents such as ion-exchange resins [6, 7], commercial clay Tonsil Terrana 580FF [5, 8], and coal obtained from the Pequi bark [9] were previously reported for the purification of ACNs. Among them, natural clays can be highlighted due to their high availability on the earth's surface, low cost, and high versatility to modify their physicochemical properties, improving adsorption capacity [10, 11].

Among the raw clays, fibrous clays such as attapulgite (ATA) or sepiolite (SEP) have been extensively studied in adsorption processes due to their interesting fibrous morphology with high microporosity in their fibers because of the inversion of the tetrahedral sheet of the clay [12]. This results in a material with low density and high specific surface area [12–14]. Smectites are other phyllosilicates of great interest to the scientific community due to the charge deficiency of these phyllosilicates in their sheets, which must be counterbalanced with the presence of cations in the interlayer space. This fact encourages that smectites show a good trend in exchanging cations located in the interlayer space as well as hosting other cations or organic molecules in their interlaminar space, in such a way that make these phyllosilicates of great interest in the field of adsorption [11, 12]. The ability to exchange interlayer spaced alkaline or alkaline-earth cations by bulkier cations, as substitute bulkier cations in the interlayer space, promotes the incorporation of bulky polyoxocations or organic cations, which can be used to form pillared clays, improving textural properties of the clays substantially [11, 15].

Among the possible pillared clays, porous clay heterostructures (PCHs) have emerged as interesting materials for adsorption and catalytic processes [11, 16–19]. PCH synthesis was first described by Galarneau et al. in 1995 [16]. In this synthesis, a smectite is treated with a bulky organic cation solution to expand the interlayer space. After removing the nonintercalated organic cation, a silicon alkoxide is added to the mother solution, which polymerizes around the cation between adjacent sheets. Finally, the obtained gel is calcined to remove the organic cation, obtaining a porous material, which displays great porosity and high

thermal stability, as well as high potential in the fields of adsorption and catalysis [11, 17].

Considering the importance of obtaining purified ACN extracts for their application as antioxidant, anticancer, or anti-inflammatory actions, through a simple and less expensive process such as adsorption, this study is aimed at evaluating the best conditions for the purification of ACNs extracted from purple cabbage using inexpensive adsorbents, such as natural and modified clays. The originality of this work lies in the study of several clay minerals in the present research that have not yet been evaluated in adsorption processes of ACNs. In addition, the study of PCHs in ACN purification processes has not been evaluated either. On the other hand, this manuscript is not limited to carrying out adsorption studies, since another goal of this study is the desorption of ACNs for subsequent valorization, as well as the quantification of adsorbed sugars and the possible determination of the ACN adsorbent.

2. Materials and Methods

2.1. Chemical Reagents. Ethanol (96 vol.%), acetone, methanol, and trifluoroacetic acid were obtained from Sigma-Aldrich (Saint Louis, USA), HPLC grade. Acetonitrile and methanol from J.T.Baker (Pennsylvania, USA) were reagent grade, while the purity of H₂O was Milli-Q grade (Millipore Lab., Bedford, MA).

The natural fibrous clays (sepiolite and attapulgite) were provided by TOLSA. Bentonite was obtained from La Serrata de Nijar deposits located in the southeast of Spain [20]. PCH was synthesized from the bentonite sample [21].

2.2. Synthesis of the Porous Clay Heterostructures. The porous clay heterostructures (PCHs) were synthesized following the methodology described by Cecilia et al. with some modifications [11, 21]. 2.5 g of bentonite remained under stirring with 1 M NaCl solution for 1 day. Then, the homoionic bentonite underwent a cationic exchange with an excess bulky cation (9 g of cetyltrimethylammonium bromide in 100 mL of 1-propanol for 3 days). In the next step, the expanded bentonite was filtered and washed with H₂O to remove the excess cetyltrimethylammonium bromide, and then, the sample was resuspended in 250 mL of H₂O for 1 day. After that, 0.9 g of hexadecylamine was dissolved in 25 mL of 1-propanol and added dropwise into the mother solution, maintaining the stirring for 1 day. After this time, a solution of 12 mL of tetraethyl orthosilicate (TEOS), as a silicon source, dissolved in 12 mL of 1-propanol was added dropwise into the mother solution, maintaining this stirring for 3 days. Then, the gel was filtered and washed, and finally, the solid was dried at 80°C overnight and calcined at 550°C for 6 h to remove the organic template, forming a porous structure.

2.3. Characterization Techniques. X-ray powder diffraction (XRD) patterns have been performed on an automated X'Pert Pro MPD diffractometer (Malvern Panalytical, United Kingdom) with a primary monochromator Ge (111) (strictly monochromatic Cu K α 1 radiation) and an X'Celerator (real-time multiple strip) detector. The powder

profiles were recorded between 2° and 70° in 2θ with a total measuring time of 30 min and at a scanning rate of $2^\circ/\text{min}$.

The morphology of the clays was determined by Transmission Electron Microscopy (TEM) in an FEI Talos F200X equipment supplied by Thermo Fisher Scientific (USA). This equipment combines outstanding high-resolution STEM and TEM imaging. The samples were dispersed in ethanol, and a drop of the suspension was put on a Cu grid (300 mesh).

The textural properties were determined from their N_2 adsorption-desorption isotherms at -196°C , using an ASAP 2020 Micromeritics equipment (USA). In a prior step to the analysis, the samples were outgassed at 200°C and a pressure of 10^{-4} mbar overnight. The specific surface area was determined by the BET method, with a N_2 molecule cross-section of 16.2 \AA^2 [22]. The pore size and micropore size distributions were determined by the DFT [23] and MP methods [24], respectively.

The characterization of the clays, before and after the adsorption and after the desorption processes, was evaluated by Fourier Transform Infrared Spectroscopy (FTIR). The samples were prepared in KBr tablets (2 mg of sample + 200 mg of dry KBr) and were analyzed in a Shimadzu FTIR 8300 spectrometer (Japan), in the range 500 to 4000 cm^{-1} .

2.4. Starting Plant. The purple cabbage was obtained from local trade in Fortaleza (Ceará, Brazil), manually cut and freeze-dried in a Labconco Freeze Dry-5 dryer (Labconco, MO) under pressure of 0.6 Pa for 48 h. After drying, the sample was crushed in a domestic blender and sieved on a $700 \mu\text{m}$ mesh to obtain a powder. The purple cabbage powder was stored (-5°C) in polyethylene bottles until the moment of analysis.

2.5. Anthocyanin Extraction. For ACN extraction, 10 g of purple cabbage was treated with a solution composed of 27 mL of ethanol (80% vol.) and 3 mL of trifluoroacetic acid. The mixture was sonicated (USC-1400; standard ultrasonic frequency of 40 kHz and real power of 135 W) for 20 min, and this process was repeated until the residue was colorless. The extracts obtained were mixed and concentrated at 40°C in a rotavapor R-215 (Bunch, Flawil, Switzerland) under reduced pressure. The crude extract was stored in glass bottles at -5°C until the moment of analysis.

2.6. Anthocyanin Quantification. The quantification of ACNs present in powdered cabbage was performed according to Do et al. [25]. The extracts were solubilized in a potassium chloride buffer (pH 1.0) and sodium acetate (pH 4.5) and read on a BioMate 3 UV-VIS spectrophotometer (Thermo Scientific, USA) in quartz cuvettes (1 mL) at 520 and 700 nm. The buffers were used as blanks. Total anthocyanins (AntT), expressed as a cyanidin-3-glucoside equivalent, were obtained according to the following equation.

$$\text{AntT} = \frac{A \times \text{MM} \times \text{FD} \times 1000}{\epsilon \times l}, \quad (1)$$

where A is the absorbance (for differential pH $A = [(A_{520\text{nm}} - A_{700\text{nm}})_{\text{pH } 1.0} - (A_{520\text{nm}} - A_{700\text{nm}})_{\text{pH } 4.5}]$), MM is the molar mass (449.2 g/mol for cyanidin-3-glucoside), FD is the dilution factor, and ϵ is the extinction coefficient (26900 L/mol/cm). These reading procedures were performed for all samples and at all stages of the experiments.

2.7. Determination of the Point of Zero Charge (pH_{PZC}). The determination of the point of zero charge (pH_{PZC}) of the clays was based on 11 experimental points, as was previously described by Schreider and Regalbuto and Regalbuto and Robles [26, 27]. For these studies, 25 mL of a 0.01 M NaCl solution was distributed in 10 beakers, in which the pH was adjusted in the range of 2 to 11 with hydrochloric acid (HCl) or sodium hydroxide (NaOH). Sequentially, 25 mg of each clay was dispersed in NaCl solutions and kept for 48 h. Finally, the pH of each beaker was measured, and the difference between the initial pH and the final pH was plotted.

2.8. Static Adsorption Experiments. The optimization of the conditions for the ACN adsorption process in natural and modified clays was carried out using batch experiments, at a constant temperature of 22°C . Adsorption studies were performed in a Tecnal rotary agitator (model TE-165, Brazil) at 121 rpm. The ACN extracts and clays were mixed in Falcon tubes (15 mL), and the data were obtained from the contact according to the time defined for each test. At the end of each test, the extracts were separated from the adsorbents using a CT-15000R refrigerated centrifuge (CIENEC, Brazil) for 10 min at 2540 rpm, and the ACN content was quantified (Equation (1)). Equation (2) was used to calculate the adsorption capacity per gram of adsorbent ($\text{mg}\cdot\text{g}^{-1}$):

$$q = \frac{V \times (C_i - C_f)}{m}, \quad (2)$$

where C_i and C_f are the initial and final concentrations in the liquid extract, respectively; q ($\text{mg}\cdot\text{g}^{-1}$) is the amount of ACN adsorbed on the solid phase; m (g) is the mass of adsorbent; and V (mL) is the volume of the sample solution.

For the selection of the most suitable clay for the ACN adsorption, 10 mg of each adsorbent was dispersed in 10 mL of the ACN extract, while remaining under agitation for 3 hours at 22°C . After the test, the ACNs were quantified, and the amount adsorbed was calculated according to Equation (2).

Once the clays with the highest adsorption capacity were selected, the mass of adsorbent was optimized. From 10 to 100 mg of each clay was weighed, which was kept in contact with 10 mL of the ACN extract for 3 hours. At the end of the test, the adsorbed ACNs were quantified according to Equation (2).

To determine the amount adsorbed, 25 mg of each clay (mass optimized) was dispersed in 10 mL of extract. Aliquots of supernatant were collected at regular intervals (0, 1, 3, 5, 10, 20, 30 min, and every 30 min until 3 h). The amount of

adsorbed ACNs was determined according to Equation (2), and after each reading, the pH was monitored using a DM-22 pH meter (Digimed, Brazil) to evaluate the influence of pH on the adsorption process. All adsorption experiments were performed at least three times, and no significant deviations (<5%) were observed.

2.9. Static Desorption Experiments. Desorption tests were performed with the following methodology. After ensuring that the adsorption equilibrium was reached, the clays loaded with ACNs were washed with 30 mL of water and then desorbed with 10 mL of ethanol 80% (0.1% v/v HCl). The tests were performed on a rotary shaker at a constant speed, according to the time determined for each experiment. After each test, the eluted samples were separated from the clays by centrifugation (10 min at 2540 rpm) and analyzed in a spectrophotometer. The percentage of desorption capacity ACNs was calculated using the mass balance presented in the following equation.

$$\% \text{desorption} = \frac{C_{\text{desorption}}}{C_{\text{initial}} - C_{\text{adsorption}}} \times 100, \quad (3)$$

where C_{initial} , $C_{\text{adsorption}}$, and $C_{\text{desorption}}$ are the concentrations of anthocyanins at the beginning, after adsorption, and after desorption, respectively.

2.9.1. Kinetic Study of the Desorption Process. For the kinetic study of the desorption of the ACNs, 10 mL of 80% (v/v) ethanol was used to perform the desorption of the ACNs. 2 mL aliquots of the solution were removed at regular intervals from 30 to 240 min to assess when the desorption process reached equilibrium. The amount of ACNs desorbed was determined by UV-visible and calculated according to Equation (3).

2.9.2. Evaluation of the Eluent. In order to evaluate the most suitable eluent for the ACN desorption, aqueous solutions of ethanol and methanol (60, 80, and 90% v/v), acidified with HCl (0.1% v/v) or not, were tested. The clays were loaded with ACNs, and the solvents were kept under constant agitation for 120 min, as determined in the previous test (Section 2.9.1). The amount of ACNs desorbed was calculated according to Equation (3).

2.10. Quantification of Sugars. Total sugars were quantified in the supernatants after adsorption and desorption tests using the phenol-indole method, as described by Dubois et al. [28]. 0.5 mL of each extract was reacted with 0.5 mL of 5% (v/v) phenol solution and 2.5 mL of H_2SO_4 . After 15 minutes of incubation, the samples were placed in quartz cuvettes and read in a spectrophotometer at 490 nm. Ultra-pure water was used as a blank. Quantification was performed using a glucose standard curve, and the results were expressed in mg L^{-1} .

2.11. Analysis of Anthocyanins by HPLC-MS/MS. The ACN extract was characterized by mass spectrometry in a chromatographic system ACQUITY UPLC (Waters, USA), coupled to a Quadrupole Time-of-Flight system (QToF,

Waters). The chromatographic runs were performed on a chromatographic column Waters ACQUITY UPLC BEH (150×2.1 mm, $1.7 \mu\text{m}$) under the following conditions: fixed temperature of 40°C , mobile phase of water with 0.1% formic acid (A) and acetonitrile with 0.1% formic acid (B), gradient ranging from 2% to 95%B (21 min), flow of 0.4 mL min^{-1} , and injection volume of $5 \mu\text{L}$. High-resolution mass conditions using a Xevo QToF in positive mode (ESI^+) were acquired in the range of 110-1180 Da, fixed source temperature of 120°C , desolvation temperature of 350°C , flow rate of 500 L h^{-1} , and capillary voltage of 3.2 kV. Leucine enkephalin was used as a *lock mass*. The acquisition mode was MS^E . The instrument was controlled by MassLynx software 4.1 (Waters Corporation, USA).

3. Characterization of the Adsorbents

3.1. X-Ray Diffraction (XRD). To evaluate the crystallinity of the clay minerals, X-ray diffractograms of these clays were registered (Figure 1). It should be noted that the crystallinity of clay minerals is relatively low compared to other inorganic compounds since these phyllosilicates are raw materials that have not undergone any purification.

The diffractogram of the Bent sample shows a strong and intense reflection with a maximum located at a 2θ value of 6.80° , which is ascribed to the d_{001} reflection. From this diffraction, it is possible to obtain the basal spacing of the Bent sample through the Bragg equation, obtaining a value of 13.0 \AA , so the cation located in the interlayer spacing must be partially hydrated. In the same way, other broad reflections are observed and ascribed to the bentonite. Of these, one of the most interesting diffraction peaks is the d_{060} reflection located at 2θ of 62.05° since it is possible to discern between a trioctahedral and dioctahedral smectite. The presence of the d_{060} reflection at 1.49 nm confirms that the phyllosilicate is dioctahedral, so this adsorbent must be an Al-rich smectite. On the other hand, other narrower reflections are observed, which are ascribed to some impurities (calcite, plagioclase, and cristobalite) [21].

In the case of the Sep sample, its typical diffraction peaks are observed, where the main diffraction peak is located at 2θ of 7.27° (12.1 \AA) and is assigned to the d_{110} reflection [29]. In addition, a small quartz impurity located at 2θ of 26.55° is observed. The diffractogram of the Ata sample shows a main peak located at 2θ of 8.37° (10.5 \AA), which is ascribed to the typical d_{110} reflection of this clay mineral [30]. Moreover, this sample also displays impurities of quartz.

Finally, the PCH synthesized from bentonite was also studied by XRD. The diffractogram of the PCH reveals that the insertion of Si pillars causes a loss of the nonbasal reflections while the basal reflections (d_{020} , d_{110} , d_{130} , d_{200} , and d_{060}) are maintained although these signals can suffer a random displacement as a consequence of the partial delamination of the clay mineral [31]. On the other hand, the absence of impurities after the formation of the PCH is striking, as was observed in previous studies [19]. The analysis of the low angle of the PCH (Figure 2) reveals the presence of a broad band located about 2θ of 2.60° (33 \AA), which confirms

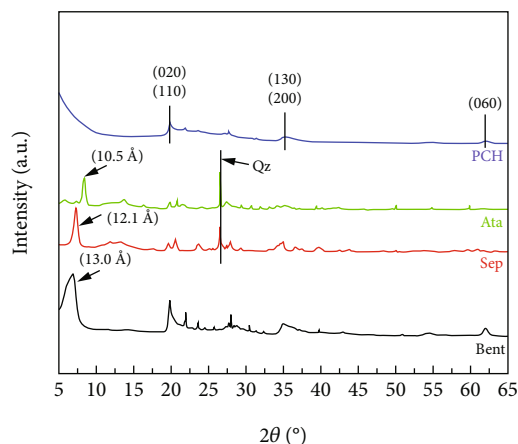


FIGURE 1: X-ray diffractograms of bentonite (Bent), sepiolite (Sep), attapulgite (Ata), and porous clay heterostructure (PCH).

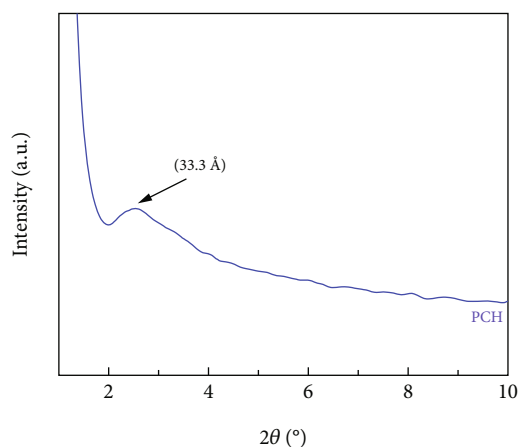


FIGURE 2: Low-angle X-ray diffractogram of the PCH.

the formation of an expanded structure because of the insertion of silica pillars between adjacent sheets to form the PCH structure [21].

3.2. Transmission Electron Microscopy (TEM). The morphology of the raw clays and the PCH was analyzed by TEM (Figure 3). In the case of the Bent sample (Figure 3(A)), the typical lamellar structure of bentonite can be observed. When the pillars are included to form the PCH (Figure 3(B)), the lamellar structure is maintained although a higher disorder of the sheets is observed, confirming that the insertion of pillars causes a partial delamination of the structure [31]. Both the Sep and Ata samples show a fibrous structure (Figures 3(C) and 3(D)). From the TEM, it is not possible to differentiate between both fibrous structures since the difference between them lies in the periodic inversion of the tetrahedral sheet leading to microchannels with the dimensions of $0.37 \text{ nm} \times 1.06 \text{ nm}$ for Sep and $0.37 \text{ nm} \times 0.64 \text{ nm}$ in the case of Ata [32].

3.3. Textural Properties. The textural properties of the raw clay minerals and the PCH were determined from N_2 adsorption-desorption isotherms at -196°C (Figure 4).

According to the IUPAC classification, the isotherms of both raw clay minerals and PCH can be adjusted to type II, which are typical of materials with high macroporosity due to the voids between adjacent particles [33]. Regarding the hysteresis loops, the isotherm can be fitted to type H3, which is typical of nonrigid aggregates of plate-like particles as clay minerals [33]. In the case of the raw clays, it can be observed how the N_2 -adsorbed at low relative pressure is relatively low, which suggests that these materials display low microporosity. These data are striking for the fibrous phyllosilicates (Sep and Ata) since these clays display nanocavities, which are very efficient for retaining small molecules such as CO_2 [32]. In these fibrous phyllosilicates, N_2 -adsorption values increase remarkably at a high relative pressure. This supposes that both materials display high macroporosity probably due to voids between adjacent fibers. The analysis of the adsorption isotherm of the Bent sample shows how the N_2 adsorption is lower than that observed for both fibrous phyllosilicates, so it is expected that the Bent sample shows poorer textural properties than the other raw clays. However, the substitution of the cation located in the interlayer spacing by a bulkier organic cation and the formation of pillared structures such as PCH lead to structures with higher porosity. Thus, the PCH sample shows a clear increase in N_2 adsorption at low relative pressures, so an increase in microporosity is expected, probably due to the partial delamination of the clay mineral in the pillaring step and its subsequent calcination leading to a microporous structure due to the formation of a house-of-cards structure [31]. This delamination also gives rise to the formation of macroporosity, as suggested by the increase in N_2 adsorption at a high relative pressure.

The estimation of the mesoporosity was carried out by the BET equation (Table 1) [22]. BET surface area (S_{BET}) values reveal how the raw clay with the highest surface area and higher microporosity is Sep due to the presence of zeolitic channels. In the case of the other fibrous clays (Ata), it can be observed how this sample displays lower meso- and microporosities. In this sense, it has been reported in the literature that Sep can host a higher proportion of small molecules, such as CO_2 , in its zeolitic channels than Ata [32]. The synthesis of the PCH improves textural properties compared to its respective starting bentonite. Thus, it can be observed how PCH displays a BET surface area of $640 \text{ m}^2 \text{ g}^{-1}$ and a pore volume of $0.828 \text{ cm}^3 \text{ g}^{-1}$. In addition, the t -plot data also reveals that PCH displays high microporosity than the raw bentonite [21]. These data confirm that the incorporation of PCH promotes the formation of micro-, meso-, and macropores.

The estimation of the pore size distribution was carried out by the DFT method (Figure 5) [23]. This figure shows how all raw clays display a wide pore distribution due to the variable porosity ascribed to the voids between adjacent particles. However, in the case of the PCH, the presence of a narrow distribution with two maxima can be observed. The first maximum located at 1.9 nm is probably attributed to the microporosity generated in the synthesis of the PCH, and a second maximum, located about 3.0 nm , is

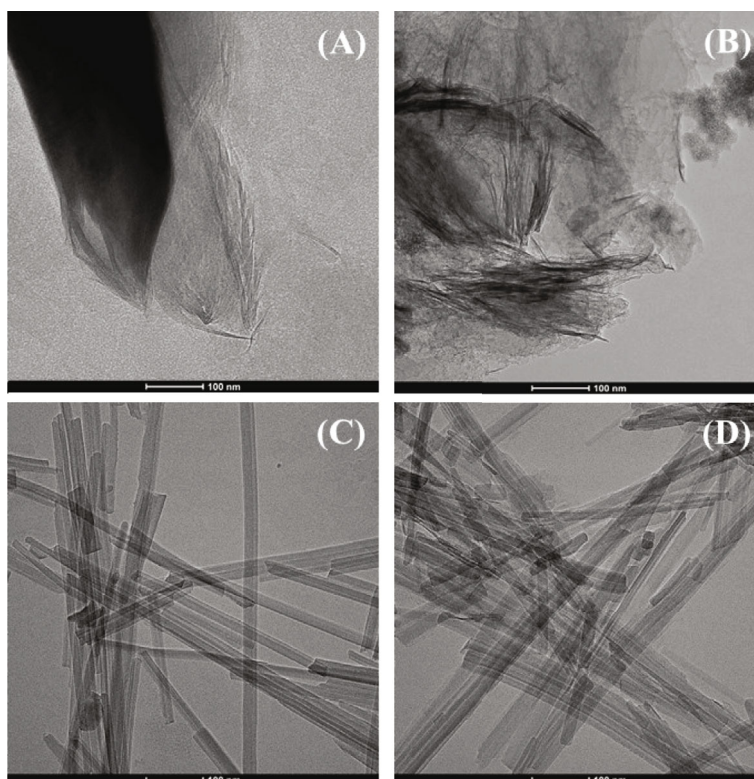


FIGURE 3: TEM micrographs of Bent (A), PCH (B), Sep (C), and Ata (D).

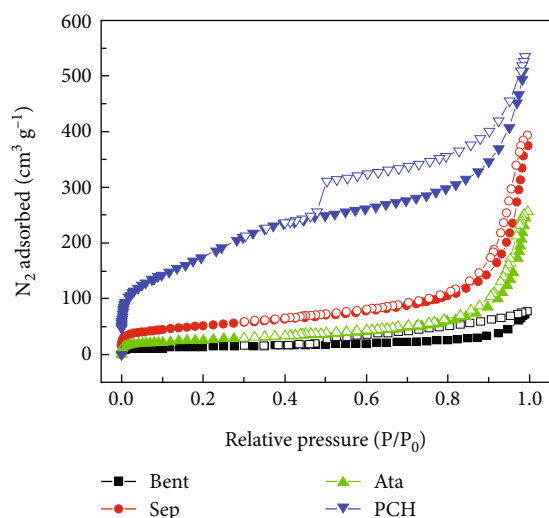


FIGURE 4: N₂ adsorption-desorption isotherms at -196°C of Bent, Sep, Ata, and PCH.

ascribed to the porosity generated in the pillared process and the delamination of the clay. This value seems to agree with that data obtained for low-angle XRD (Figure 2).

3.4. Attenuated Total Reflectance (ATR). Both the raw clay and the PCH obtained from the Bent sample were also characterized by ATR (Figure 6(a)). The study of the -OH stretching region, compiled in Figure 6(a), shows how the Bent sample displays a broad band located about 3630 cm⁻¹, which is assigned to the Al(OH)Al stretching vibration

TABLE 1: Textural properties of Bent, Sep, Ata, and PCH samples estimated from N₂ adsorption-desorption isotherms at -196°C.

Sample	S_{BET} (m ² g ⁻¹)	t -plot _{mic} (m ² g ⁻¹)	t -plot _{ext} (m ² g ⁻¹)	V_p (cm ³ g ⁻¹)
Bent	48	14	21	0.119
Sep	182	48	134	0.608
Ata	93	13	80	0.397
PCH	640	376	264	0.828

mode, which is typical of Al-rich smectites [34, 35]. In addition, the presence of a small contribution close to 3700 cm⁻¹ also draws attention, which suggests the existence of pyrophyllite-like local structural fragments [34]. In the case of the Sep sample, two bands located at 3690 and 3625 cm⁻¹ are observed [32, 36], which are assigned to -OH stretching vibration modes coordinated with Mg²⁺ species, while the band located at 3670 cm⁻¹ is assigned to the H₂O stretching vibration mode coordinated with Mg²⁺ species [36].

Regarding the Ata sample, Frost et al. pointed out that this clay mineral exhibits two bands located at 3616 and 3552 cm⁻¹, which are assigned to the -OH stretching vibration modes of Mg²⁺ and Al³⁺ or Fe³⁺ species, respectively [36]. In both fibrous clays (Sep and Ata), two other bands located about 3400 and 3250 cm⁻¹ are attributed to the physisorbed H₂O in the nanocavities [32]. The study of the PCH sample shows how the band located about 3630 cm⁻¹ disappears due to the thermal treatment in the calcination step, causing a partial dehydroxylation of the Al-rich smectite [21]. The absence of a band about 3740 cm⁻¹ is also

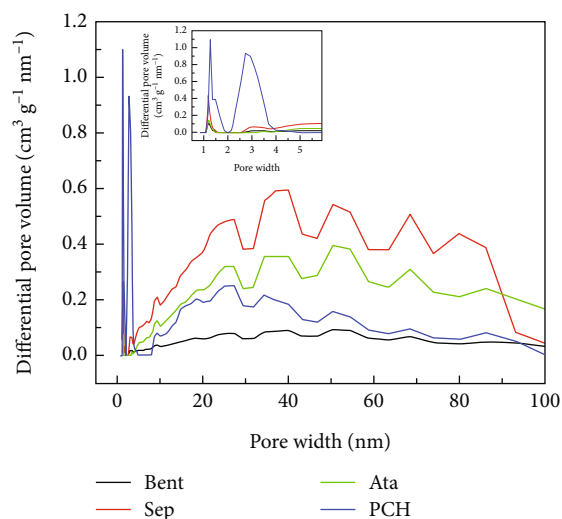


FIGURE 5: Pore size distribution of Bent, Sep, Ata, and PCH.

noticeable, discarding the presence of silanol groups in the SiO_2 pillars because the pyrolytic treatment promotes the dehydroxylation of the silanol groups into siloxane.

The analysis of the region between 2000 and 500 cm^{-1} (Figure 6(b)) for the Bent sample shows a broad band with a maximum located at 1030 cm^{-1} , which is assigned to the Si-O stretching mode [37]. The band located at 918 cm^{-1} is attributed to the Al_2OH bending mode, while the shoulder located about 884 cm^{-1} is attributed to the AlMgOH bending mode due to the partial substitution of Al by Mg species. The small contributions located about 793 and 693 cm^{-1} are assigned to Fe_2OH and Fe-O out-of-plane vibration modes, indicating that Fe^{3+} must be partially replacing Al^{3+} species. Finally, the bands located at 525 and 465 cm^{-1} are assigned to Si-O-Al and Si-O-Si bending vibrations, respectively [37].

In the case of the Sep sample, the set of bands between 1230 and 850 cm^{-1} is assigned to the Si-O stretching mode. In the same way, the bands located about 785 cm^{-1} and 470 cm^{-1} are assigned to the Si-O-Si symmetric stretching vibration and Si-O-Si bending mode, respectively. The band located at 660 cm^{-1} is assigned to the Mg_3OH bending vibration mode, while the band about 425 cm^{-1} is attributed to the Si-O-Mg bending vibration mode. For the Ata sample, a band located at 515 cm^{-1} can also be observed, to which the Si-O-Al bending vibration mode is assigned [32, 38].

For the PCH sample, the incorporation of the SiO_2 pillar causes a shift of the band ascribed to the Si-O stretching mode to higher wavenumber values. In the same way, the broad bands close to 975 cm^{-1} (Si-O in-plane stretching vibration mode) and 805 and 470 cm^{-1} (bending vibration modes) also confirm the presence of SiO_2 in the form of pillars [39], as suggested from XRD (Figure 2) and textural property data (Figures 4 and 5).

Finally, a broad band at 1630 cm^{-1} is observed for all samples. This band is assigned to the H-O-H bending mode band, which is typical of the physisorbed H_2O .

4. Adsorption Studies

From the dilution of the concentrated crude extract, a solution of ACNs with a concentration equal to $40\text{ mg}\cdot\text{L}^{-1}$ was prepared using ultrapure water as the diluent. This solution presented a concentration of sugars equal to $2283.7\text{ mg}\cdot\text{L}^{-1}$. The prepared volume was sufficient to carry out all experiments.

4.1. Selection of Adsorbents. It is well-known that phyllosilicates are materials with high cation exchange capacity and high adsorption capacity for organic molecules. Thus, these adsorbents can be potential hosts to ACNs. As shown in Figure 7, the PCH sample displays a high adsorption capacity for ACNs ($q = 16.89\text{ mg g}^{-1}$), adsorbing approximately 42% of the pigments in the solution. This result did not differ statistically ($P > 0.05$) from that presented by the Sep sample (16.64 mg g^{-1}), which has reached an adsorption capacity of 41%. The lowest values were observed for the Ata sample, which only adsorbs 27.4% of the pigments.

The results obtained for the PCH and Sep samples are directly related to their structural properties (Table 1). For the PCH sample, the formation of a pillared and delaminated adsorbent with high micro- and mesoporosity results in a greater ACN adsorption [40, 41]. In the case of the Sep sample, the fibrous morphology with a crystalline structure, with high specific surface area and high porosity (Table 1), results in a high capacity for adsorption of dyes, organic compounds, and other substances [42, 43]. On the other hand, the smaller surface area obtained by the Bent and Ata samples seems to be related to the lowest observed ACN adsorption values. Thus, considering the amount of ACNs adsorbed, the PCH and Sep samples were selected to perform the other adsorption tests.

4.2. Influence of the Mass in the Adsorbent Test. The data reported in Figure 8 show how the amount of adsorbed ACNs increased proportionally with the increasing mass of the adsorbent; however, this increase was nonlinear for the PCH sample. The ratio between the mass of adsorbed ACNs and the mass of adsorbent showed that, in terms of process economy, 25 mg of clay was sufficient for the effective adsorption of ACNs, which was equal to 0.096 and 0.180 mg for Sep and PCH samples, respectively. From these results, it was possible to evaluate the most suitable mass of clay for the adsorption of ACNs from the cabbage extract, which is, in general, an important result to determine the maximum adsorption capacity and the economy of the process.

4.3. Equilibrium Conditions for the Adsorbents. It can be observed that adsorption of ACNs in Sep and PCH occurred quickly after the first few minutes of the process (Supplementary Information, Figure S1). For the Sep sample, equilibrium conditions were reached after the third minute, obtaining a relationship between the initial concentration (C_0) and the final concentration (C_f) of $C_0/C_f = 0.77$. Using a longer adsorption time causes a slight increase in adsorption, showing an initial to final

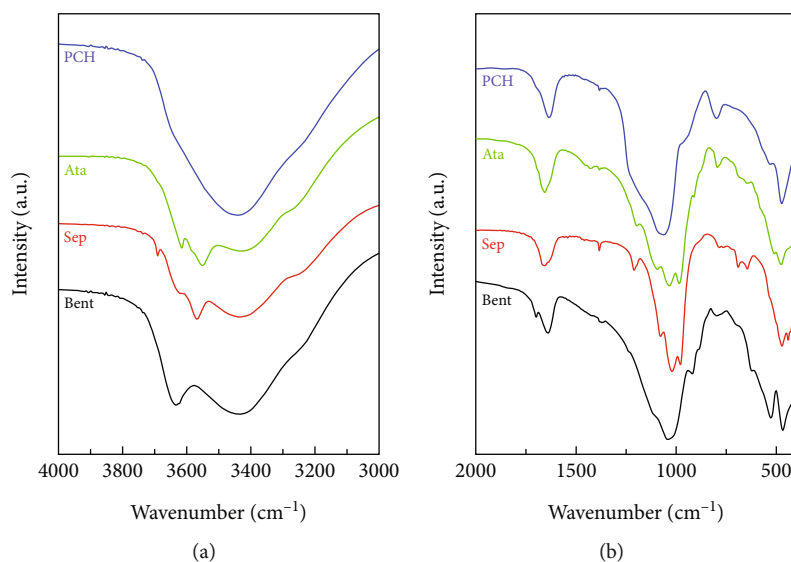


FIGURE 6: ATR of Bent, Sep, Ata, and PCH in the region 4000-3000 cm^{-1} (a) and 2000-400 cm^{-1} (b).

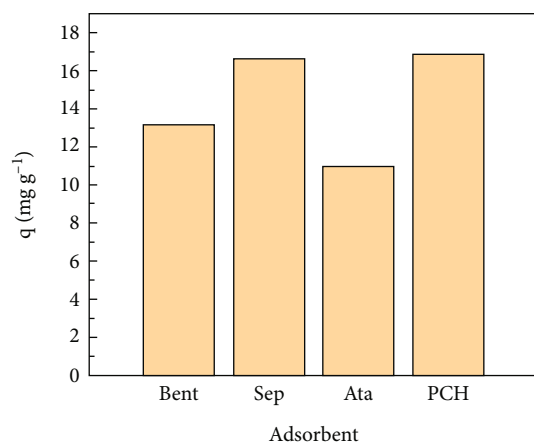


FIGURE 7: Amount of ACNs adsorbed (q) in different natural and modified clays after 3 hours of contact during the adsorbent selection test.

concentration ratio of 0.66 after 300 minutes. For PCH, it is noteworthy that the adsorption is more progressive. Thus, the adsorption curve presents an intense decrease, going from 0.46 after 3 min to 0.298 at 120 min, when the equilibrium was reached. The PCH showed great potential for adsorption, around 70.2% of ACNs after 120 minutes of processing. However, Sep only adsorbs 35% of the ACNs after 300 min. The obtained results from the PCH samples are above those obtained by Lopez et al. [8], who achieved an adsorption of about 35% of the ACNs, using a similar initial concentration of purple cabbage (*Brassica oleracea* var. Capitata) and using commercial clays as adsorbent.

The ACN adsorption mechanism process on clays can be explained by the behavior of the system in the solution. Previous studies have reported that the exposition of the clay minerals to a polar solvent, such as H_2O , promotes negative electrical charges on the surface of the sheets through different mechanisms (e.g., dissociation of groups or dissolution

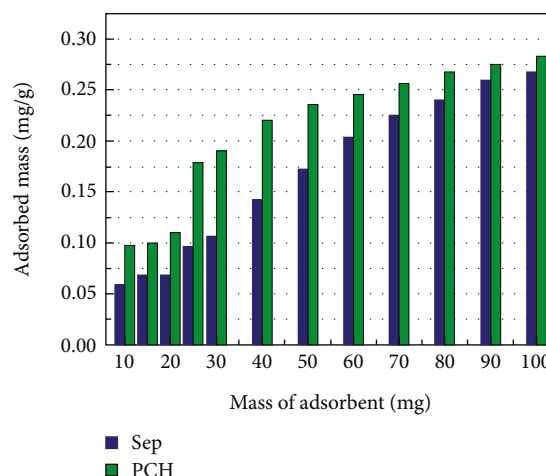


FIGURE 8: Mass of ACNs adsorbed in different amounts of Sep and PCH.

of surface ions and uniform adsorption) [44]. As ACNs take the form of flavylum cations in moderately acidic conditions, some authors have reported that fast adsorption should take place with the negative charges of the sheets [45]. On the other hand, the higher adsorption capacity of PCH compared to the Sep sample must also be attributed to its textural properties. The presence of high microporosity allows hosting a higher proportion of ACNs in narrow pores due to electrostatic interactions.

4.4. Influence of the pH in the Adsorption Process. The pH is a critical factor in the adsorption process between the ACNs and the clays, so this parameter was monitored during the assays. Abrupt pH changes have not been detected in the samples containing Sep and PCH. However, a different behavior was observed for each one. For the Sep sample, the pH value increases slightly from the beginning ($\text{pH} = 3.91$) to the end ($\text{pH} = 4.70$) when equilibrium is reached (300 min). This increase suggests that Sep has the

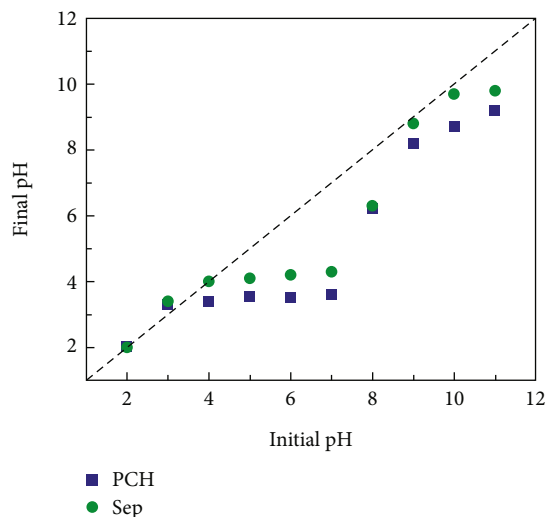


FIGURE 9: pH of zero charge (pH_{PZC}) of the Sep and PCH samples.

potential to retain H^+ species, so it can be plausible that adsorption on sepiolite could take place between the flavylum cations and the fibers, which are negatively charged on their surface [45].

In the case of the PCH sample, the variation presents a slight decrease, reaching a pH of 3.23 after the equilibrium time (300 min). This suggests that the adsorption process must follow a different mechanism than that in the case of the Sep sample. In this sense, it has previously been reported that the decay in pH could be ascribed to the compensation of unbalanced charges in the ACN and clay structures [8, 46]. As the pH after the adsorption process has not increased, the presence of another type of interaction, alternative to the ionic, is also possible. In this sense, the interaction between the PCH and ACNs through other electrostatic interactions in narrow micropores is also possible.

4.5. Study of the Point of Zero Charge (pH_{PZC}). To determine the pH of the zero charge (pH_{PZC}) point of the clays, the pH_{PZC} value was calculated from the difference between the initial and final pH. Figure 9 reveals that the PCH presented its pH_{PZC} at 3.4, while the Sep sample reaches pH_{PZC} at 4.0. This value indicates the pH value at which there is a balance between the positive and negative charges on the surface of these adsorbents. Thus, for pH values lower than pH_{PZC} , PCH and Sep present a positive surface charge, leading to a higher affinity for anionic groups. When the pH is higher than pH_{PZC} , the surface of these clays has a negative surface charge and therefore a higher affinity for cationic groups. Considering that the pH of the plant extract used in the adsorption is around 3.9, the ACNs are in the form of flavylum cation. At this pH value, ACNs are positively charged, while the Sep sample must be negatively charged although this value is very close to the pI, so the Sep sample should be barely charged at that pH value. Under these conditions, the presence of ionic interactions between the ACNs positively charged and the surface of the clay layers together with other interactions as hydrogen bonds should be expected [47]. In the case of the PCH sample, the adsorbent

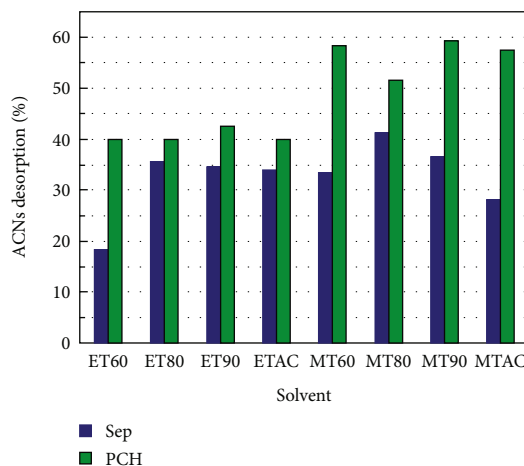


FIGURE 10: Percentage of ACNs desorbed in relation to the concentration adsorbed by the PCH and Sep, modifying the proportion of eluents (ethanol and methanol) and their concentrations (ET60: ethanol 60%; ET80: ethanol 80%; ET90: ethanol 90%; ETAC: acidified ethanol; MT60: methanol 60%; MT80: methanol 80%; MT90: methanol 90%; MTAC: acidified methanol).

is positively charged while the ACNs are also positively charged. This should cause repulsive interactions so the adsorption must follow another type of interaction. In this sense, the high surface area and high micro- and mesoporosity of the PCH sample should capture ACN molecules in its porous structure [48].

4.6. Desorption Studies. For the desorption process, the best conditions obtained in the adsorption stage were reproduced. Thus, the desorption data have been obtained based on the percentages of adsorbed ACNs (i.e., 70% or $28.0 \text{ mg}\cdot\text{L}^{-1}$ in PCH and 35% or $14 \text{ mg}\cdot\text{L}^{-1}$ in Sep).

In the first stage, it was observed that the ACN desorption was proportional to time for both clays. Even with similarity, the desorption of ACNs in the PCH adsorbent shows better results in the range of time evaluated. The greatest desorption occurred at 120 minutes, where 40% of the ACNs was desorbed ($11 \text{ mg}\cdot\text{L}^{-1}$). Under the same conditions, 36% of the ACNs ($5.04 \text{ mg}\cdot\text{L}^{-1}$) of the Sep sample was desorbed.

Figure 10 shows the desorption profiles of the ACNs using different amounts of ethanol and methanol. For the Sep sample, the best results have been attained using ethanol ($4.97 \text{ mg}\cdot\text{L}^{-1}$) and methanol ($5.77 \text{ mg}\cdot\text{L}^{-1}$), at a concentration of 80% (v/v). The Sep sample eluted with ethanol 60% presented the lowest desorption percentage (18%), while the others presented values above 28%. For the PCH, the best results were obtained using methanol as the eluent, in concentrations of 60 and 90%, which reached about 60% of desorption (16.40 and $16.60 \text{ mg}\cdot\text{L}^{-1}$, respectively). In the case of ethanol, the PCH samples showed a similar desorption pattern, varying between 39.90% ($11.17 \text{ mg}\cdot\text{L}^{-1}$) and 42.60% ($11.92 \text{ mg}\cdot\text{L}^{-1}$). Considering that all the samples eluted with methanol presented a desorption capacity higher than those eluted with ethanol, PCH (60% methanol) was chosen as the eluent, as it presented a capacity of desorption equal to

58.60% (16.40 mg L⁻¹). In addition, it was also observed that the acidification of the eluent did not influence the desorption in both cases.

On the other hand, it is also noticeable that desorption is less efficient in the case of Sep. These data suggest that the interaction between ACNs and Sep, which must be partially ionic, is stronger than that observed between ACNs and PCH, despite that ACN molecules must be captured in the porous structure.

4.7. Quantification of Sugars. Compared to the concentration of the initial solution, the solutions that remained after the adsorption process present a high concentration of sugars (89.56% for the Sep sample and 81.05% for the PCH sample), showing that the clays did not adsorb a large amount of this set of molecules. This result suggests that the affinity of the ACNs for the adsorbent is higher and faster than that of sugars. In this sense, sugars are also bulkier than ACNs, which is also difficult for their adsorption. In both clays, the solutions obtained after desorption showed a sugar concentration of only 2% of the initial content, indicating that the clays showed good selectivity related to ACNs. In this sense, previous authors reported a concentration of sugar less than 0.1% compared to their initial extract using macroporous resins for the purification of the ACNs extracted from purple cabbage (*Brassica oleracea* var. *Capitata*) and jambolan fruit (*Syzygium cumini* L.) [49, 50].

4.8. Anthocyanin Identification. The UPLC-QToF analyses, carried out in the positive ionization mode, allowed identification of the compounds present in the purple cabbage extract before and after the adsorption process on the clays, as well as in the desorption. Peaks identified in the PCH (Supplementary Information, Figure S2A) and Sep (Supplementary Information, Figure S2B) chromatograms were labeled according to the order of elution. In Table 2, it is possible to find six identified compounds, their protonated ions and their ionic fragments, as well as the error in parts per million (ppm) and their possible molecular formula. The extracted ACNs are listed below.

Peak 1 (rt = 2.244 min) represents cyanidin-3-diglucoside-5-glucoside, and its structure is the basis for the composition of the other ACNs, as was previously reported by other authors [51]. Beside the position and quantity of sugars, the bonds with phenolic acids, such as synaptic (peaks 2 and 5), ferulic (peaks 3, 4, and 5), and coumaric (peak 2) acids, characterized the structural difference of ACNs. The identification of these acids in the structure was facilitated due to the presence of their characteristic fragments [52, 53].

All the ACNs identified in this study are acylated and derived from cyanidin-3-diglucoside-5-glucoside (m/z 773), which is in agreement with other studies carried out for other cabbage species [54–56]. This is confirmed by tandem mass spectrometry (MS/MS) of the molecular ions having the fragments m/z 449 or m/z 611, which represent the residues of cyanidin-5-glucoside and cyanidin-3-diglucoside, respectively [56], as well as the fragment m/z 287, which corresponds to cyanidin [56].

Peak 2 (rt = 3.889 min), with m/z 919, shows the fragments of ions m/z 757, due to the loss of a hexose, and m/z 449 and m/z 287, which are characteristic of cyanidin [57]. The presence of these fragments indicates the possibility of coumaric acid in the structure of the pigment; thus, the compound was identified as cyanidin-3-(p-coumaroyl)-diglucoside-5-glucoside [2].

Peak 3 (rt = 4.006 min) indicates the presence of two compounds, which possibly coeluted. The first compound showed m/z 979 with the presence of fragments, m/z 449 and m/z 287, and also m/z 817, referring to the loss of a glucose molecule [58, 59]. The ACNs were identified as cyanidin-3-(sinapoyl)-diglucoside-5-glucoside [54]. The second compound (mass spectrum m/z 949) presents a fragment with m/z 287, common to cyanidins, being identified as cyanidin-3-(feruloyl)-diglucoside-5-glucoside. For peak 4 (rt = 4.292 min), the ion fragmentation in m/z 1125 produced ions m/z 963 related to the loss of a glucosyl residue, m/z 449 for the loss of diglucosyl, and m/z 287 of the cyanidins. These fragments indicated the presence of two ferulic acids in the ACN structure, corresponding to the compound cyanidin-3-(feruloyl)(feruloyl)-diglucoside-5-glucoside [2, 60].

Peak 5 (rt = 4.354 min) presents a mass spectrum m/z 1155. The presence of fragments m/z 993, m/z 449, and m/z 287 is observed. This compound was identified as cyanidin-3-(sinapoyl)(feruloyl)-diglucoside-5-glucoside, due to the presence of synaptic and ferulic acids [59, 60].

When comparing the chromatograms of the initial, post-adsorption, and postdesorption phases (Supplementary Information, Figure S2A), striking differences are observed between the intensities of the peaks in the samples. Analyzing in terms of concentration and intensity from the overlapping of the peaks, the compound cyanidin-3-diglucoside-5-glucoside (rt = 2.254 min) is more evident in the postadsorption step. However, this compound is less evident in the postdesorption phase, indicating that a low concentration of these ACNs was adsorbed and, consequently, recovered from the PCH.

The behavior of peak 2 (rt = 3.889 min) indicates that a considerable amount of cyanidin-3-(p-coumaroyl)-diglucoside-5-glucoside was adsorbed and recovered from the PCH. This result is evidenced by the intense decrease in the intensity of this peak from the first to the second stage, intensifying again in the last stage.

The compounds coeluted in peak 3 (rt = 4.006 min), cyanidin-3-(sinapoyl)-diglucoside-5-glucoside and cyanidin-3-(feruloyl)-diglucoside-5-glucoside, did not have large amounts adsorbed, once the peak in the second stage showed a slight decrease. However, a reduced amount of these adsorbed ACNs was recovered since the peak is also evidenced in the postdesorption stage.

Most of the ACNs adsorbed and recovered, possibly, were cyanidin-3-(feruloyl)(feruloyl)-diglucoside-5-glucoside (peak 4, rt = 4.292 min) and cyanidin-3-(sinapoyl)(feruloyl)-diglucoside-5-glucoside (peak 5, rt = 4.354 min). Both compounds were more evident in the recovery profiles (postdesorption stage), while in the postadsorption stage, they were less apparent. Unlike the other compounds identified in the chromatogram, these ACNs present two organic

TABLE 2: Constituents identified or tentatively identified in the ACN extract of red cabbage.

Peak	rt (min)	[M ⁺] (m/z)		Ion fragments (m/z)	Error (ppm)	Molecular formula	Compound	Ref.
		Observed	Calculated					
1	2.254	773.2140	773.2150	611/449/287	1.3	C ₃₃ H ₄₁ O ₂₁	Cyanidin-3-diglucoside-5-glucoside	[54]
2	3.889	919.2508	919.2525	757/449/287	1.5	C ₄₂ H ₄₇ O ₂₃	Cyanidin-3-(p-coumaroyl)-diglucoside-5-glucoside	[54]
3	4.006	979.2719	979.2745	817/449/287	2.1	C ₄₄ H ₅₁ O ₂₅	Cyanidin-3-(sinapoyl)-diglucoside-5-glucoside	[54]
3	4.006	949.2628	949.2630	287	1.5	C ₄₃ H ₄₉ O ₂₄	Cyanidin-3-(feruloyl)-diglucoside-5-glucoside	[51]
4	4.292	1125.3087	1125.3149	963/449/287	5.5	C ₅₃ H ₅₇ O ₂₇	Cyanidin-3-(feruloyl)(feruloyl)-diglucoside-5-glucoside	[53]
5	4.354	1155.3193	1155.3282	993/287/449	7.9	C ₅₄ H ₅₉ O ₂₈	Cyanidin-3-(sinapoyl)(feruloyl)-diglucoside-5-glucoside	[51]

acids in their structure (ferulic or synaptic). Thus, these ACNs have a higher number of hydroxyl and carboxylic groups in their structure, which may promote a better interaction between the ACNs and the sheets and the SiO₂ pillars of the adsorbent surface through electrostatic interactions [61].

For the Sep sample (Supplementary Information, Figure S2B), the adsorption and desorption profiles indicated that this clay does not present a good affinity for the compounds referring to peaks 1, 2, and 3, since their intensity hardly shows considerable changes between the beginning and postadsorption stages. However, there is a lower intensity of these peaks in the postdesorption stage, indicating that these ACNs were recovered from the Sep sample. Regarding peaks 4 and 5, their intensities decreased from the first to the second stage and are quite apparent in the last stage, showing that a large part of these compounds is desorbed on the Sep sample, and therefore, these ACNs are recovered.

5. Conclusions

Several clay minerals have been selected for the recovery and elution of ACNs from purple cabbage to a subsequent valorization. The results obtained in this research showed that the best conditions to adsorb ACNs were obtained using PCH as the adsorbent, and the higher adsorption properties of this clay were related to its higher surface area and pore volume. The 60% methanol solution was found as the best eluent, allowing the recovery a large amount of ACNs adsorbed on PCH. Both the PCH and the sepiolite exhibited a high selectivity for ACNs and a low affinity for the sugars present in the ACN crude extract, facilitating the recovery of these pigments free of possible contaminants. The analysis of the samples by UPLC-QToF and FTIR indicated that the profile of anthocyanins present in purple cabbage is composed of different cyanidin species and that those with more than one organic acid in their structure had a higher affinity for clay, as well as a higher recovery rate. This research was aimed at evaluating the best operating conditions in a simple batch process to obtain a partially purified anthocyanin extract and obtain important results, which will serve as the basis for future research based on the application of anthocyanins and their purified form.

Data Availability

The authors confirm that all data generated or analyzed during this study are available from the corresponding author. These materials can be requested directly from the corresponding author if needed.

Conflicts of Interest

The authors declare that they have no conflicts of interest.

Acknowledgments

This publication is part of the R&D project PID2021-126235OB-C32 funded by MCIN/AEI/10.13039/501100011033/ and FEDER funds and R&D project TED2021-130756B-C31 funded by MCIN/AEI/10.13039/

501100011033/ and European Union Next Generation funds. The authors also thank Conselho Nacional de Desenvolvimento Científico e Tecnológico (CNPq, Ministério da Ciência, Tecnologia, Inovações e Comunicações, Brazil) for its financing support.

Supplementary Materials

The supplementary information contains the kinetic studies of Sep and PCH (Figure S1) and the chromatograms of anthocyanins in the purple cabbage extract and their respective chromatograms postadsorption and postdesorption in PCH (Figure S2A) and in sepiolite (Figure S2B). (*Supplementary Materials*)

References

- [1] S. Oancea and Z. M. Linn, "Anthocyanins: powerful natural antioxidant pigments with significant biomedical and technological applications," *Oxidation Communications*, vol. 41, no. 1, pp. 92–106, 2018.
- [2] J. Zhang, Z. Wang, and X. Liu, "Characterization of acylated anthocyanins in red cabbage via comprehensive two-dimensional high performance liquid chromatography and HPLC-MS," *Journal of Food Processing and Preservation*, vol. 41, no. 2, Article ID e13129, 2017.
- [3] L. M. Soldatkina and V. O. Novotna, "Adsorption removal of anthocyanins from red cabbage extracts by bentonite: statistical analysis of main and interaction effects," *Chemistry, Physics and Technology of Surface*, vol. 8, no. 4, pp. 439–447, 2017.
- [4] P. Ongkowijoyo, D. A. Luna-Vital, and E. González de Mejía, "Extraction techniques and analysis of anthocyanins from food sources by mass spectrometry: an update," *Food Chemistry*, vol. 250, pp. 113–126, 2018.
- [5] T. J. Lopez, S. R. Yaginuma, M. G. N. Quadri, and M. B. Quadri, "Evaluation of red cabbage anthocyanins after partial purification on clay," *Brazilian Archives of Biology and Technology*, vol. 54, no. 6, pp. 1349–1356, 2011.
- [6] A. Kraemer-Schafhalter, H. Fuchs, and W. Pfannhauser, "Solid-phase extraction (SPE)—a comparison of 16 materials for the purification of anthocyanins from *Aronia melanocarpa* var Nero," *Journal of the Science of Food and Agriculture*, vol. 78, no. 3, pp. 435–440, 1998.
- [7] X. Liu, G. Xiao, W. Chen, Y. Xu, and J. Wu, "Quantification and Purification of Mulberry Anthocyanins with Macroporous Resins," *BioMed Research International*, vol. 2004, Article ID 713759, 6 pages, 2004.
- [8] T. J. Lopez, M. G. N. Quadri, and M. B. Quadri, "Recovery of anthocyanins from red cabbage using sandy porous medium enriched with clay," *Applied Clay Science*, vol. 37, no. 1-2, pp. 97–106, 2007.
- [9] M. F. Ávila, L. C. Lima, and T. J. Lopes, "Adsorption of red cabbage dye through Pequi coat charcoal (*Cariocar brasiliense*)," *Revista Electronica en Gestado, Educação e Tecnologia Ambiental*, vol. 19, no. 2, pp. 1561–1573, 2015.
- [10] D. Cheikh, H. Majdoub, and M. Darder, "An overview of clay-polymer nanocomposites containing bioactive compounds for food packaging applications," *Applied Clay Science*, vol. 216, article 106335, 2022.

- [11] J. A. Cecilia, C. García-Sancho, E. Vilarrasa-García, J. Jiménez-Jiménez, and E. Rodríguez-Castellón, "Synthesis, characterization uses and applications of porous clays heterostructures: a review," *Chemical Record*, vol. 18, no. 7-8, pp. 1085–1104, 2018.
- [12] M. Suárez and E. García-Romero, "Advances in the crystal chemistry of sepiolite and palygorskite," *Developments in Clay Science*, vol. 3, pp. 33–65, 2011.
- [13] M. Suárez, J. García-Rivas, E. García-Romero, and N. Jara, "Mineralogical characterisation and surface properties of sepiolite from Polatli (Turkey)," *Applied Clay Science*, vol. 131, pp. 124–130, 2016.
- [14] Z. Xu, H. Jiang, Y. Yu et al., "Activation and β -FeOOH modification of sepiolite in one-step hydrothermal reaction and its simulated solar light catalytic reduction of Cr(VI)," *Applied Clay Science*, vol. 135, pp. 547–553, 2017.
- [15] A. Gil, S. A. Korili, and M. A. Vicente, "Recent advances in the control and characterization of the porous structure of pillared clay catalysts," *Catalysis Reviews*, vol. 50, no. 2, pp. 153–221, 2008.
- [16] A. Galarneau, A. Barodawalla, and T. J. Pinnavaia, "Porous clay heterostructures formed by gallery-templated synthesis," *Nature*, vol. 374, no. 6522, pp. 529–531, 1995.
- [17] J. E. Aguiar, J. A. Cecilia, P. A. S. Tavares et al., "Adsorption study of reactive dyes onto porous clay heterostructures," *Applied Clay Science*, vol. 135, pp. 35–44, 2017.
- [18] M. D. Soriano, J. A. Cecilia, A. Natoli, J. Jiménez-Jiménez, J. M. López-Nieto, and E. Rodríguez-Castellón, "Vanadium oxide supported on porous clay heterostructure for the partial oxidation of hydrogen sulphide to sulfur," *Catalysis Today*, vol. 254, no. 1, pp. 36–42, 2015.
- [19] E. Vilarrasa-García, J. A. Cecilia, D. C. S. Azevedo, C. L. Cavalcante Jr., and E. Rodríguez-Castellón, "Evaluation of porous clay heterostructures modified with amine species as adsorbent for the CO₂ capture," *Microporous Mesoporous Materials*, vol. 249, no. 1, pp. 25–33, 2017.
- [20] M. V. Villar, L. Pérez del Villar, P. L. Martín et al., "The study of Spanish clays for their use as sealing materials in nuclear waste repositories: 20 years of progress," *Journal of Iberian Geology*, vol. 32, no. 1, pp. 15–36, 2006.
- [21] J. A. Cecilia, C. García-Sancho, and F. Franco, "Montmorillonite based porous clay heterostructures: influence of Zr in the structure and acidic properties," *Microporous and Mesoporous Materials*, vol. 176, pp. 95–102, 2013.
- [22] S. Brunauer, P. H. Emmett, and E. Teller, "Adsorption of gases in multimolecular layers," *Journal of American Chemical Society*, vol. 60, no. 2, pp. 309–319, 1938.
- [23] J. Landers, G. Y. Gor, and A. V. Neimark, "Density functional theory methods for characterization of porous materials," *Colloids and Surfaces A: Physicochemical and Engineering Aspects*, vol. 437, pp. 3–32, 2013.
- [24] R. S. Mikhail, S. Brunauer, and E. E. Bodor, "Investigations of a complete pore structure analysis," *Journal of Colloid and Interface Science*, vol. 26, no. 1, pp. 45–53, 1968.
- [25] J. R. Do, H. K. Kim, H. K. Kim, J. H. Hong, and G. D. Lee, "Optimization of extraction conditions for cabbage," *Journal of the Korean Society of Food Science and Nutrition*, vol. 34, no. 10, pp. 1625–1632, 2005.
- [26] M. Schreider and J. R. Regalbuto, "A fundamental study of Pt tetraammine impregnation of silica. 1. The electrostatic nature of platinum adsorption," *Journal of Catalysis*, vol. 225, no. 1, pp. 190–202, 2004.
- [27] J. R. Regalbuto and J. Robles, *The Engineering of Pt/Carbon Catalyst Preparation*, University of Illinois, Chicago, IL, USA, 2004.
- [28] M. Dubois, K. A. Gilles, J. K. Hamilton, P. A. Rebers, and F. Smith, "Colorimetric method for determination of sugars and related substances," *Analytical Chemistry*, vol. 28, no. 3, pp. 350–356, 1956.
- [29] F. Franco, M. Pozo, J. A. Cecilia, M. Benítez-Guerrero, E. Pozo, and J. A. Martín-Rubí, "Microwave assisted acid treatment of sepiolite: the role of composition and "crystallinity"," *Applied Clay Science*, vol. 102, pp. 15–27, 2014.
- [30] L. Pardo-Canales, S. Essih, J. A. Cecilia et al., "Modification of the textural properties of palygorskite through microwave assisted acid treatment. Influence of the octahedral sheet composition," *Applied Clay Science*, vol. 196, article 105745, 2020.
- [31] M. L. Ocelli, "Surface properties and cracking activity of delaminated clay catalysts," *Catalysis Today*, vol. 2, no. 2-3, pp. 339–355, 1988.
- [32] J. A. Cecilia, E. Vilarrasa-García, C. L. Cavalcante Jr., D. C. S. Azevedo, F. Franco, and E. Rodríguez-Castellón, "Evaluation of two fibrous clay minerals (sepiolite and palygorskite) for CO₂ capture," *Journal of Environmental Chemical Engineering*, vol. 6, no. 4, pp. 4573–4587, 2018.
- [33] M. Thommes, K. Kaneko, A. V. Neimark et al., "Physisorption of gases, with special reference to the evaluation of surface area and pore size distribution (IUPAC technical report)," *Pure and Applied Chemistry*, vol. 87, no. 9-10, pp. 1051–1069, 2015.
- [34] B. B. Zviagina, D. K. McCarty, J. Srodón, and V. A. Drits, "Interpretation of infrared spectra of dioctahedral smectites in the region of OH-stretching vibrations," *Clays and Clay Minerals*, vol. 52, no. 4, pp. 399–410, 2004.
- [35] J. A. Cecilia, L. Pardo, M. Pozo, E. Bellido, and F. Franco, "Microwave-assisted acid activation of clays composed of 2:1 clay minerals: a comparative study," *Minerals*, vol. 8, no. 9, p. 376, 2018.
- [36] R. L. Frost, O. B. Locos, H. Ruan, and J. T. Klopogge, "Near-infrared and mid-infrared spectroscopic study of sepiolites and palygorskites," *Vibrational Spectroscopy*, vol. 27, no. 1, pp. 1–13, 2001.
- [37] J. Madejová, "FTIR techniques in clay mineral studies," *Vibrational Spectroscopy*, vol. 31, no. 1, pp. 1–10, 2003.
- [38] M. A. Vicente-Rodríguez, M. Suárez, M. A. Bañares-Muñoz, and J. D. López-Suárez, "Comparative FT-IR study of the removal of octahedral cations and structural modifications during acid treatment of several silicates," *Spectrochimica Acta A*, vol. 52, no. 13, pp. 1685–1694, 1996.
- [39] J. A. Cecilia, E. Vilarrasa-García, C. García-Sancho et al., "Functionalization of hollow silica microspheres by impregnation or grafted of amine groups for the CO₂ capture," *International Journal of Greenhouse Gas Control*, vol. 52, pp. 344–356, 2016.
- [40] M. Eloussaief, A. Sdiri, and M. Benzina, "Modelling the adsorption of mercury onto natural and aluminium pillared clays," *Environmental Science and Pollution Research*, vol. 20, no. 1, pp. 469–479, 2013.
- [41] L. R. Sartor and A. C. de Azevedo, "Pilarização de argilas e perspectivas de aplicação e de pesquisa agrônômica e ambiental," *Ciência Rural*, vol. 44, no. 9, pp. 1541–1548, 2014.
- [42] Y. Gao, H. Gan, G. Zhang, and Y. Guo, "Visible light assisted Fenton-like degradation of rhodamine B and 4-nitrophenol solutions with a stable poly-hydroxyl-iron/sepiolite catalyst," *Chemical Engineering Journal*, vol. 217, pp. 221–230, 2013.

- [43] N. Liu, Y. Y. Song, Y. Qin, X. Gong, and Y. L. Liu, "Chromatic characteristics and anthocyanin compositions of cabernet sauvignon wines: influence of indigenous *Saccharomyces cerevisiae* strains in Ningxia, China," *Food Science and Biotechnology*, vol. 24, no. 6, pp. 1973–1978, 2015.
- [44] M. Jafellici Jr. and L. C. Varanda, "The world of colloids," *Química Nova Na Escola*, vol. 9, pp. 9–13, 1999.
- [45] A. B. Das, V. V. Goud, and C. Das, "Adsorption/desorption, diffusion, and thermodynamic properties of anthocyanin from purple rice bran extract on various adsorbents," *Journal of Food Process Engineering*, vol. 41, no. 6, article e12834, 2018.
- [46] G. A. F. Hendry and J. D. Houghton, *Natural Food Colorants*, Springer, 1996.
- [47] L. C. B. Lima, F. Castro-Silva, E. C. Silva-Filho, M. G. Fonseca, and M. Jaber, "Saponite-anthocyanin pigments: slipping between the sheets," *Microporous and Mesoporous Materials*, vol. 300, article 110148, 2020.
- [48] C. Agougui, J. A. Cecilia, H. Saad et al., "Adsorption of Carvone and Limonene from Caraway essential oil onto Tunisian montmorillonite clay for pharmaceutical application," *Scientific Reports*, vol. 12, no. 1, article 19814, 2022.
- [49] J. Chandrasekhar, N. Aduja, and K. S. M. S. Raghavarao, "Purification of anthocyanins from jamun (*Syzygium cumini* L.) employing adsorption," *Separation and Purification Technology*, vol. 125, pp. 170–178, 2014.
- [50] J. Chandrasekhar, M. C. Madhusudhan, and K. S. M. S. Raghavarao, "Extraction of anthocyanins from red cabbage and purification using adsorption," *Food and Bioproducts Processing*, vol. 90, no. 4, pp. 615–623, 2012.
- [51] N. Ahmadiani, R. J. Robbins, T. M. Collins, and M. M. Giusti, "Anthocyanins contents, profiles, and color characteristics of red cabbage extracts from different cultivars and maturity stages," *Journal of Agricultural and Food Chemistry*, vol. 62, no. 30, pp. 7524–7531, 2014.
- [52] P. Arapitsas and C. Turner, "Pressurized solvent extraction and monolithic column-HPLC/DAD analysis of anthocyanins in red cabbage," *Talanta*, vol. 74, no. 5, pp. 1218–1223, 2008.
- [53] W. Wiczkowski, D. Szawara-Nowak, and J. Topolska, "Red cabbage anthocyanins: profile, isolation, identification, and antioxidant activity," *Food Research International*, vol. 51, no. 1, pp. 303–309, 2013.
- [54] P. Arapitsas, P. J. R. Sjöberg, and C. Turner, "Characterisation of anthocyanins in red cabbage using high resolution liquid chromatography coupled with photodiode array detection and electrospray ionization-linear ion trap mass spectrometry," *Food Chemistry*, vol. 109, no. 1, pp. 219–226, 2008.
- [55] G. J. McDougall, S. Fyffe, P. Dobson, and D. Stewart, "Anthocyanins from red cabbage-stability to simulated gastrointestinal digestion," *Phytochemistry*, vol. 68, no. 9, pp. 1285–1294, 2007.
- [56] J. Sun, Z. Xiao, L. Z. Lin et al., "Profiling polyphenols in five *Brassica* species microgreens by UHPLC-PDA-ESI/HRMSⁿ," *Journal of Agricultural and Food Chemistry*, vol. 61, no. 46, pp. 10960–10970, 2013.
- [57] C. Aza-González and N. Ochoa-Alejo, "Characterization of anthocyanins from fruits of two Mexican chili peppers (*Capsicum Annuum* L.)," *Journal of the Mexican Chemical Society*, vol. 56, no. 2, pp. 149–151, 2017.
- [58] T. Shimizu, T. Muroi, T. Ichi, M. Nakamura, and K. Yoshihira, "Analysis of red cabbage colors in commercial foods using high performance liquid chromatography with photodiode array detection-mass spectrophotometry," *Shokuhin Eiseigaku Zasshi*, vol. 38, no. 1, pp. 34–38, 1997.
- [59] X. Wu and R. L. Prior, "Identification and characterization of anthocyanins by high-performance liquid chromatography-electrospray ionization-tandem mass spectrometry in common foods in the United States: vegetables, nuts, and grains," *Journal of Agricultural and Food Chemistry*, vol. 53, no. 8, pp. 3101–3113, 2005.
- [60] C. S. Charron, B. A. Clevidence, S. J. Britz, and J. A. Novotny, "Effect of dose size on bioavailability of acylated and nonacylated anthocyanins from red cabbage (*Brassica oleracea* L. Var. capitata)," *Journal of Agricultural and Food Chemistry*, vol. 55, no. 13, pp. 5354–5362, 2007.
- [61] W. S. W. Ngah and M. A. K. M. Hanafiah, "Biosorption of copper ions from dilute aqueous solutions on base treated rubber (*Hevea brasiliensis*) leaves powder: kinetics, isotherm, and biosorption mechanisms," *Journal of Environmental Sciences*, vol. 20, no. 10, pp. 1168–1176, 2008.

Research Article

Adsorption Study and Removal of Basic Fuchsin Dye from Medical Laboratory Wastewater Using Local Natural Clay

Fuad Hama Sharif Radha,¹ Dler M. S. Shwan¹ ,¹ and Stephan Kaufhold² 

¹Department of Chemistry, College of Science, University of Sulaimani, Sulaymaniyah 46001, Iraq

²Federal Institute for Geosciences and Natural Resources (BGR), Stilleweg 2, 30655 Hannover, Germany

Correspondence should be addressed to Dler M. S. Shwan; dler.salh@univsul.edu.iq

Received 19 October 2022; Revised 12 December 2022; Accepted 4 January 2023; Published 31 March 2023

Academic Editor: Juan A. Cecilia

Copyright © 2023 Fuad Hama Sharif Radha et al. This is an open access article distributed under the Creative Commons Attribution License, which permits unrestricted use, distribution, and reproduction in any medium, provided the original work is properly cited.

Local natural clay from Sulaimani zone-Takiya (TKC), Kurdistan Region of Iraq, was characterized and used for the removal of basic fuchsin (BF) dye from laboratory bacterial wastewater. The characterization of the adsorbent was carried out with XRD, XRF, and FT-IR. The clay sample was dominated by vermiculite. Adsorption tests under different conditions of contact time, pH of the solution, temperature, initial dye concentration, and adsorbent amount were performed to analyze the effect of various experimental parameters. Equilibrium time was reached within 180 minutes, and maximum BF adsorption was achieved at pH 6.8 at a temperature ranging from 20 to 50°C. The experimental data fitted the pseudo-second-order kinetic model, with the activation energy of 22.68 kJ·mol⁻¹. Adsorption isotherms could be well-fitted by the Langmuir isotherm model. The thermodynamic parameters such as ΔG° , ΔH° , and ΔS° were determined, and the negative values of ΔG° indicated that adsorption was spontaneous at all temperatures. Furthermore, the values of ΔH° indicated an endothermic reaction. Wastewater contaminated by BF dye from the bacterial laboratory was collected (BF concentration: 160 mg·L⁻¹) and treated by TKC. The resulting concentration of BF after adsorption was 4.76 mg·L⁻¹. The maximum amount of dye adsorbed is about 149.2 mg/g or 0.44 mmol/g, which is close to the range of the cation exchange capacity (CEC) value of the vermiculite which indicated that cation exchange was the dominant adsorption mechanism.

1. Introduction

Basic fuchsin (BF) is a fluorescent dye-containing mixture of rosaniline, pararosaniline, new fuchsine, and magenta II. The molecular formula is C₁₉H₁₇N₃ • HCl, and the maximum absorption wavelength is λ -max. UV-spectrophotometry is at 546 nm. BF is used for the detection of acid-fast bacilli and is commonly used in gram staining and a mixture with phenol for acid-fast staining of mycobacterium (tuberculosis and leprosy) in the procedure described by Ziehl-Neelsen [1]. Also, BF is used as a coloring agent in the industry for textile and leather materials [2].

Wastewater contaminated by BF could be released into the environment from the sewage of the medical laboratories or the textile and leather industry. Because of their low biodegradability, some of these dyes have been reported to accumulate in surface water and sediments which may be

environmentally hazardous [3]. Repeated exposure to this dye may cause toxicity and carcinogenic and mutagenic effects. In addition, its effect on the nervous system like headache, dizziness, muscle contraction, and ingestion system may cause gastrointestinal irritation with nausea and vomiting [4].

Various biological, chemical, and physical methods such as biodegradation, Fenton-biological treatment scheme, chemical oxidation, ozonolysis, filtration, ionic exchange, photodegradation, membrane technologies, coagulation/flocculation, and adsorption were tested for removing wastewater dye [5]. Although these are very efficient techniques, most of them present several drawbacks like high cost, incomplete elimination of the contaminants, and generation of sludge or by-products. Biodegradation is a low-cost method, but the bacterial strain was usually feasible for special dyes only and toxicity also posed problems for bacteria.

Also, a few biosorbents have been employed recently for the removal of BF in aqueous solutions [4, 6].

There is not much research involving the use of clay minerals for the adsorption and removal of BF from wastewater. However, related materials were tested such as modified red mud [7], natural clinoptilolite modified with apolaccase [8], and alkali-activated diatomite [9]. For these materials, the maximum adsorption capacity was $333 \text{ mg}\cdot\text{g}^{-1}$ (pH = 5), $2 \text{ mg}\cdot\text{g}^{-1}$ (pH = 6), and $10 \text{ mg}\cdot\text{g}^{-1}$ (pH = 6), respectively.

Among adsorbents such as fly ash [10], silica gel [11], wood [12], biogas slurry [13], activated carbon, and clay materials, clay-based materials can be considered as the most abundant and cheap raw materials which showed high adsorption capacity for colored compounds in wastewater [14, 15].

Vermiculite clay minerals are naturally occurring trioctahedral 2:1 phyllosilicate. They possess permanent negative charges and only partly exchangeable and hydrated interlayer ions like Ca^{2+} , Mg^{2+} , and Na^+ . Vermiculite is a natural and modified material that was used for the adsorption and removal of many types of textile dyes from wastewater [16]. Vermiculite adsorbed $107 \text{ mg}\cdot\text{g}^{-1}$ of basic blue [17] and $2.2 \text{ mg}\cdot\text{g}^{-1}$ of pyronine Y [18]. Also, methylene blue and crystal violet onto natural vermiculite were investigated. Maximum dye loading was 0.083 and $0.103 \text{ mmol}\cdot\text{L}^{-1}$, respectively [19]. Vermiculite was also used as a composite (AgI-Bi₂MoO₆/vermiculite) for the adsorptive and photocatalytic degradation of dyes [20]. In the present work, it was tried to test the adsorption and removal of BF from wastewater using locally available vermiculite. The reason for using vermiculite and not smectite is that it has a larger (negative) charge (>0.6 per formula unit), arising mostly from the substitution of Al^{3+} for Si^{4+} in tetrahedral sites [21, 22].

The hydrophobic character is a feature of BF molecules when occurs at a higher pH value, but at low pH values, its hydrophilicity and solubility are enhanced because the amino group of BF reaches the ionized state [23].

The present study is aimed at characterizing the TKC local clay and investigating the possible use of this clay as an efficient available and cheap adsorbent for wastewater treatment, due to the wide usage of BF dye and its toxicity in the wastewater.

2. Materials and Methods

2.1. Materials. Basic fuchsin (BF) is a dark green powder that will turn red in solution. Its molecular formula is $\text{C}_{19}\text{H}_{17}\text{N}_3 \cdot \text{HCl}$, and its maximum wavelength is 546 nm. Natural clay (TKC) was used in the adsorption process for the removal of basic fuchsin dye from wastewater.

2.2. Characterizations of Adsorbent. The chemical composition of the powdered TKC was determined by XRF with a PANalytical Axios spectrometer (ALMELO, Netherlands). The clay samples were prepared by mixing with a flux material (lithium metaborate Spectroflux, Flux No. 100A, Alfa Aesar) and melting into glass beads. The beads were analyzed by wavelength dispersive XRF. To determine loss on ignition (LOI), 1000 mg of sample material was heated to 1030°C for 10 min. XRD pattern was recorded using a

PANalytical X'Pert PRO MPD θ - θ diffractometer (Cu-K α radiation generated at 40 kV and 30 mA), equipped with a variable divergence slit (20 mm irradiated length), primary and secondary soller, Scientific X'Celerator detector (active length 0.59°), and a sample changer (sample diameter 28 mm). The samples were investigated from 2° to $85^\circ 2\theta$ with a step size of $0.0167^\circ 2\theta$ and a measuring time of 10 s per step. For specimen preparation, the top-loading technique was used. For the detailed clay mineralogical investigation, a texture slide of the $<2 \mu\text{m}$ fraction was prepared. 15 mg per cm^2 clay was used to record an XRD scan. An aliquot of 1.5 mL of suspension was deposited on the circular (diameter = 2.4 cm) ceramic tile which was 3 mm thick. The suspension was filtered through the tile using a vacuum filter apparatus. Furthermore, the specimens were stored overnight in an ethylene glycol (EG) atmosphere at 60°C . The clay films were measured from 1° to $40^\circ 2\theta$ (step size $0.03^\circ 2\theta$, 5 s per step) after cooling to room temperature, representing EG conditions. For measuring midinfrared spectra, the KBr pellet technique (1 mg sample/200 mg KBr) was applied. Spectra were collected on a Thermo Nicolet Nexus FTIR spectrometer (MIR beam splitter: KBr, detector DTGS TEC). The resolution was adjusted to 2 cm^{-1} . Measurements were conducted before and after drying the pellets at 150°C in a vacuum oven for 24 h. The surface emergence and microregion adsorbent before and after adsorption were measured using a scanning electron microscope (SEM, S-400 N, Hitachi).

2.3. Adsorption Studies. Adsorption experiments were carried out in batch systems to achieve the optimum operating conditions for the removal of the selected dye 0.1 g of clay mixed with 50 mL BF dye solutions of the desired concentration in 100 mL polyethylene dark bottles in a thermostatic shaker bath (GFL 1083) at the desired temperatures (20 – 50°C). After 5–300 min, the dispersion was centrifuged at 4000 rpm for 5 minutes to remove the clay from the solution which was spectroscopically investigated concerning its dye concentration. A Cary 60 UV-Vis spectrophotometer adjusted to 546 nm was used. The adsorption capacity (q) of the dye for each step was calculated using the following equation:

$$q = \frac{(C_o - C_e)V}{m}, \quad (1)$$

where C_o and C_e represent the initial and equilibrium concentrations ($\text{mg}\cdot\text{L}^{-1}$), respectively, V is the volume of the solution (L), and m is the mass of the adsorbent (g).

The impact of the contact time was first evaluated by varying the contact time (0 to 300 min) at room temperature. The initial pH effect of the BF solution was investigated in the range from 2.0 to 11.0. Different BF concentrations (10 to $400 \text{ mg}\cdot\text{L}^{-1}$) were utilized to study the impact of the initial BF concentration. The weight of the clay was varied from 0.025 to 0.25 g.

2.4. Desorption of BF from the TKC. To conduct the desorption experiments, the adsorption procedure was carried out using 0.1 g TKC with 50 mL of $150 \text{ mg}\cdot\text{L}^{-1}$ BF shaking for 180 minutes at 30°C . The adsorbed BF onto TKC was

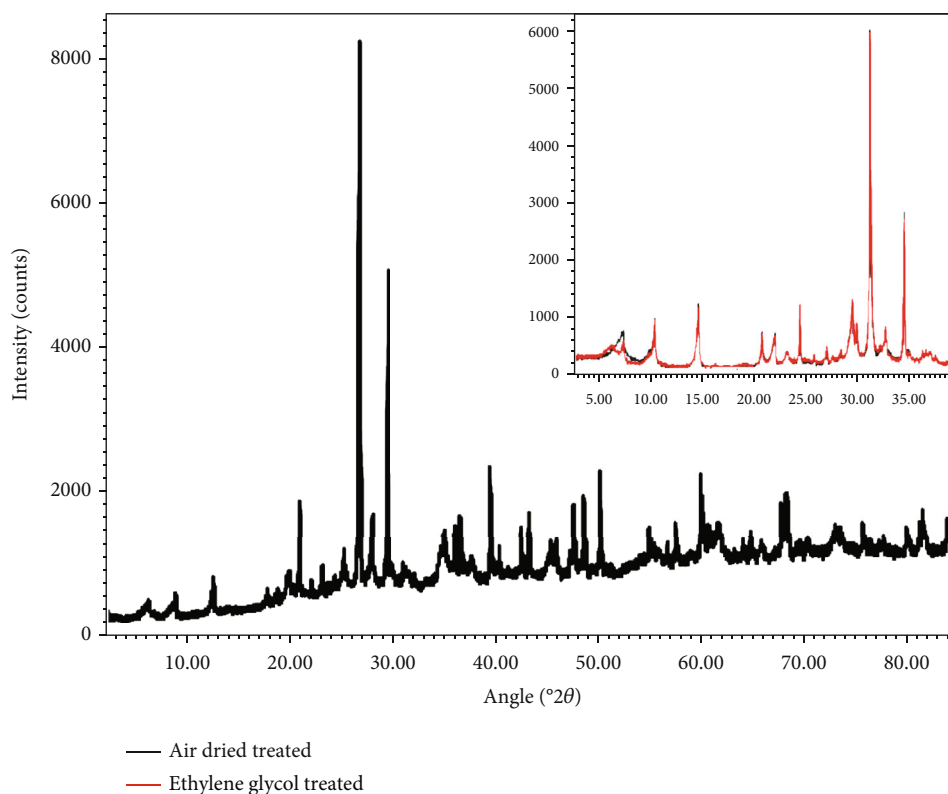


FIGURE 1: XRD pattern of random powder, air-dried, and EG saturated.

separated from the solutions and allowed to air-dry until it had reached a constant mass. By accounting for the dye concentrations in the solution that remained after the treatment, the amount of dye that had been absorbed was calculated. Following that, 2.00 g of dry, BF-adsorbed TKC was mixed for 1 hour with 50.0 mL of pH-adjusted water and then left to stand for 1 hour. The amount of desorption was estimated, and the concentration of BF that was leached out was calculated. For various beginning pH ranges (2-12), the desorption experiment was repeated.

3. Results and Discussion

3.1. Characterizations of Adsorbent. X-ray diffraction patterns of TKC are shown in Figure 1 for random powder, air-dried, and ethylene glycol (EG) saturated mounts. The peak observed at 14.2 Å was almost entirely shifted to 16.3 Å with EG saturated pointing towards the dominance of vermiculite [24] because smectite would shift to higher values. The powder pattern (randomly oriented mounts) proved the presence of calcite 3 Å, quartz 3.4 Å, muscovite 9 Å, and chlorite (mainly based on the (002) basal reflection at 7.1 Å and the remaining intensity at 14 Å after EG solvation).

The FTIR spectra of the TKC clay sample are dominated by a trioctahedral 2:1 clay mineral (vermiculite) as indicated by XRD (Figure 2). The spectra at 3622 and 3420 cm^{-1} and 3547 cm^{-1} were assigned to the OH-stretching of vermiculite and Fe-chlorite, respectively [25, 26]. OH-bending of water was determined by the bands at 1796 and 1637 cm^{-1} , while

the bands at 2412, 1900, 1431, and 712 cm^{-1} were due to calcite [27]. The identification of quartz was characterized by the doublet spectra of 792 cm^{-1} and 800 cm^{-1} . The main spectral feature at about 1027 cm^{-1} was related to the Si-O stretching of all silicates present in the sample. Infrared spectroscopy confirmed the qualitative mineral composition determined by XRD. However, X-ray fluorescence (XRF) was used for determining the chemical composition of TKC, which is following XRD and IR data. The XRF values were 46.4, 0.7, 13.3, 6.4, 0.1, 4.6, 10.6, 0.7, 2.1, 14.7, and 99.8 mass% for SiO_2 , TiO_2 , Al_2O_3 , Fe_2O_3 , MnO, MgO, CaO, Na_2O , K_2O , LOI, and the sum of elements.

The morphological properties of TKC before and after BF adsorption were analyzed by using scanning electron microscopy (SEM) which is a valuable tool for precise measurement and analysis of very small features and the morphology of the sample. A flake-like TKC adsorbent particle's surface is shown in Figure 3, both before (Figure 3(a)) and after (Figure 3(b)) BF adsorption. As can be observed in Figure 3(a), TKC has a rough surface with pores that can be identified as dark spots. These pores are then filled with BF dye molecules following adsorption as shown in Figure 3(b). It was possible to see the pores becoming blocked and the material shrinking as a result of BF adsorption.

3.2. Adsorption Studies

3.2.1. Study the Effect of Contact Time. The study of the contact time effect on the adsorption of BF dye was carried out at different temperatures (Figure 4). The quick absorption of

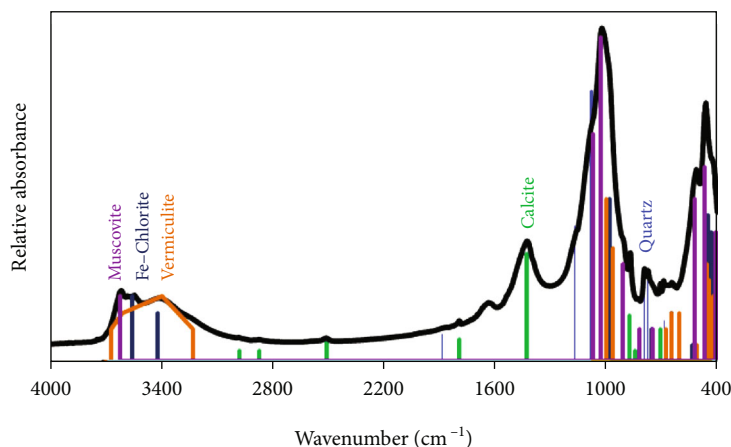


FIGURE 2: FTIR spectra of the TKC clay.

the dye can be noticed in the first 50th minutes of the adsorption process, which is due to the presence of a high number of empty adsorbent sites and the high affinity of solute concentration to the surface. The adsorption rate becomes slower after a period (>2 hours), and equilibrium was reached after 180 min of shaking the solution of the BF dye and TKC adsorbent at different temperatures. A 240-minute reaction time was used as a reference to ensure that equilibrium was reached and approached the constant values 72.75, 72.91, 73.5, and 73.8 mg·g⁻¹ at 20, 30, 40, and 50°C. The rate of dye adsorption onto the interior sites of the adsorbent particles in batch adsorption was controlled by the adsorption of dye molecules in the bulk solution onto the interior sites of the adsorbent particles [28].

The results (Figure 4) illustrate that increasing temperature may enhance the diffusion rate of the BF molecules from the bulk solution to the adsorbent surface, which means that there is a directly proportional relationship between temperature and the adsorption capacity of BF by TKC.

3.2.2. Study the Effect of the pH of the Solution. To investigate the effect of pH on TKC adsorption capability, the study was carried out with various initial pH levels ranging from 2 to 11. The removal efficiency (percent) and adsorption capacity (mg·g⁻¹) were shown versus the various initial pH. The adsorption is found to be strongly reliant on the pH of the solution, which influences the adsorbent's surface charge, degree of ionization, and dissociation of various functional groups on the active sites [29]. The dye's highest uptake occurs at pH values greater than 4, as seen in Figure 5, which is likely due to the hydrophobic nature of BF at higher pH values.

Therefore, all the subsequent studies were performed at the normal pH of the dye which was 6.8. The clay, however, is trioctahedral, and as a result, variable charge effects are supposed to be restricted to higher pH values.

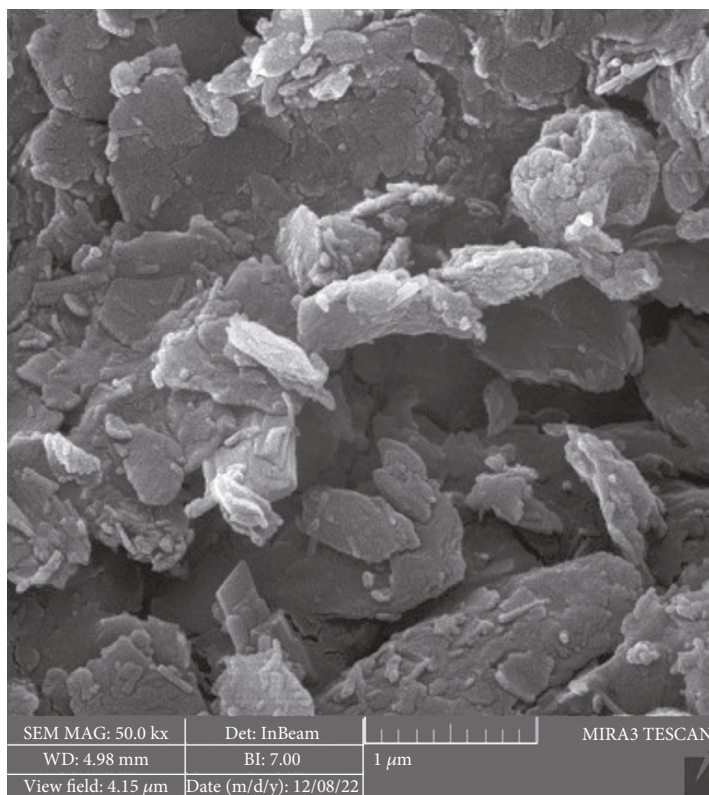
3.2.3. Point-Zero Charge (PZC) of Adsorbent. The PZC of the clay was measured using the pH drift method (Khan and Sarwar 2007). Series solutions of different pH were prepared by using HCl and NaOH; 0.1 g of the TKC was added to 50 mL of each adjusted solution in a sealed vial and equilibrated for 24 hours. The final pH was measured and plotted

against the original pH; the PZC was determined as the pH at which the curve crossed the pH_{initial} = pH_{final} line. This point is related to the charge on the particle's surface and is greatly influenced by the pH's effect on the charge on the TKC surface. As a result, it has an impact on a wide range of colloidal material properties, including their size and shape, stability, electrolyte interaction, suspension rheology, and ion exchange capacity.

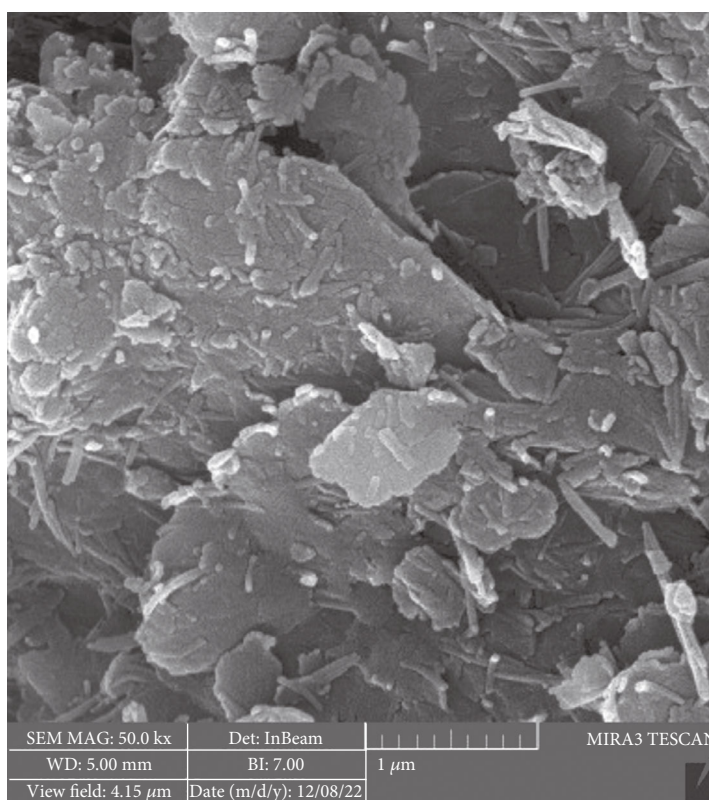
PZC of TKC (Figure 6) also explains the reason for the high adsorption of BF around neutral pH. The TKC adsorbent surface becomes negatively charged at pH values higher than 8.2, whereas it is within the opposite state for pH < 8.2. Figure 5 shows that the adsorption of BF onto TKC is highest for PZC above 8.2, which indicates that the negative form of TKC is responsible for adsorption in this range [30].

3.2.4. Study the Effect of Adsorbent Dosage. Applying varying concentrations (0.025 to 0.25 g) of adsorbent while maintaining all other experimental conditions constant (50 mL BF dye Co=150 mg·L⁻¹, pH=6.8, temperature=30°C, and 240 min equilibrium time shaking) was used to determine the adsorbent dosage influence. As shown in Figure 7, the adsorption capacity (mg·g⁻¹) and removal efficiency (percent) were plotted versus the clay weight dosage. When the overall surface area of the adsorbent (the number of adsorption sites) grows, as does the amount of the adsorbent, the percentage adsorption removal of BF dye increases, until it reaches an equilibrium to approach the constant value of 74.38 mg·g⁻¹ adsorption capacity, or 99.17% removal. As a result, TKC is considered a more effective adsorbent when compared to other adsorbents, such as the adsorption performance of BF on alkali-activated diatomite [9] and the use of HCl-treated malted sorghum mash [30].

3.2.5. Study the Effect of the Initial Concentration of BF Dye. The effect of the dye's initial concentration was investigated in the range of 10 to 400 mg·L⁻¹, while maintaining all other experimental conditions constant. Figure 8 shows that there is a direct proportion between the equilibrium adsorption capacity (q_e) and the initial dye concentration from 10 mg·L⁻¹ to 200 mg·L⁻¹. However, the percentage removal of dye ions decreased. The higher percentage uptake at lower



(a)



(b)

FIGURE 3: SEM of the TKC: (a) before BF adsorption; (b) after BF adsorption.

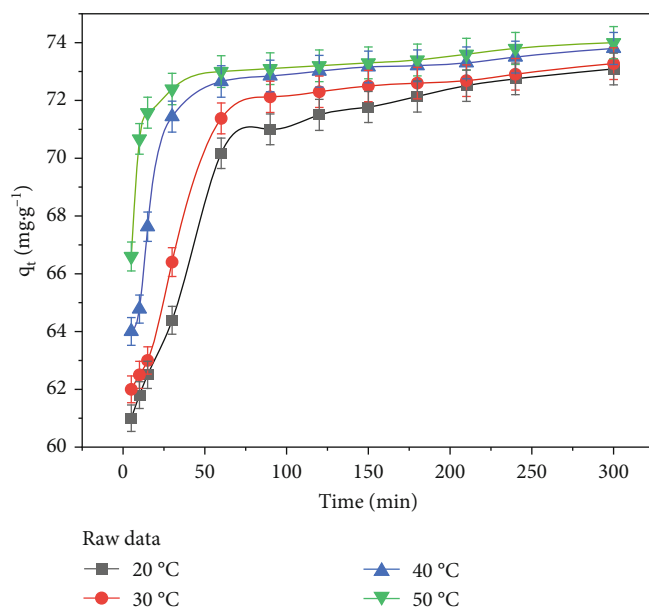


FIGURE 4: Effect of contact time on the adsorption of $150 \text{ mg}\cdot\text{L}^{-1}$ of BF dye on TKC at different temperatures.

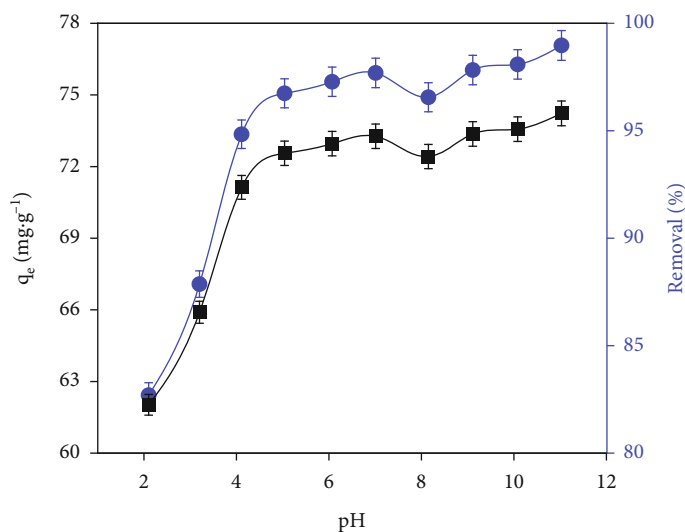


FIGURE 5: Effect of pH on the adsorption of $150 \text{ mg}\cdot\text{L}^{-1}$ of BF on TKC at 30°C .

dye concentrations was related to the available larger surface area of the adsorbent being for adsorption. While at a higher concentration of dye, the percentual uptake decreased, and this is because of the reducing number of available sites for adsorption due to saturation of adsorption sites. At a higher concentration of dye, the ratio of the initial number of moles of dye to the adsorption sites available was higher, resulting in a lower percentual removal [31].

3.2.6. Kinetic of Adsorption. The study of adsorption kinetics is significant to explore kinetic parameters (solute uptake rate determination and governs residence time or efficiency for sorption) because they can provide valuable information on the mechanism of the adsorption process. Preliminary investigations show that the adsorption kinetics at different temperatures increase with increasing contact time

(Figure 9). The kinetic studies further suggest that the adsorption equilibrium was attained within about 180 min.

The two most common kinetic models, pseudo-first-order and pseudo-second-order models, were applied for adsorption kinetics.

(1) *The Pseudo-First-Order Equation.* Lagergren proposed this equation, which is the most common kinetics equation, and it was most significant over the initial stage of the adsorption processes [32].

The pseudo-first-order equation describes the adsorption of solid/liquid systems given as

$$q_t = q_e \left(1 - e^{-k_1 t}\right). \quad (2)$$

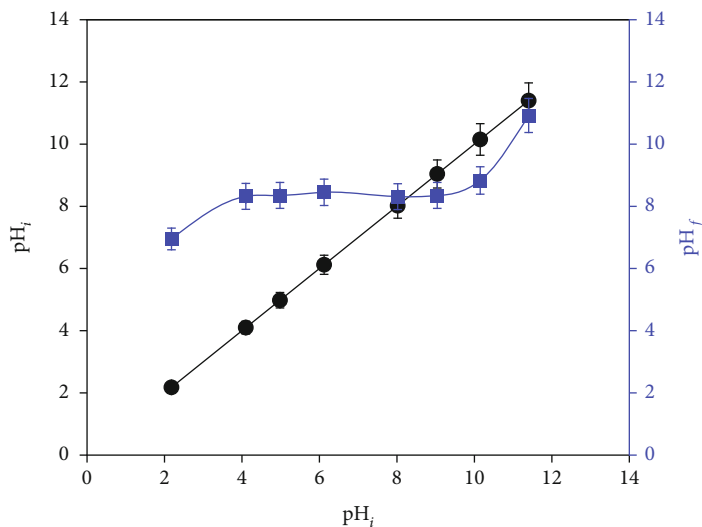


FIGURE 6: Determination of point of zero charges (pH_{PZC}) of the TKC by the pH drift method.

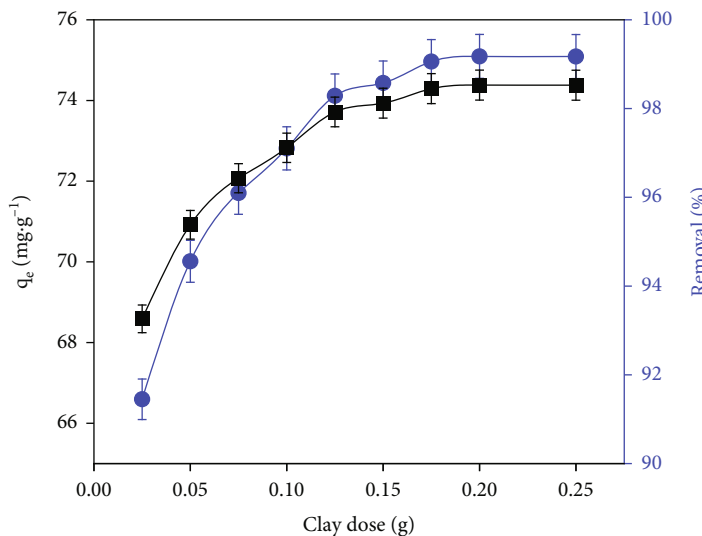


FIGURE 7: Effect of dosage on the adsorption of $150 \text{ mg}\cdot\text{L}^{-1}$ BF on TKC at 30°C .

The linearized form is

$$\log (q_e - q_t) = \log q_e - \frac{k_1}{2.303} t, \quad (3)$$

where k_1 is the pseudo-first-order rate constant (min^{-1}) of adsorption and q_e and q_t are the amounts of the BF dye (mg/g) adsorbed at equilibrium and at time t .

The Lagergren pseudo-first-order kinetic plots for the adsorption of BF dye on TKC were studied at different temperatures (Figure 9).

(2) *The Pseudo-Second-Order.* Both Ho and Mckay proposed this model depending on the hypothesis that the adsorption follows second-order chemisorption [33, 34].

The pseudo-second-order is assumed that the adsorption capacity is proportional to the number of binding sites occupied on the adsorbent. It is more likely to predict the behavior over the whole range of adsorption and agrees with the chemisorption mechanism being the rate-controlling step [35]. The linear form of the pseudo-second-order model is as follows:

$$\frac{t}{q_t} = \frac{1}{k_2 q_e^2} + \frac{t}{q_e}, \quad (4)$$

where q_t is the amount of adsorption at any time ($\text{mg}\cdot\text{g}^{-1}$), k_2 is the rate constant of the pseudo-second-order model ($\text{g}\cdot\text{mg}^{-1}\cdot\text{min}^{-1}$), q_e is the amount of adsorption equilibrium ($\text{mg}\cdot\text{g}^{-1}$), and t is the time (min).

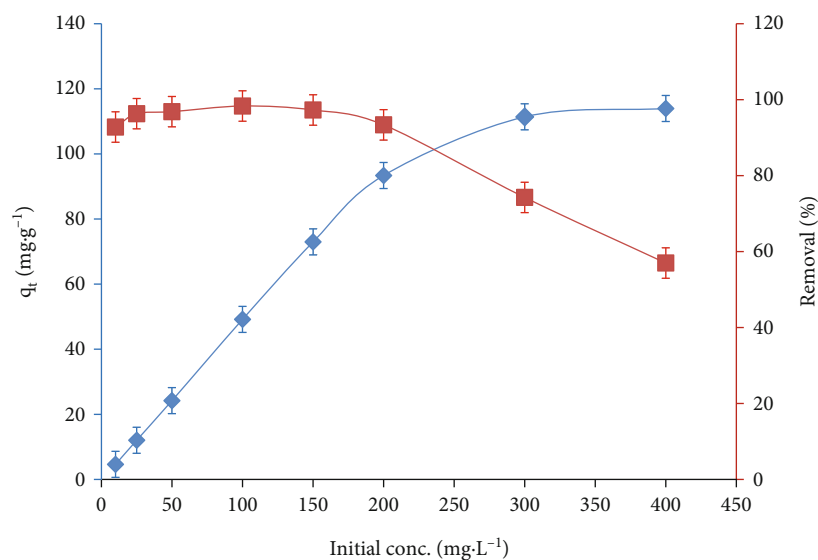


FIGURE 8: Effect of initial concentration on the adsorption of BF on 0.1 g of TKC at 30°C.

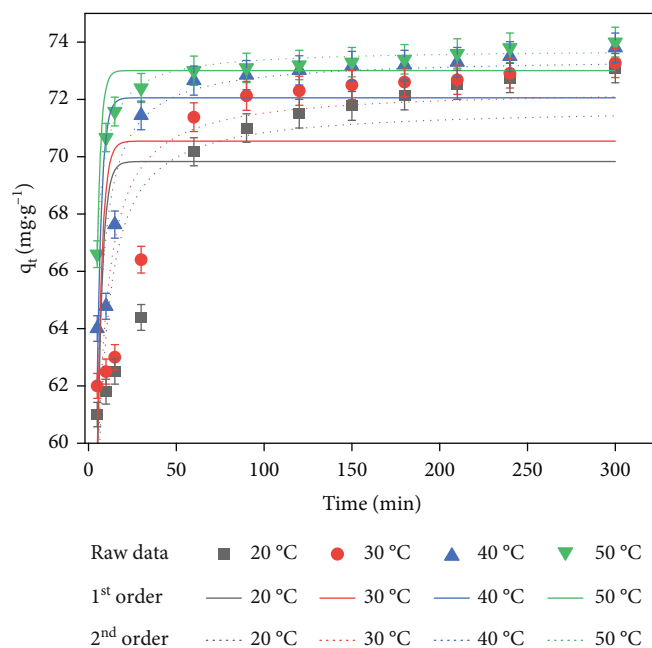


FIGURE 9: Nonlinear regression plots of pseudo-first-order and pseudo-second-order kinetics for the adsorption of BF dye on TKC at different temperatures.

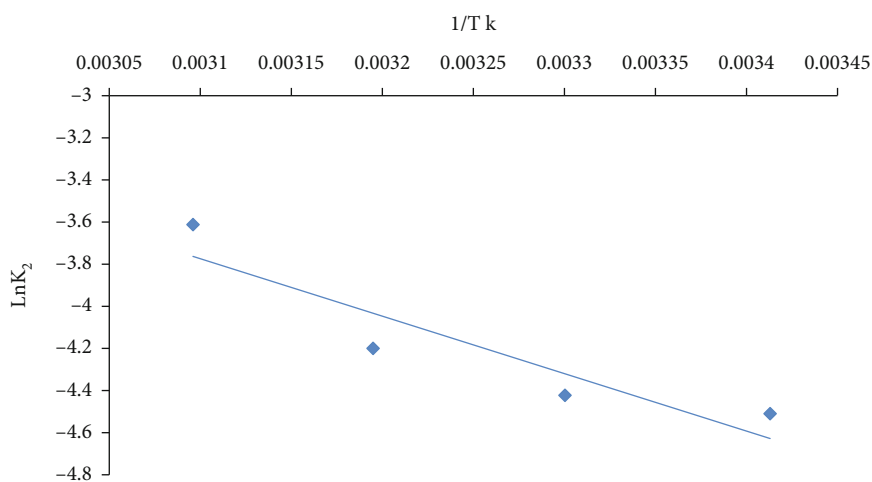
The pseudo-first and second-order kinetic plots for the adsorption of BF dye on TKC were calculated at different temperatures as illustrated in Figure 9. Table 1 shows that the corresponding kinetic parameters were evaluated from nonlinear regression fittings, and the kinetic parameters (rate constants k_1 and k_2 , correlation coefficients, and predicted ($q_{e, cal}$) values) are presented in Table 1.

The experimental higher value of R^2 and lower values of SSE are presented in Table 1 for the kinetic models. All of the information and the results from Figure 9 and Table 1, like the correlation coefficient values (R^2), the rate constants

of the kinetic models (K_1 and K_2), and the calculated maximum adsorption capacity (q_e) from the experiment compared with that obtained from the kinetics model, show that the data were better fitted with the pseudo-second-order model as compared to the pseudo-first-order model. The result showed that the pseudo-second-order correlation coefficient values for BF adsorption onto TKC of $R^2 = 0.767, 0.788, 0.905, \text{ and } 0.983$ at 293, 303, 313, and 323 K, respectively, while the pseudo-first-order correlation coefficient values of $R^2 = 0.348, 0.356, 0.509, \text{ and } 0.838$ at 293, 303, 313, and 323 K, respectively. The experimental values (q_e) of BF

TABLE 1: Kinetic model parameters for the adsorption of BF on TKC.

Kinetic models	Kinetic parameters	Temperature (K)			
		293	303	313	323
	q_{exp} (mg·g ⁻¹)	149.5	167.5	177.5	186.3
Pseudo 1 st order	q_{calc} (mg·g ⁻¹)	69.83106 ± 1.26091	70.54346 ± 1.19893	72.05584 ± 0.80815	73.00539 ± 0.26722
	k_1 (min ⁻¹)	0.47594 ± 0.02687	0.39655 ± 0.05393	0.37066 ± 0.07084	0.36236 ± 0.07184
	R^2	0.348	0.356	0.509	0.838
	SSE	163.3	148.1	67.9	7.6
Pseudo 2 nd order	q_{calc} (mg·g ⁻¹)	73.75046 ± 0.10077	73.45156 ± 0.4151	72.37468 ± 0.80579	71.72428 ± 0.88367
	k_2 (g·mg ⁻¹ ·min ⁻¹)	0.02653 ± 0.00122	0.01478 ± 0.00175	0.01159 ± 0.00223	0.01112 ± 0.00229
	R^2	0.767	0.788	0.905	0.983
	SSE	58.4	48.7	13.2	0.8

FIGURE 10: Plot of $\text{Ln}K_2$ versus $1/T$ (K) for BF on KTC adsorbent.

onto TKC were 149.5, 167.5, 177.5, and 186.3 g·g⁻¹ at 293, 303, 313, and 323 K, respectively, which were closer to that obtained from the pseudo-second-order kinetics model as compared to that of the pseudo-first-order. Also, the fast-kinetic adsorption of AFD in the first 30 minutes followed by gradual adsorption can be seen from the rate constant from both the pseudo-first-order and pseudo-second-order. The value of K_1 and K_2 was determined, indicating that the faster rate of adsorption is more directed towards that of the pseudo-second-order.

The study of the temperature effect on the rate at which BF is adsorbed from solution also allows for an evaluation of the activation energy (E_a) for the sorption reaction; the E_a can be calculated from the Arrhenius equation:

$$k_2 = A e^{-E_a/RT}. \quad (5)$$

The E_a value was calculated from the slope of the plot of $\ln k_2$ vs. $1/T$ (Figure 10), according to the Arrhenius equation (Equation (6)).

$$\ln k_2 = \ln A - \frac{E_a}{RT}, \quad (6)$$

where E_a (J·mol⁻¹), A (g·mol⁻¹·s⁻¹), K_2 (g·mol⁻¹·s⁻¹), R (8.314 J·K⁻¹·mol⁻¹), and T (k) are the activation energy of the adsorption and the Arrhenius pre-exponential factor, rate constant for pseudo-second-order, and the gas constant and temperature, respectively.

Low activation energies (<40 kJ·mol⁻¹) indicate the physical nature of the adsorption process, while the value of E_a (>80 kJ·mol⁻¹) indicates chemisorption. In the present case, E_a was found to be (22.68 kJ·mol⁻¹) which is consistent with physisorption [14].

3.2.7. Adsorption Isotherms. Investigating the mechanism of the adsorption process depends on the distribution of the adsorbate between solution and adsorbent at equilibrium conditions when the dynamic balancing between the concentrations of adsorbate in bulk solution with that of the interface is established. The data obtained from the sorption equilibrium can be used to acquire the adsorption capacity and certain constants whose values express the surface properties and affinity of a sorbent.

In the present study, Langmuir and Freundlich's isotherm parameters were used for the interpretation of the equilibrium adsorption data.

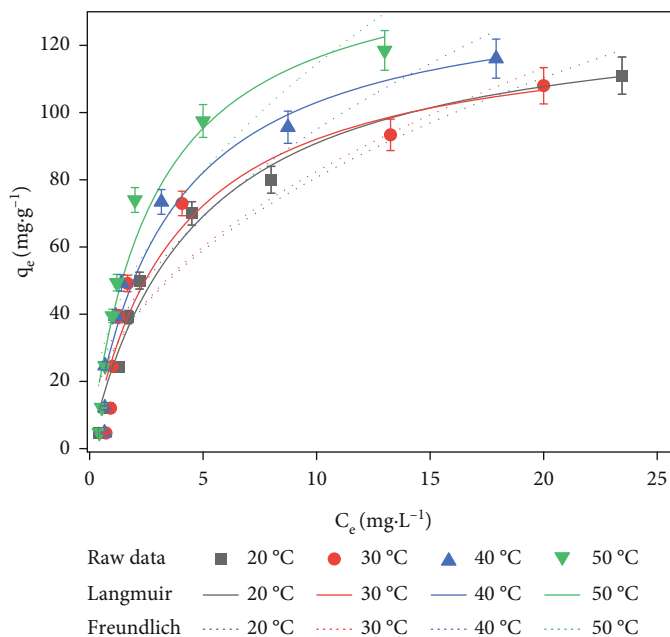


FIGURE 11: The Langmuir and Freundlich isotherm models for the adsorption of BF dye on TKC at different temperatures (0.1 g TC, initial pH = 6.0).

TABLE 2: Isotherm parameters for the adsorption of BF dye onto TKC adsorbent.

Isotherm models	Isotherm parameters	Temperature (K)			
		293	303	313	323
Langmuir	q_m (mg·g ⁻¹)	132.30323 ± 9.3445	126.75118 ± 13.68696	138.08058 ± 14.21631	149.16508 ± 15.80561
	K_L (L mg ⁻¹)	0.21934 ± 0.0377	0.26587 ± 0.07655	0.29393 ± 0.07778	0.35393 ± 0.08827
	R_L	0.029	0.024	0.022	0.018
	R^2	0.977	0.935	0.947	0.951
	SSE	213.2	653.6	593.4	572.5
Freundlich	K_F (mg·g ⁻¹) (L·mg ⁻¹)	28.52537 ± 4.66085	28.74579 ± 5.86427	32.76571 ± 5.95929	38.49453 ± 6.56976
	n_f	2.21404 ± 0.3234	2.18457 ± 0.39493	2.16319 ± 0.36822	2.11376 ± 0.38198
	R^2	0.910	0.876	0.884	0.863
	SSE	835.6	1244.6	1297.6	1600.2

The Langmuir isotherm model assumes that monolayer adsorption of the adsorbate over specific homogenous sites on the adsorbent surface occurs due to the certain number of fixed adsorption sites with equivalent properties [36].

The Langmuir isotherm can be expressed in the following equation (Equation (7)):

$$q_e = \frac{q_m K_L C_e}{1 + K_L C_e}, \quad (7)$$

@where q_e and q_m are the amounts of the adsorbate adsorbed per unit weight of clay (mg·g⁻¹) at equilibrium and monolayer saturation, respectively, K_L is the Langmuir equilibrium constant, and C_e is the concentration of the adsorbate in solution at equilibrium (mg·L⁻¹).

The values of K_L and q_m were calculated from the non-linear regression analysis at different temperatures

(Figure 11 and Table 2). The maximum dye adsorption capacity by TKC was found to be 149.2 mg·g⁻¹ or 0.44 mmol·g⁻¹ at 50 °C, which is close to the range of the CEC value of the vermiculite. Therefore, the main adsorption mechanism is cation exchange which is not surprising since the molecule is similar to other index cations that could be adsorbed by the clay. The values of K_L increased with increasing temperature, indicating that increasing temperature induced a higher maximum adsorption capacity.

The essential feature of the Langmuir isotherm can be expressed in terms of a dimensionless factor called separation factor also called equilibrium parameter (R_L) which is shown in the following equation [37]:

$$R_L = \frac{1}{1 + K_L C_0}, \quad (8)$$

TABLE 3: Thermodynamic parameters for the adsorption of BF dye onto TKC.

C_o (mg·L ⁻¹)	ΔH° (kJ·mol ⁻¹)	ΔS° (kJ·mol ⁻¹)	ΔG° (kJ·mol ⁻¹)			
			293 K	303 K	313 K	423 K
50	18.59	0.09	-7.22	-8.10	-8.98	-9.86
100	15.99	0.08	-7.62	-8.43	-9.23	-10.04

where K_L is the Langmuir constant and C_o is the initial concentration of the adsorbate. The shape of the isotherm indicates by the value of R_L to be either unfavorable ($R_L > 1$), linear ($R_L = 1$), favorable ($0 < R_L < 1$), or irreversible ($R_L = 0$).

The Freundlich equation is an empirical equation that describes multilayer adsorption of the adsorbate on a heterogeneous adsorbent surface. Equation (9) represents the linearized Freundlich isotherm [38].

$$q_e = K_f + C_e^{1/n}, \quad (9)$$

@where K_f and n are the Freundlich constants representing adsorption capacity and intensity, respectively.

The adsorption capacity K_f increased directly proportional to increasing temperature as represented in Table 2. The magnitude of n values (that gives a measure of the favorability of adsorption) between 1 and 10 ($1/n$ less than 1) represents favorable adsorption. In the present study, the value of n presented the same trend, indicating favorable adsorption [2].

Based on the high correlation coefficient R^2 , it has been deduced that the Langmuir model is better fitted to the experimental data.

3.2.8. Thermodynamic Studies. The effect of temperature on the adsorption is important to estimate the thermodynamic parameters such as ΔG° , ΔH° , and ΔS° , which are useful in determining whether the adsorption reaction is endothermic or exothermic and the spontaneity of the adsorption process.

The Gibbs free energy ΔG° (kJ·mol⁻¹) of adsorption was determined from the following equation:

$$\Delta G^\circ = -RT \ln Kc. \quad (10)$$

Standard entropy change ΔS° (kJ·mol⁻¹·K⁻¹) and standard enthalpy change ΔH° (kJ·mol⁻¹) of the adsorption process can be found from the van't Hoff equation as shown as follows:

$$\begin{aligned} \Delta G^\circ &= \Delta H^\circ - T\Delta S^\circ, \\ \ln Kc &= \frac{\Delta S^\circ}{R} - \frac{\Delta H^\circ}{RT}. \end{aligned} \quad (11)$$

Kc is calculated using the following equation:

$$Kc = \frac{C_s}{C_e}, \quad (12)$$

where K_c is the equilibrium constant and C_s and C_e are the equilibrium concentration (mg·L⁻¹) of the dye on the adsorbent and in the solution, respectively [39].

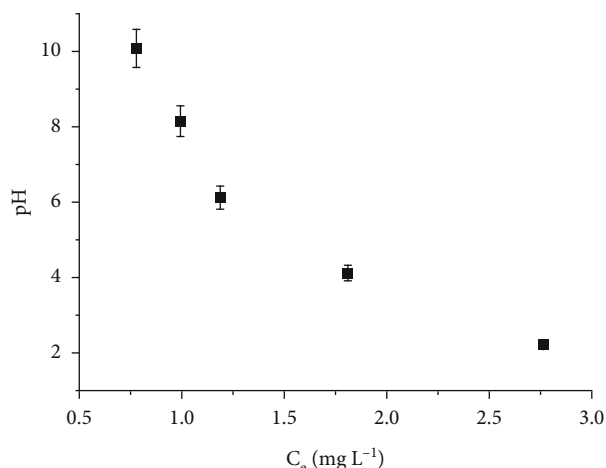


FIGURE 12: Concentrations obtained for desorbed BF dye at different initial solution pH values.

The values of the thermodynamic parameters are presented in Table 3. The negative value of ΔG° at all temperatures indicates the feasibility and spontaneity while the positive value of ΔH° substantiates the endothermic nature of the adsorption process. Also, if the ΔS° value is positive, the process would become more spontaneous on raising the temperature [40].

The positive value of ΔS° indicates that some structural changes may have taken place due to the affinity of interactions of dye molecules with active groups in the clay surface; therefore, the randomness at the solid/liquid interface during the adsorption is increased, despite the liberate inorganic cations from the clay causing an overall increase in entropy analogous [14, 41].

4. Desorption Study

A desorption study was conducted by altering the starting solution pH to examine the ability of adsorbed BF dye to leach into the solution under various conditions. Figure 12 displays the concentrations for samples desorbed with distilled water at various medium pH levels following pre-adsorption of a mixture of synthetic dye effluents with a concentration of 150 mg·L⁻¹. The results show that the desorption considerably increases at pH values below 2.5 and decreases with increasing medium pH. The reason why BF dye adsorbed on TKC is probably that BF is hydrophobic at higher pH values, as mentioned in the adsorption of dye with increasing pH of the medium, confirming the research's results. Therefore, highly acidic media are preferred for desorption. However, the reusability of the TKC is somewhat problematic, and further research is required.

More importantly, desorption experiments show that the BF dye adsorbed on the TKC adsorbent will not leach to the environment under normal conditions.

5. Applications on Real Samples

The BF-containing wastewater samples (laboratory wastewater) were taken from the Medical Laboratory Science (MLS) Department of Komar University, as a true sample for the remediation application of wastewater through the use of TKC natural clay. The real samples include detectable (BF) with a noticeable amount ($160 \text{ mg}\cdot\text{L}^{-1}$) of BF depending on whether the used amount of distilled water was for washing and liberating the excess of the BF that was used in excess for coloring the bacteria species. The pH of the wastewater (real) samples was measured and was found in the range of 7.2–7.7. Adsorption tests were carried out using the TKC described in the current work. The final concentration following adsorption of BF after adsorption onto TKC was $4.76 \text{ mg}\cdot\text{L}^{-1}$. These results showed that the adsorbent was capable to eliminate BF from wastewater (real samples) at a rate of greater than 97%.

6. Conclusion

The surface of natural local clay (TKC) is a more effective adsorbent for the removal of hydrophilic organic compounds such as basic fuchsin dye from aqueous solution; this is due to the electrically charged and hydrophilic characteristics of the surface. The parameters that affected the adsorption such as pH, contact time, temperature, adsorbent dose, and initial dye concentration were determined. The influence of the initial pH of the solution on the adsorption showed a significant effect, and the efficient pH was obtained at the normal pH of the BF dye (pH = 6.8). The maximum amount of dye adsorbed is about $149.2 \text{ mg}\cdot\text{g}^{-1}$ or $0.44 \text{ mmol}\cdot\text{g}^{-1}$, which is close to the CEC value of the vermiculite. Cation exchange, hence, is supposed to be the dominant adsorption mechanism which is also in agreement with the kinetic and thermodynamic results. The negative value of ΔG° indicated spontaneity at study temperatures, and the positive values of ΔS° show the affinity of the adsorbent to the adsorbate. The positive values of ΔH° and the adsorption of the dye are favorably influenced by the increase in temperature indicating the endothermic nature of the adsorption process. Also, the sorption kinetics followed the pseudo-second-order model. The calculated activation energy for the adsorption is $22.68 \text{ kJ}\cdot\text{mol}^{-1}$ indicating that the adsorption falls in the range of a physisorption process and has a low potential barrier. The results of the present investigation indicate that TKC has a suitable adsorption capacity for the removal of BF dye in wastewater. These results, therefore, are of great importance for the removal of toxic dyes from wastewater and sewage and applied to real sample wastewater.

Data Availability

The authors confirm that the data supporting the findings of this study are available within the article.

Conflicts of Interest

The authors declare that they have no conflicts of interest.

Authors' Contributions

F. Radha, D. Shwan, and S. Kaufhold were responsible for the conceptualization. D. Shwan was responsible for the methodology. D. Shwan and S. Kaufhold were responsible for the software. D. Shwan and S. Kaufhold were responsible for the validation. F. Radha and D. Shwan were responsible for the formal analysis. D. Shwan and S. Kaufhold were responsible for the investigation. F. Radha and D. Shwan were responsible for the resources. F. Radha, D. Shwan, and S. Kaufhold were responsible for the data curation. F. Radha and D. Shwan were responsible for the writing—original draft preparation. D. Shwan and S. Kaufhold were responsible for the writing—review and editing. F. Radha and D. Shwan were responsible for the visualization. D. Shwan and S. Kaufhold were responsible for the supervision. All of the authors worked on the manuscript, read the final version, and approved it.

Acknowledgments

We gratefully acknowledge the Komar University, MLS Department, for providing the real sample for the application of the present study and all who contributed to the conduction of this study especially Mr. Karokh B. Ali, Hassan H. Amin, and Dlzar D. Ghafoor.

References

- [1] M. El-Azazy, A. S. El-Shafie, A. Ashraf, and A. A. Issa, "Eco-structured biosorptive removal of basic fuchsin using pistachio nutshells: a definitive screening design-based approach," *Applied Sciences*, vol. 9, no. 22, p. 4855, 2019.
- [2] M. El Haddad, "Removal of basic fuchsin dye from water using mussel shell biomass waste as an adsorbent: equilibrium, kinetics, and thermodynamics," *Journal of Taibah University for Science*, vol. 10, no. 5, pp. 664–674, 2016.
- [3] H. S. Rai, S. Singh, P. P. S. Cheema, T. K. Bansal, and U. C. Banerjee, "Decolorization of triphenylmethane dye-bath effluent in an integrated two-stage anaerobic reactor," *Journal of Environmental Management*, vol. 83, no. 3, pp. 290–297, 2007.
- [4] V. K. Gupta, A. Mittal, V. Gajbe, and J. Mittal, "Adsorption of basic fuchsin using waste materials—bottom ash and deoiled soya—as adsorbents," *Journal of Colloid and Interface Science*, vol. 319, no. 1, pp. 30–39, 2008.
- [5] E. Kalkan, H. Nadaroglu, N. Celebi, H. Celik, and E. Tasgin, "Experimental study to remediate acid fuchsin dye using laccase-modified zeolite from aqueous solutions," *Polish Journal of Environmental Studies*, vol. 24, no. 1, pp. 115–124, 2015.
- [6] A. D. Sponza, N. J. Fernandez, D. Yang, K. A. Ortiz, and A. E. Navarro, "Comparative sorption of methylene blue onto hydrophobic clays," *Environments*, vol. 2, no. 4, pp. 388–398, 2015.
- [7] H. Nadaroglu, E. Kalkan, and N. Celebi, "Adsorption performance of laccase modified-red mud for acid fuchsin dye removal from aqueous solutions," *Annals of Chromatography and Separation Techniques*, vol. 3, no. 1, p. 1027, 2017.

- [8] H. Nadaroglu, E. Kalkan, and N. Celebi, "Removal of reactive black 5 from wastewater using natural clinoptilolite modified with apolaccase," *Clay Minerals*, vol. 50, pp. 65–76, 2015.
- [9] Y. Zhao, J. Geng, J. Cai, Y. F. Cai, and C. Y. Cao, "Adsorption performance of basic fuchsin on alkali-activated diatomite," *Adsorption Science & Technology*, vol. 38, no. 5-6, pp. 151–167, 2020.
- [10] G. S. Gupta, G. Prasad, K. K. Panday, and V. N. Singh, "Removal of chrome dye from aqueous solutions by fly ash," *Water, Air, and Soil Pollution*, vol. 37, pp. 13–24, 1988.
- [11] M. N. Ahmed and R. N. Ram, "Removal of basic dye from waste-water using silica as adsorbent," *Environmental Pollution*, vol. 77, no. 1, pp. 79–86, 1992.
- [12] Y. S. Ho and G. McKay, "Kinetic models for the sorption of dye from aqueous solution by wood," *Process Safety and Environmental Protection*, vol. 76, no. 2, pp. 183–191, 1998.
- [13] R. T. Yamuna and C. Namasivayam, "Color removal from aqueous solution by biogas residual slurry," *Toxicological and Environmental Chemistry*, vol. 38, no. 3–4, pp. 131–143, 1993.
- [14] C. A. P. Almeida, N. A. Debacher, A. J. Downs, L. Cottet, and C. A. D. Mello, "Removal of methylene blue from colored effluents by adsorption on montmorillonite clay," *Journal of Colloid and Interface Science*, vol. 332, no. 1, pp. 46–53, 2009.
- [15] Z. Boubberka, A. Khenifi, N. Benderdouche, and Z. Derriche, "Removal of supranol yellow 4GL by adsorption onto Cr-intercalated montmorillonite," *Journal of Hazardous Materials*, vol. 133, no. 1–3, pp. 154–161, 2006.
- [16] D. M. Salh, B. K. Aziz, and S. Kaufhold, "High adsorption efficiency of Topkhana natural clay for methylene blue from medical laboratory wastewater: a Linear and Nonlinear Regression," *Silicon*, vol. 12, no. 1, pp. 87–99, 2020.
- [17] Y. S. Choi and J. H. Cho, "Color removal from dye wastewater using vermiculite," *Environmental Technology*, vol. 17, no. 11, pp. 1169–1180, 1996.
- [18] M. Toprak, A. Salci, and A. R. Demirkiran, "Comparison of adsorption performances of vermiculite and clinoptilolite for the removal of pyronine Y dyestuff," *Reaction Kinetics, Mechanisms and Catalysis*, vol. 111, no. 2, pp. 791–804, 2014.
- [19] X. Yu, C. Wei, and H. Wu, "Effect of molecular structure on the adsorption behavior of cationic dyes onto natural vermiculite," *Separation and Purification Technology*, vol. 156, pp. 489–495, 2015.
- [20] F. Papers, "Efficient adsorption and photocatalytic degradation of dyes by AgI-Bi₂MoO₆/Vermiculite composite under visible Light," *ChemistrySelect*, vol. 4, no. 41, pp. 12022–12031, 2019.
- [21] M. F. Brigatti, E. Galán, and B. K. G. Theng, "Structure and mineralogy of clay minerals," *Developments in Clay Science*, vol. 5, 2013.
- [22] W. Bleam, "Clay Mineralogy and Chemistry," *Soil and Environmental Chemistry*, vol. 2, pp. 87–146, 2017.
- [23] R. Lan, J. Li, and B. Chen, "Ultrasonic degradation of fuchsin basic in aqueous solution: effects of operating parameters and additives," *International Journal of Photoenergy*, vol. 2013, Article ID 893131, 7 pages, 2013.
- [24] R. Cruz, "Chemical and structural evolution of 'metamorphic vermiculite' in metaclastic rocks of the Betic Cordillera, Málaga, Spain: a synthesis," *The Canadian Mineralogist*, vol. 44, no. 1, pp. 249–265, 2006.
- [25] M. Arab, D. Bougeard, and K. S. Smirnov, "Experimental and computer simulation study of the vibrational spectra of vermiculite," *Physical Chemistry Chemical Physics*, vol. 4, no. 10, pp. 1957–1963, 2002.
- [26] S. Hillier and B. Velde, "Chlorite interstratified with a 7 Å mineral: an example from offshore Norway and possible implications for the interpretation of the composition of diagenetic chlorites," *Clay Minerals*, vol. 27, no. 4, pp. 475–486, 1992.
- [27] F. A. Andersen, L. Brecevic, G. Beuter et al., "Infrared spectra of amorphous and crystalline calcium carbonate," *Acta Chemica Scandinavica*, vol. 45, pp. 1018–1024, 1991.
- [28] S. Banerjee and M. C. Chattopadhyaya, "Adsorption characteristics for the removal of a toxic dye, tartrazine from aqueous solutions by a low cost agricultural by-product," *Arabian Journal of Chemistry*, vol. 10, pp. S1629–S1638, 2017.
- [29] M. Wawrzkiwicz and Z. Hubicki, "Removal of tartrazine from aqueous solutions by strongly basic polystyrene anion exchange resins," *Journal of Hazardous Materials*, vol. 164, no. 2-3, pp. 502–509, 2009.
- [30] E. O. Oyelude, F. Frimpong, and D. Dawson, "Studies on the removal of basic fuchsin dye from aqueous solution by HCl treated malted sorghum mash," *Journal of Materials and Environmental Science*, vol. 6, no. 4, pp. 1126–1136, 2015.
- [31] P. Taylor, D. Prabu, R. Parthiban, P. S. Kumar, N. Kumari, and P. Saikia, "Desalination and water treatment adsorption of copper ions onto nano-scale zero-valent iron impregnated cashew nut shell," *Desalination and Water Treatment*, vol. 57, no. 14, pp. 37–41, 2016.
- [32] P. K. Baskaran, B. R. Venkatraman, and S. Arivoli, "Kinetics of adsorption of ferrous ion onto acid activated carbon from Zea mays dust," *E-Journal of Chemistry*, vol. 8, no. 1, pp. 185–195, 2011.
- [33] Y. S. Ho, "Citation review of Lagergren kinetic rate equation on adsorption reactions," *Scientometrics*, vol. 59, no. 1, pp. 171–177, 2004.
- [34] Y. S. Ho and G. McKay, "Pseudo-second order model for sorption processes," *Process Biochemistry*, vol. 34, no. 5, pp. 451–465, 1999.
- [35] M. S. Chiou and H. Y. Li, "Adsorption behavior of reactive dye in aqueous solution on chemical cross-linked chitosan beads," *Chemosphere*, vol. 50, no. 8, pp. 1095–1105, 2003.
- [36] M. H. Armbruster and J. B. Austin, "The adsorption of gases on plane surfaces of mica," *Journal of the American Chemical Society*, vol. 60, no. 2, pp. 467–475, 1938.
- [37] S. N. Hurairah, N. M. Lajis, and A. A. Halim, "Methylene blue removal from aqueous solution by adsorption on Archidendron jiringa seed shells," *Journal of Geoscience and Environment Protection*, vol. 8, no. 2, pp. 128–143, 2020.
- [38] J. Appel, "Freundlich's adsorption isotherm," *Surface Science*, vol. 39, no. 1, pp. 237–244, 1973.
- [39] A. K. Meena, K. Kadirvelu, G. K. Mishra, C. Rajagopal, and P. N. Nagar, "Adsorption of Pb(II) and Cd(II) metal ions from aqueous solutions by mustard husk," *Journal of Hazardous Materials*, vol. 150, no. 3, pp. 619–625, 2008.
- [40] L. Cottet, C. A. P. Almeida, N. Naidek, M. F. Viante, M. C. Lopes, and N. A. Debacher, "Adsorption characteristics of montmorillonite clay modified with iron oxide with respect to methylene blue in aqueous media," *Applied Clay Science*, vol. 95, pp. 25–31, 2014.
- [41] S. Hong, C. Wen, J. He, F. Gan, and Y. S. Ho, "Adsorption thermodynamics of methylene blue onto bentonite," *Journal of Hazardous Materials*, vol. 167, no. 1–3, pp. 630–633, 2009.

Research Article

Mesoscopic Process Simulation of In Situ Leaching of Ionic Rare Earth Based on NMRI Technology

Fuyu Wu ¹, Dan Wang ², Yunzhang Rao ^{1,2}, Meidao Zhang², Liang Shi ^{1,2}, Min Han,² and Wei Xu^{2,3}

¹School of Civil and Surveying & Mapping Engineering, Jiangxi University of Science and Technology, Ganzhou 341000, China

²School of Resources and Architectural Engineering, Jiangxi University of Science and Technology, Ganzhou 341000, China

³The Seventh Geological Brigade of Jiangxi Bureau of Geology, Ganzhou 341000, China

Correspondence should be addressed to Yunzhang Rao; raoyunzhang@jxust.edu.cn

Received 31 August 2022; Revised 18 October 2022; Accepted 25 November 2022; Published 8 March 2023

Academic Editor: Juan A. Cecilia

Copyright © 2023 Fuyu Wu et al. This is an open access article distributed under the Creative Commons Attribution License, which permits unrestricted use, distribution, and reproduction in any medium, provided the original work is properly cited.

In order to simulate and calculate the leaching process of ionic rare earths more realistically, a digital model of ionic rare earths with real size, shape, seepage channel, and pore ratio and distribution at the mesoscopic scale was constructed based on nuclear magnetic resonance imaging (NMRI) technology. And the in situ leaching mining process was simulated and calculated by using three control equations of solution seepage, ion exchange, and solute migration. The reliability of the NMRI model was verified by the results of the indoor column leaching experiment, and the influence of the injection intensity and leaching agent concentration on the leaching of rare earth ions was analyzed. The results show that there are dominant seepage channels in the ore body, and the rare earth ion exchange reaction and migration in the dominant channel area are completed first. By analyzing the leaching results of rare earth ions under the working conditions of different injection strengths and different concentrations of leaching agent, the results show that the injection strength and the concentration of leaching agent have an obvious promoting effect on the leaching of rare earth ions in a certain range. The injection strength of 0.5~1.0 mL/min and the concentration of 0.20~0.25 mol/L leaching agent are considered to be more economical in practical engineering.

1. Introduction

Ion-adsorbed rare earth minerals are mainly distributed in the south of China and are named for rare earth elements adsorbed in the form of cations on the surface of clay minerals weathered by granite or volcanic rocks. They are unique and important rare earth minerals in China [1, 2]. Rare earth cations adsorbed on the surface of clay minerals undergo ion exchange reaction in strong electrolyte solution and enter the solution [3]. Based on this characteristic, in situ leaching technology is developed to mine such rare earth minerals [4, 5]. In the actual promotion and application process of this technology, key issues such as leaching cycle, leaching rare earth concentration, and leaching efficiency have always been the focus of technical personnel and scientific researchers in the industry [6–8].

At present, many researchers describe the leaching process by establishing numerical models [9–11] and study the leaching process and mechanism by means of numerical simulation. Sheikhzadeh et al. [12] established an unsteady two-dimensional model of the unsaturated flow of the liquid in the uniform spherical ore bed based on the mass conservation equation of the liquid phase in the ore bed and the particles and solved the model with the full implicit finite difference method and obtained the influence of the periodic permeability of water on the saturation and vertical velocity distribution in the ore body. Liu et al. [13] established the governing equation for the elastic deformation seepage of ore and the governing equation for mass transfer, solved the two governing equations through porosity coupling, and simulated the change law of the concentration of leaching agent and leaching ion in constant head leaching. Hu et al. [14] used Kerr model, Vanselow model, and Gapon

model to describe the solid-phase rare earth ion exchange process; analyzed the error between the calculated value and the test value under those three models; and proposed the suggestion of using Kerr model to describe the solid-phase rare earth ion exchange process. Long et al. [15] used the convective dispersion equation to describe the solute transport process in the one-dimensional column leaching test of ionic rare earth and analyzed the influence of different concentrations of leaching agents on the leaching rate of rare earth. Wu et al. [16, 17] established a fully coupled flow-reaction-deformation-mass transfer model in the leaching process on the basis of the original results, considering the deformation factors of ore in the leaching process, and studied the distribution of porosity, saturation, leaching agent concentration, and leached ore concentration in the ore pile under the condition of one-dimensional fixed spray and fixed water head. Based on the mass conservation of fluid and solute, combined with the influence of consolidation effect on soil mass, Tan [18] established a coupled numerical model of seepage-reaction-stress of ionic type rare earth in situ leaching and studied the distribution and space-time evolution of seepage field, stress field, and concentration field under different injection pressure, axial pressure, and confining pressure factors during column leaching, respectively.

Most of the previous studies treated ore bodies as homogeneous porous media without considering the influence of the nonuniformity of particle size and the disorder of particle distribution on the seepage flow of rare earth ore bodies [19–21]. With the development of testing technology, more and more researchers try to use NMRI, CT, and other technologies to study the internal pore structure of ore bodies. Ma et al. [22, 23] used CT technology to collect pore images of ore and rock granular media and found that the porosity of ore and rock media in heap leaching system had spatial and temporal variability. Li et al. [24] established the ore body pore model of different layers of ion-type rare earth ore through CT scanning technology and analyzed the influence of ion-type rare earth cavity process on the ore body pore network. Yang et al. [25] explored the microstructure change rule of ion-type rare earth ore body during leaching by NMRI technology and analyzed the influence of leaching agent pH on the leaching rule of ion-type rare earth.

In order to reflect the real seepage channel and the process of complex ion exchange and migration in the rare earth ore body, this paper constructed the seepage channel in rare earth ore body by NMRI technology and established a numerical model of seepage-exchange-migration in situ leaching of ionic rare earth on the basis of Navier-Stokes equation, exchange reaction equation, and convection-diffusion equation. COMSOL Multiphysics multiphysical field coupling software was used to study the seepage-exchange-migration evolution law in the leaching process under different injection strengths and leaching agent concentrations and analyze the effect of this law on the leaching of rare earth ions.

2. Theory and Model

In the process of ionic rare earth in situ leaching, the leaching agent enters the interior of the ore body through the liq-

uid injection hole and reacts with the rare earth ions adsorbed on the surface of the ore body to make them parse and leach out along with the seepage process [26, 27]. As shown in Figure 1, according to the ionic rare earth leaching kinetics of related research [28, 29], ionic rare earth leaching process, the leaching agent (taking magnesium sulphate solution as an example) first contacts with the liquid film layer on the surface of the rare earth ore particles. The magnesium ions in the leaching agent contact with the surface of the mineral particles through diffusion (liquid film diffusion) and then exchange with the rare earth ions on the surface of the ore body particles. After the ion exchange reaction between rare earth ions and magnesium ions, rare earth ions are resolved from the surface of the ore body, while magnesium ions are adsorbed to the particle surface of the ore body (ion exchange reaction). In the process of exchange reaction, magnesium ions can reach the surface of rare earth ion adsorption only through diffusion through the solid film layer of magnesium ion adsorption, and ion exchange reaction occurs with the adsorbed rare earth ions (solid film diffusion). The exchange rare earth ions enter the leaching agent by diffusion and exude the ore body with the leaching agent, so that the leaching process of rare earth ions is completed.

From this point of view, the efficient leaching of rare earth ions is not only related to the seepage of leaching agent and ion migration but also closely related to the ion exchange reaction on the particle surface of ore body. Therefore, the leaching process of rare earth ions can be regarded as a coupling process of seepage, exchange reaction, and ion migration.

2.1. Flow Control Equation. Assuming that the leaching agent is incompressible, its flow process in the pores of the ore body can be described by the Navier-Stokes equation [30], and the continuity equation is as follows:

$$\nabla \cdot \mathbf{u} = 0, \quad (1)$$

where \mathbf{u} is the velocity vector of the fluid (m/s). The equation of motion is as follows:

$$\rho \left[\frac{\partial \mathbf{u}}{\partial t} + (\mathbf{u} \cdot \nabla) \mathbf{u} \right] = \nabla \cdot \left[-p\mathbf{I} + \mu(\nabla \mathbf{u}) + (\nabla \mathbf{u})^T \right] + \mathbf{F}, \quad (2)$$

where p is fluid pressure (Pa); ρ is the fluid density (kg/m^3); μ is hydrodynamic viscosity; \mathbf{I} is a unit tensor; t is time (s); and \mathbf{F} is the volume force vector (N/m^3).

2.2. Ion Exchange Governing Equations. When the leaching agent flows in the pore, it also exchanges with rare earth ions adsorbed on the particle surface of the ore body [31]. It is assumed that rare earth ions adsorbed on the particle surface of the ore body transfer along the tangential direction of the surface, and this process can be described by Fick's law:

$$N_{t,i} = -D_{s,i} \nabla_t c_{s,i}, \quad (3)$$

where $N_{t,i}$ is the surface molar flux, $\text{mol}/(\text{m} \cdot \text{s})$; $D_{s,i}$ is the

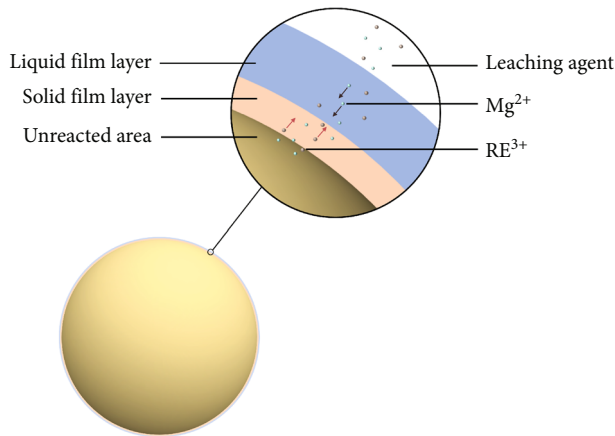


FIGURE 1: Schematic diagram of the rare earth ion exchange reaction.

surface diffusion coefficient of the substance i (m^2/s); and $c_{s,i}$ is the concentration of surface material i (mol/m^2). The governing equation of each substance concentration on the particle surface of the ore body is as follows:

$$\frac{\partial c_{s,i}}{\partial t} = -\nabla_t \cdot N_{t,i} + R_{s,i}, \quad (4)$$

where $R_{s,i}$ is the sum of source terms caused by surface reaction and adsorption analytical phenomenon ($\text{mol}/(\text{m}^2 \cdot \text{s})$).

2.3. Solute Transport Governing Equation. After the exchange reaction, the rare earth ions enter the leaching agent and migrate in the ore body with the seepage process [32]. Considering convection and diffusion, the migration process of rare earth ions with leaching agent between pores of the ore body can be described by the convection-diffusion equation:

$$\frac{\partial c_i}{\partial t} + u \cdot \nabla c_i = R_i + \nabla \cdot D_i \nabla c_i, \quad (5)$$

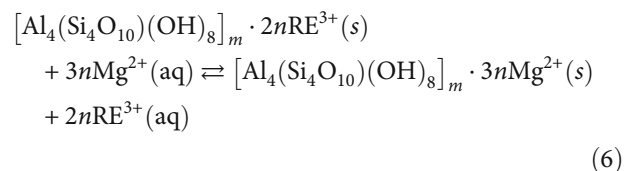
where c_i is the concentration of substance i (mol/m^3); D_i is the diffusion coefficient of the substance i (m^2/s); R_i is the reaction rate of the substance i ($\text{mol}/(\text{m}^3 \cdot \text{s})$); and u is the velocity vector of the fluid (m/s).

3. Model Establishment and Reliability Verification

3.1. Model Establishment. In the process of in situ leaching of ionic rare earth, the leaching agent fills the pores inside the ore body. The principle of magnetic resonance imaging is the resonance phenomenon of hydrogen protons under the action of strong magnetic field. The magnetic resonance imaging is obtained by data reconstruction of resonance trajectory data. In addition, the nuclear magnetic resonance test has the advantages of simple operation and accurate data, which provides convenience for the imaging of ion-type rare earth pore seepage channels in saturated state. The test samples on this paper were collected from an ionic rare earth

mining area in Longnan County, Ganzhou City, Jiangxi Province. As shown in Figure 2, in order to obtain a more real internal pore structure of ionic rare earth ore body, in situ leaching stope, Luoyang shovel was used to dig to the bottom of the topsoil layer, a transparent acrylic pipe with a length of 300 mm and a diameter of 42 mm was driven into the ore body, and the tube body was drawn out to obtain a section of undisturbed ore body. A section of cylindrical sample with a height of 100 mm was intercepted, part of mineral soil at both ends of the sample was removed, and permeable stone was inserted to seal both ends of the sample. The samples were saturated with water for 48 h, so that the pores of the cylindrical sample will be filled with water. In order to eliminate the disturbance caused by sample interception and closed treatment, a nuclear magnetic resonance instrument (manufacturer: Suzhou Niumai Analytical Instrument Production Co., LTD., model: MesomR23-060H-I) was used to scan and image the 60 mm length of the sample in the middle of the sample in the axial direction. In the gray scale map of pore imaging generated, the higher the water content of ore samples, the stronger the NMR signal, and the brighter the pixels displayed in the image [33]. In order to reflect the characteristics of mineral soil aggregate structure, Mimics image control software was used to perform light source correction, image segmentation, filtering, and denoising on the image to digitize the solid phase skeleton and pore channels [34] and generate a two-dimensional geometric model of $42 \text{ mm} \times 60 \text{ mm}$ (hereinafter referred to as the NMRI model).

The upper and lower boundaries of the model are inlet and outlet boundaries, respectively, and the left and right boundaries are flux-free boundaries. The wall of the seepage channel is the “surface region,” and the leaching agent exchanges with the rare earth ion adsorbent on the “surface region.” It is assumed that only the rare earth ions represented by yttrium (Y) element are uniformly distributed on the surface region, with a concentration of $0.12 \text{ mol}/\text{m}^2$. Studies on the leaching kinetics of in situ leaching show that [35, 36] mineral ion leaching is a process controlled by surface reaction, which is mainly affected by the exchange rate of leaching agent cation and mineral cation in leaching agent. In this study, magnesium sulphate solution is considered a leaching agent [37], and the chemical reaction equation between magnesium ion and rare earth ion can be expressed as follows:



According to the above chemical reaction equation, the related exchange reaction rate, diffusion coefficient, and dispersion coefficient were calculated by the “reaction engineering” interface in COMSOL Multiphysics multiphysical coupling software. The model was imported into that software for coupling solution of the above governing equations.

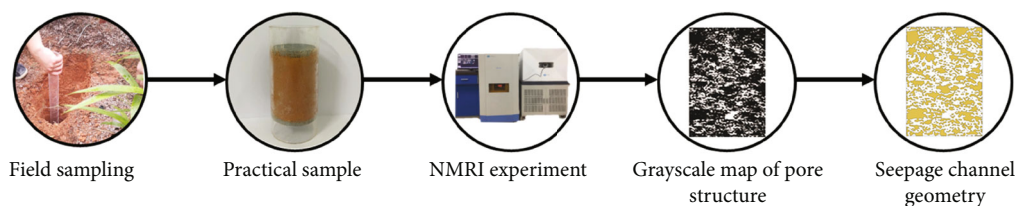


FIGURE 2: Construction steps of the NMRI model.

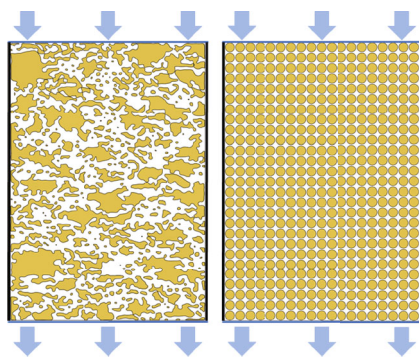


FIGURE 3: NMRI model and uniform model.

3.2. Test Method. In this study, the conditions of leaching agent concentration of 0.25 mol/L and injection strength of 1.0 mL/min were selected, and the uniform two-dimensional geometric model (hereinafter referred to as the uniform model) and the results of laboratory experiment were used for comparison with the NMRI model for validation.

As shown in Figure 3, it is assumed that the porosity of the uniform model is consistent with that of the unchanged ore sample measured in the laboratory test to be 0.37, and the particle diameter is 1.985 mm, and it is uniformly distributed in the model of 42 mm × 60 mm. The initial and boundary conditions are consistent with the NMRI model.

As shown in Figure 4, the ore sample selected for the indoor leaching test is the ore sample in the same interception section of nuclear magnetic imaging, and the leaching mother liquor is collected at the outlet end, and the content of rare earth ions in the mother liquor is measured by EDTA volumetric method (measured every 10 min and recorded) [38].

3.3. Verification of Simulation Results. Figure 5 shows the comparison between experimental results and simulation results of the average concentration of leached rare earth ions (hereinafter referred to as leaching concentration) changing with time under the condition of injection strength 1.0 mL/min and leaching agent concentration 0.25 mol/L. It can be seen from the figure that the change of leaching concentration over time in the NMRI model is similar to that in the laboratory test: the leaching agent has not reached the outlet at the initial stage of liquid injection, and the leaching concentration remains at a low level. When the leaching agent flows out from the outlet, the leaching concentration gradually reaches the peak, and the peak leaching concentrations under the NMRI model and the laboratory experiment are 9.1 g/L and 7.8 g/L, respectively. With the continuous infusion, the leaching concentration continued to decrease

and gradually approached 0.0 g/L. At the same time, the decrease of rare earth ion concentration on the surface of ore body leads to the slowdown of chemical reaction rate, and the change rate of leaching rare earth ion concentration gradually decreases. According to the change of leaching concentration with time, the leaching process of the NMRI model and laboratory test can be divided into initial stage, ascending stage, peak stage, descending stage, and trailing stage. However, the variation of the average concentration of leached rare earth ions under the uniform model is quite different from that of the former two models. The difference is shown in the rising stage. The difference is shown in that the leaching concentration rises rapidly to the peak value of 13.1 g/L in a short time, during which there is a period of slow decline, and then enters a sharp descent process (the leaching concentration plummets to 0.0 g/L). The leaching process of the uniform model can be summarized as initial stage, ascending stage, peak stage, slow descent stage, and sharp descent stage.

Figure 6 shows the steady-state flow field cloud images of the uniform model and the NMRI model. In the uniform model, the distribution of the flow field around a single particle shows a certain regularity: the flow velocity on the left and right sides of the particle is larger, and the flow velocity at the smaller channel width is larger, and the maximum flow velocity can reach 6×10^{-5} m/s. The velocity at the upper and lower ends of the particle is very small, with the lowest velocity close to 0 m/s. The flow field in the NMRI model is more complex than that in the uniform model. On the whole, there is a dominant channel near the middle line in the vertical direction of the geometric model, which is divided into two tributaries from top to bottom. The flow velocity in the dominant channel area is larger than that in the nondominant channel area, and the maximum flow velocity can reach 6×10^{-4} m/s. The distribution of the flow field around a single particle is irregular, and the velocity at different locations is different.

Figure 7 shows the distribution cloud of rare earth ion concentration of the uniform model and the NMRI model at different times. In the uniform model, the particle size is small and the distribution is uniform, the leaching agent percolates uniformly downward in the pore, and the degree of rare earth ion exchange reaction is the same at the same level height, making the exchange reaction mainly concentrated in 25-170 min. However, the particle size and particle distribution of the NMRI model are nonuniform, and the flow field is more complex than that of the uniform model, which is similar to the seepage situation of ion-type rare earth minerals under real conditions. The exchange reaction in the

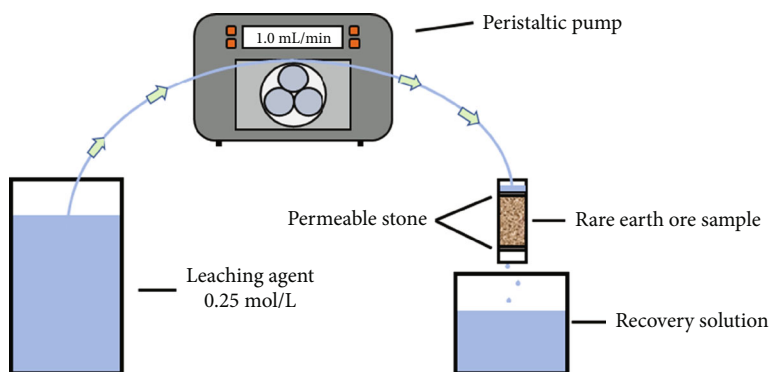


FIGURE 4: Schematic diagram of laboratory test.

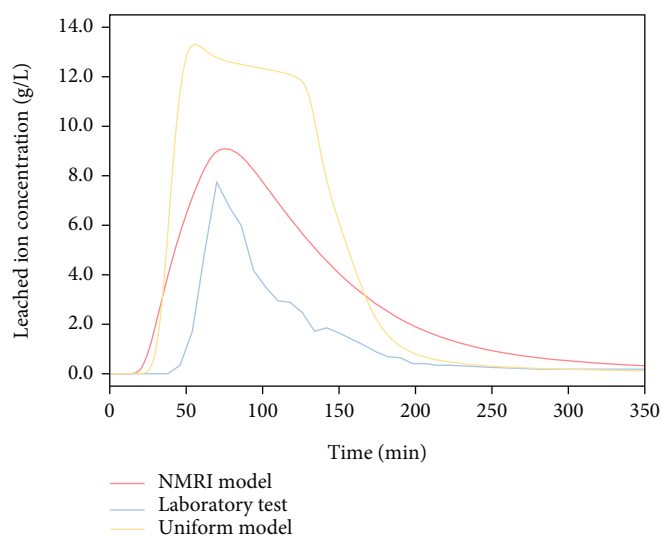


FIGURE 5: The comparison between the experimental value and the simulated value of the leaching concentration.

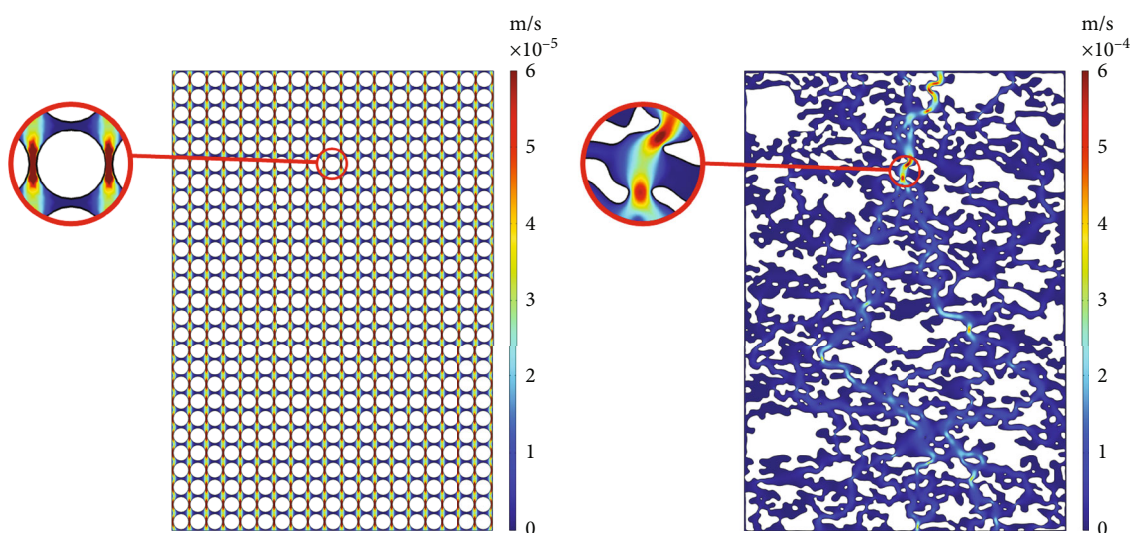


FIGURE 6: Steady-state flow field of the NMRI model and uniform model.

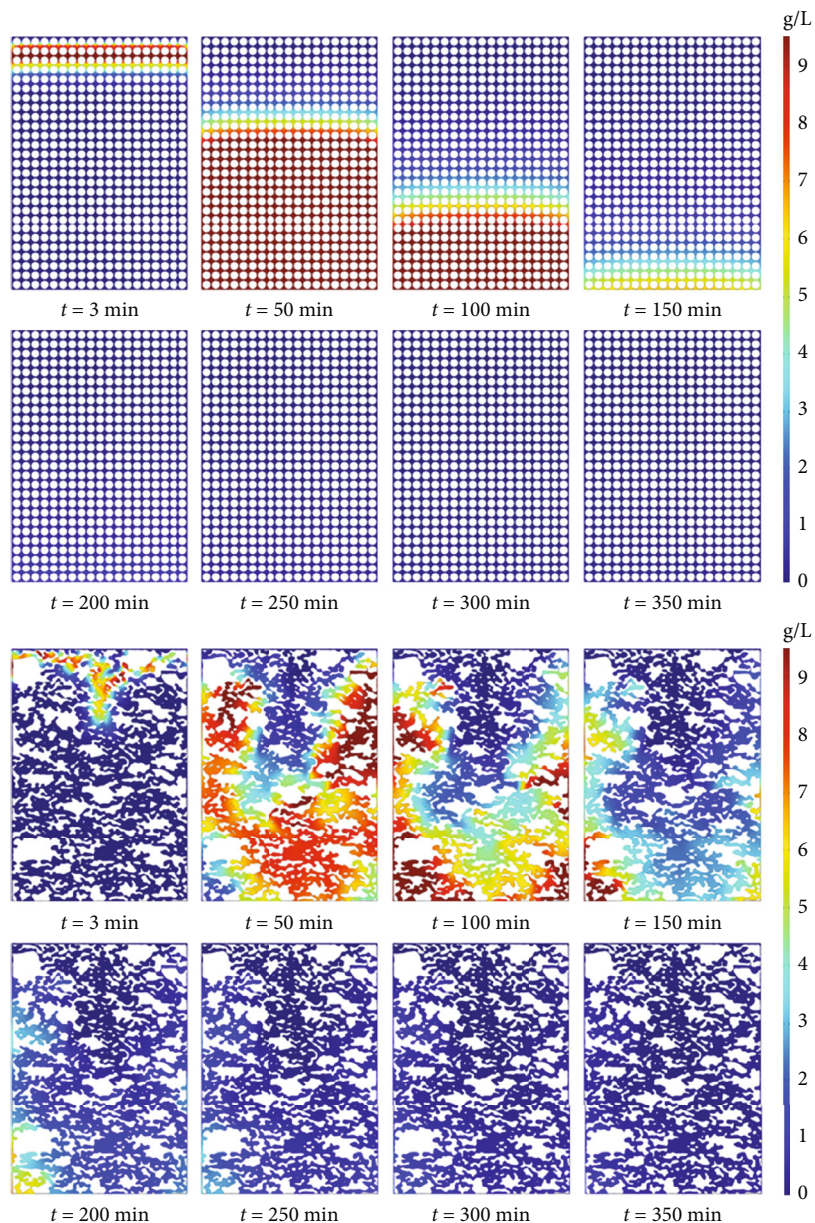


FIGURE 7: RE^{3+} ion migration processes in the NMRI model and uniform model.

dominant channel region occurred preferentially than that in the nondominant channel, and the exchange reaction lasted from 11 to 270 min. Therefore, the nonuniform model can reflect the exchange and migration of rare earth ions during in situ leaching to a certain extent.

4. Results and Discussion

4.1. Effect of Injection Strength on Leaching of Rare Earth Ions. In order to deeply understand the influence of the injection intensity on the leaching of rare earth ions, this study adopts the NMRI model and keeps the leaching agent concentration of 0.2 mol/L constant. The seepage-exchange-migration process of saturated leaching ore under different injection intensities (0.2 mL/min, 0.5 mL/min, 1.0 mL/min, and 2.0 mL/min) was studied.

Figure 8 shows the steady flow field cloud diagram under different injection intensities. With the increase of injection strength, the difference of flow velocity between dominant channel area and nondominant channel area is more obvious, and the maximum flow velocity is 1.3×10^{-4} m/s, 3.2×10^{-4} m/s, 6.5×10^{-4} m/s, and 1.3×10^{-3} m/s, respectively. As the flow rate in the dominant channel is greater than that in the nondominant channel, the leaching agent passing quantity in the dominant channel is greater than that in the nondominant channel in unit time. The flow velocity in the nondominant region is smaller than that in the dominant region, and increasing the injection intensity has limited effect on the flow velocity in the nondominant region, so the flow velocity change in this region is not obvious.

As shown in Figure 9, when the injection intensity is 0.2 mL/min, the peak leaching concentration is 8.9 g/L; when

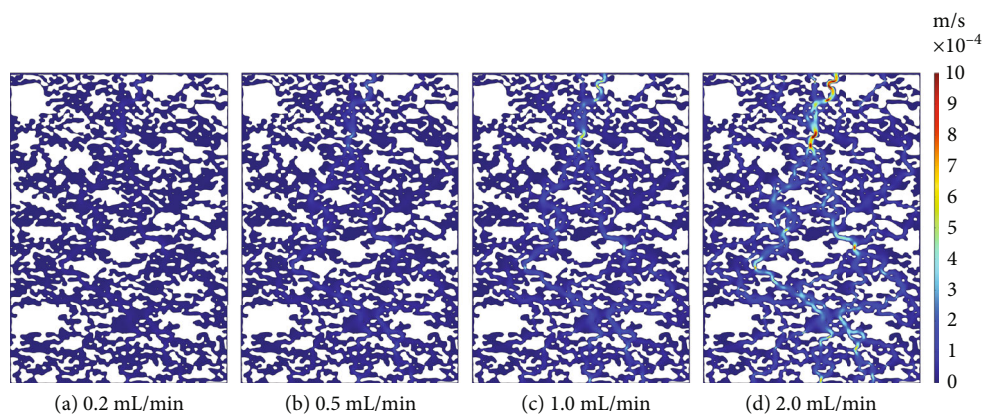


FIGURE 8: Steady-state flow field under different injection intensities.

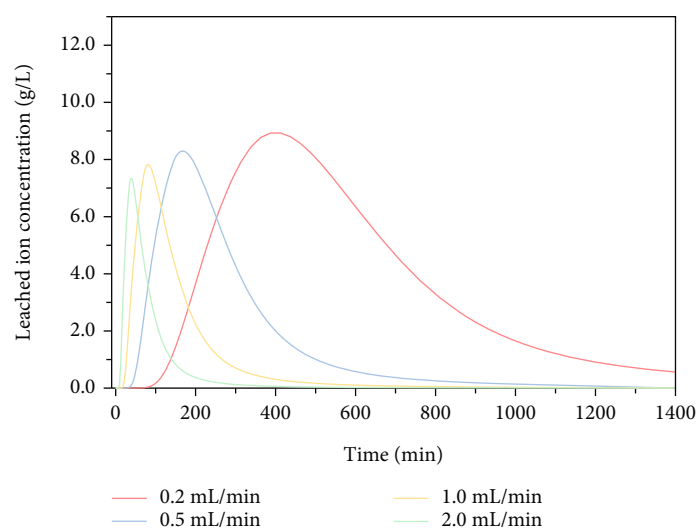


FIGURE 9: Variation curve of RE^{3+} ion leaching concentration under different injection intensities.

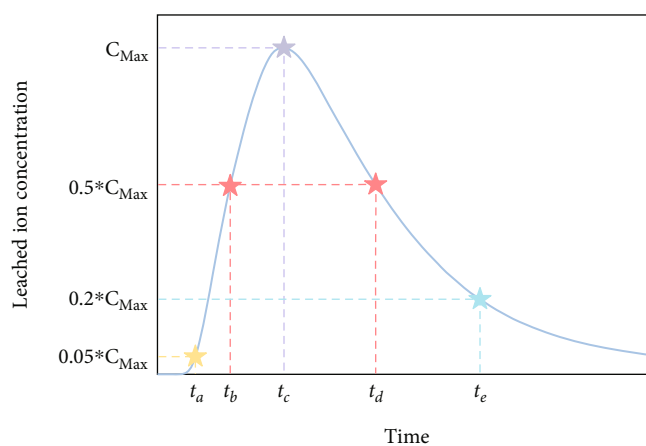


FIGURE 10: Schematic diagram of representative moments of rare earth ion leaching stage.

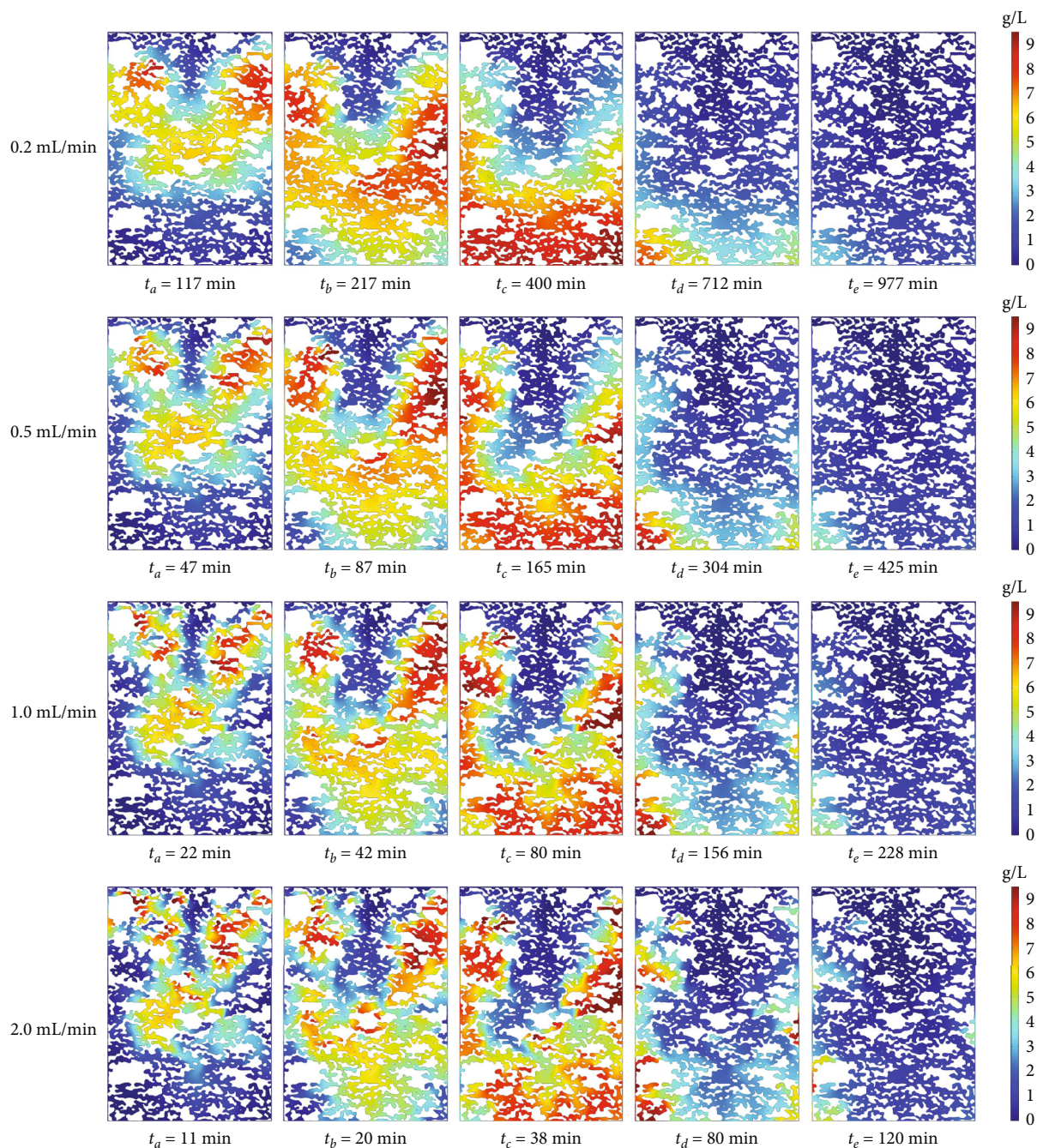


FIGURE 11: RE^{3+} ion migration process under different injection intensities.

the injection intensity increases to 0.5 mL/min, 1.0 mL/min, and 2.0 mL/min, the peak leaching concentration is 8.3 g/L, 7.8 g/L, and 7.3 g/L, respectively. This indicates that the peak concentration decreases with the increase of injection strength. At the same time, with the increase of liquid injection intensity, the corresponding time of peak concentration is $t = 400$ min, $t = 165$ min/ $t = 80$ min, and $t = 38$ min, and the leaching concentration curve moves forward as a whole, indicating that increasing the liquid injection intensity can accelerate the whole leaching process to a certain extent, to shorten the leaching cycle.

Taking the time corresponding to the peak concentration of 5% in the initial stage, corresponding to the peak concentration of 50% in the rising stage, corresponding to the peak concentration in the peak stage, corresponding to the peak concentration of 50% in the falling stage, and corresponding to the peak concentration of 20% in the trailing stage as the representative times of the corresponding stages (as shown in Figure 10), Figure 11 shows the distribution cloud diagram of leached rare earth ion concentration at each stage under different injection intensities. In the initial stage, the exchange reactions are mainly concentrated in the

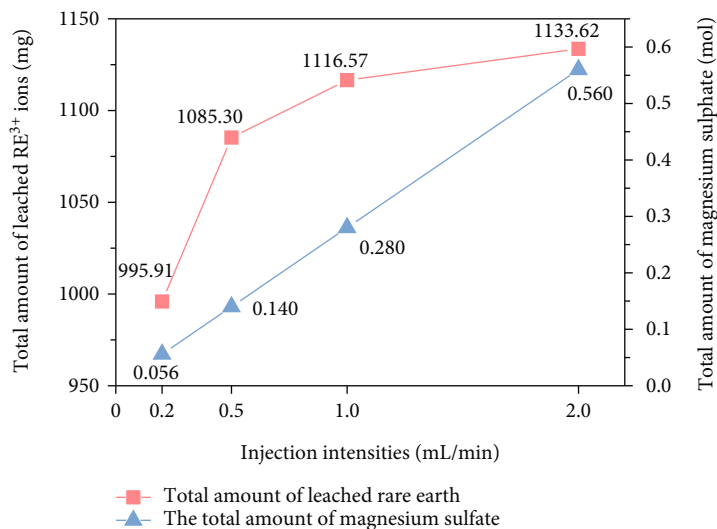


FIGURE 12: The total amount of leached RE³⁺ ions and the total amount of magnesium sulphate under different injection intensities.

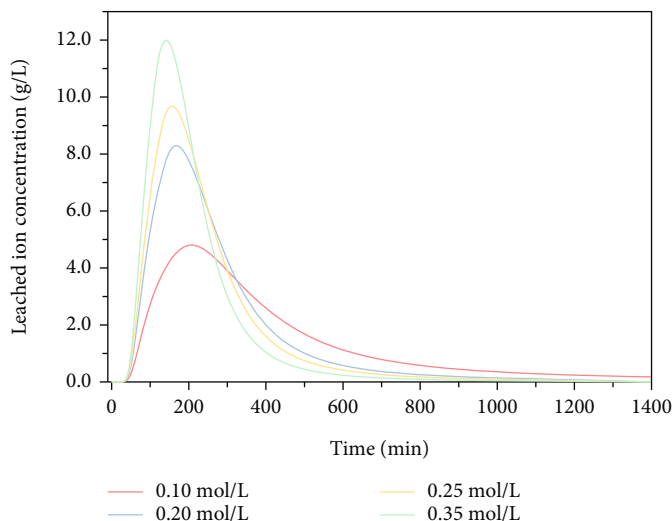


FIGURE 13: Variation curve of RE³⁺ ion leaching concentration with different leaching agent concentrations.

middle and upper part of the model. The surface reactions at the inlet end and the upper dominant channel are completed, and the rare earth ions migrate toward the outlet end with the leaching agent, so the concentration of rare earth ions there is low. In this stage, the replaced rare earth ions are mainly distributed in the upper nondominant channel and the middle dominant channel. The flow rate of the leaching agent in the nondominant channel is low, and the transport speed of leached rare earth ions in this region is less than that in the dominant channel, so the concentration of rare earth ions in the nondominant channel is higher at the same height at this stage. When the injection intensity increases, more leaching agents exchange reaction with the ore body in unit time, and the highest rare earth ion concentration in the upper nondominant channel also rises. Rising phase exchange reaction is mainly concentrated in the central model; the rare earth ions are mainly distributed in part of advantage channels and the upper advantage in the area;

this phase is an obvious advantage bigger than the channel, and the rare earth ion migration velocity of nondominant channel, rare earth ions in the nondominant channel, and highest concentration increase with liquid injection strength and rise. The exchange reactions in the peak stage are mainly concentrated in the middle and lower part of the model, and the rare earth ions are mainly distributed in the lower dominant channel and the middle and lower nondominant channel regions. When the injection intensity increases, the highest leached rare earth concentration in the middle nondominant channel increases, while the rare earth ion concentration in the lower region decreases. This is also mutually verified with the phenomenon that the peak leaching concentration decreases with the increase of injection strength. The exchange reactions in the descending stage and trailing stage are mainly on the left and right sides of the lower part of the model, and rare earth ions are mainly distributed in the lower nondominant channel region. When

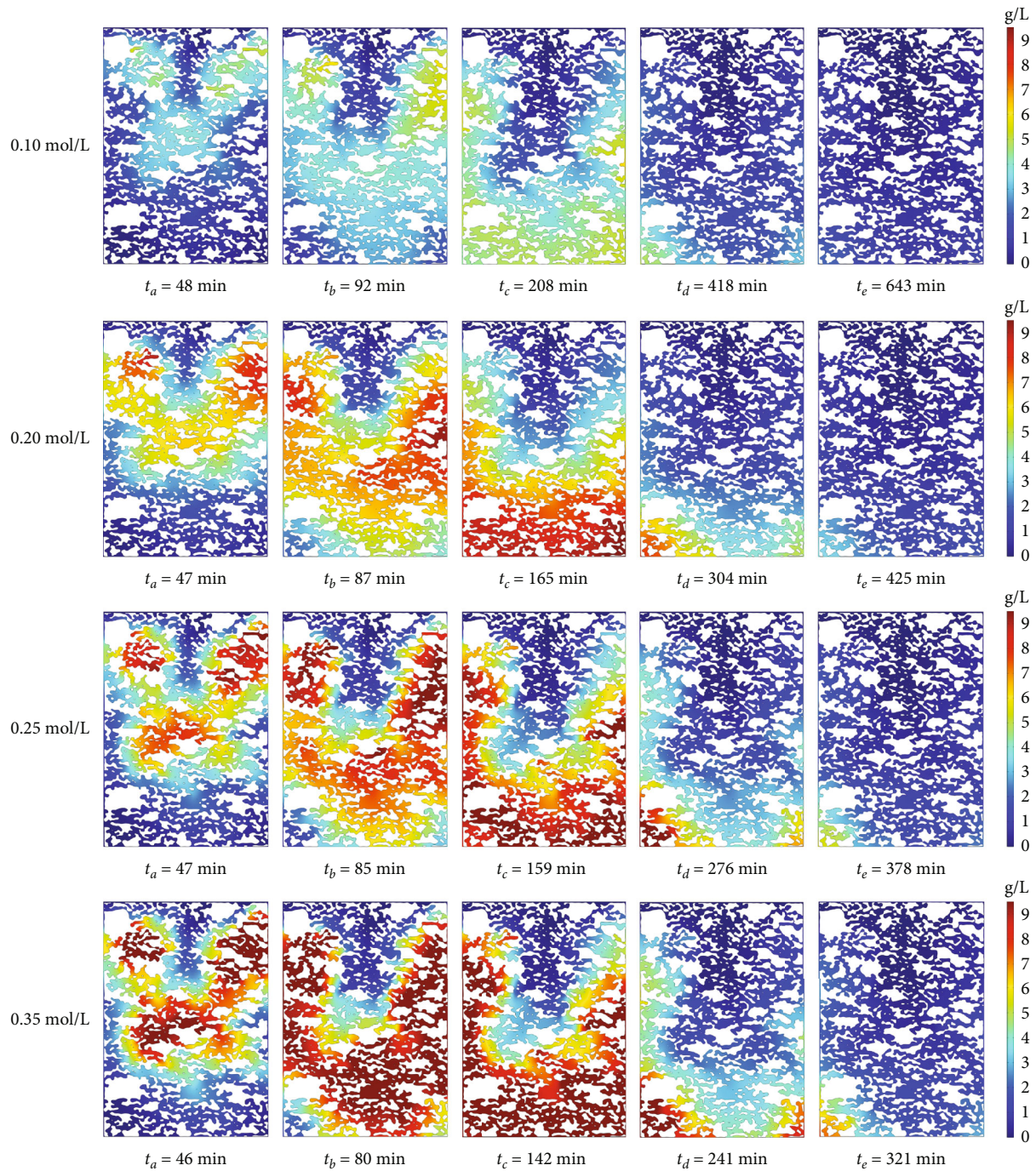


FIGURE 14: RE³⁺ ion migration process under different leaching agent concentrations.

the injection intensity increases, the overall concentration of rare earth ions in the middle and lower nondominant channel regions increases. It is obvious that the increase of injection intensity can promote the exchange reaction, and the rare earth ions in the nondominant channel region can be replaced more effectively. Convection in the dominant channel plays a dominant role in the migration of rare earth ions, while convection in the nondominant region has a relatively small effect on the migration of rare earth ions. Therefore, the migration velocity of rare earth ions in the dominant channel is greater than that in the nondominant region.

Figure 12 shows the total amount of leached rare earth ions and the total amount of magnesium sulphate under different injection strengths. It can be found from the figure that the total amount of magnesium sulphate (hereinafter referred to as the total amount) has a linear relationship with the intensity of the injection liquid, and the total amount of leached rare earth ions increases with the increase of the intensity of the injection liquid. Compared with 0.2 mL/min, the total dosage of 0.5 mL/min was increased by 150%, and the total amount of leached rare earth ions (hereinafter referred to as the total amount of leached) was

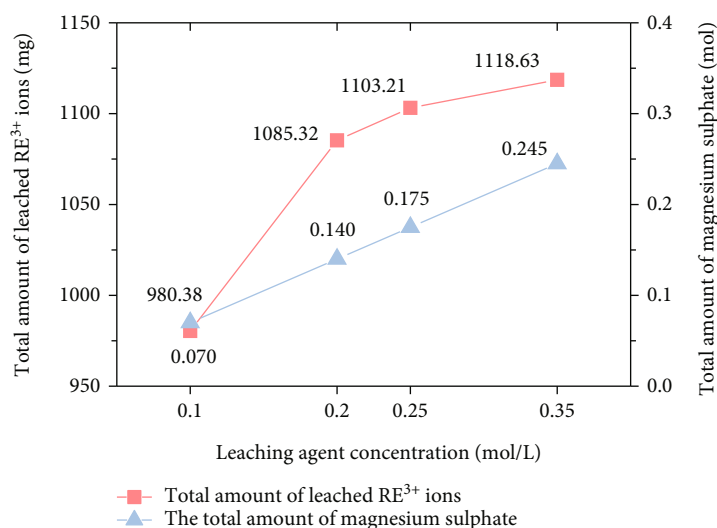


FIGURE 15: The total amount of leached RE³⁺ ions and the total amount of magnesium sulphate under different leaching agent concentrations.

increased by 8.9%; the total amount of 1.0 mL/min was increased by 100% compared with 0.5 mL/min, and the total amount of leaching was increased by 2.9%. Compared with 1.0 mL/min, the total dosage of 2.0 mL/min was increased by 100%, and the total leaching amount was increased by 1.5%. The increase of the total leaching amount decreased with the increase of the injection liquid intensity (i.e., the total dosage of magnesium sulphate). Combined with the analysis of the influence of liquid injection intensity on the flow velocity, it indicates that the limited effect of increasing liquid injection intensity on the flow velocity in the non-dominant channel leads to the limited effect of increasing liquid injection intensity on the promotion of ion exchange reaction in the region.

Therefore, it is obvious that the influence of liquid injection intensity on leaching of rare earth ions is mainly reflected in the following aspects: with the increase of liquid injection intensity, the flow rate of all parts of the seepage channel increases accordingly, and more leaching agents enter the ore body and react with rare earth ions within a unit time, which accelerates the migration velocity of leaching rare earth ions and accelerates the whole leaching process. Moreover, the increase of the flow rate in the nondominant channel promotes the rare earth ion exchange reaction in this region. Due to the limitation of its promoting effect, the total amount of leached rare earth ions does not have a linear relationship with the injection intensity, but the growth rate decreases with the increase of the injection intensity. Based on the above analysis, after comprehensive consideration of factors such as leaching period, leached rare earth ion concentration, and total amount of magnesium sulphate, it is concluded that under this model, the injection intensity of 0.5~1.0 mL/min is more economical.

4.2. Influence of Leaching Agent Concentration on Rare Earth Ion Leaching. In order to deeply understand the influence of leaching agent on the leaching of rare earth ions, the NMRI model was used in this study. By controlling the injection

strength of 0.5 mL/min, the seepage-exchange-migration process of saturated leaching under different leaching agents (0.10 mol/L, 0.20 mol/L, 0.25 mol/L, and 0.35 mol/L) was studied.

It is clear from Figure 13 that when the leaching agent concentration is 0.10 mol/L, the peak leaching concentration is 4.8 g/L, and when the injection intensity increases to 0.20 mol/L, 0.25 mol/L, and 0.35 mol/L, the peak leaching concentration is 8.3 g/L, 9.7 g/L, and 12.0 g/L, respectively. It indicates that the peak concentration increases with the increase of leaching agent concentration. Meanwhile, with the increase of leaching agent concentration, the corresponding time of peak concentration is $t = 208$ min, $t = 165$ min, $t = 159$ min, and $t = 142$ min, and the leaching concentration curves are basically in the same position, indicating that the acceleration effect of increasing leaching agent concentration on the whole leaching process is very limited, and the leaching cycle is basically unchanged.

The information given by Figure 14 is about the distribution cloud diagram of leaching rare earth ion concentration in each stage under different leaching agent concentrations. The representative time selected at the corresponding stage in the leaching process in the figure is as described in Section 4.1. On the whole, in the concentration of ore leaching reagents, the migration process of rare earth ions is roughly the same, and the main distribution area of rare earth ions is roughly the same as well. The difference is that the concentration of rare earth ions in the same distribution area in each stage increases with the increase of leaching agent, and the concentration of rare earth ions in the dominant channel and nondominant channel increases accordingly. This is because the increase of leaching agent concentration accelerates the exchange reaction rate, and more rare earth ions are leached per unit time, indicating that the increase of leaching agent concentration can promote the ion exchange reaction in all regions.

Figure 15 demonstrates the total amount of leached rare earth ions and the total amount of magnesium sulphate

under different leaching agent concentrations. As shown in the figure, the total dosage is linearly related to the injection strength, and the total amount of leached rare earth ions increases with the increase of the injection strength. The total amount of 0.20 mol/L increased by 100% compared with 0.10 mol/L, and the total amount of leaching increased by 10.7%. Compared with 0.20 mol/L, the total dosage of 0.25 mol/L increased by 25%, and the total leaching amount increased by 1.6%. Compared with the total dosage of 0.25 mol/L, 0.35 mol/L increased by 40%, and the total leaching amount increased by 1.4%. The increase of the total leaching amount decreased with the increase of leaching agent concentration (i.e., the total dosage of magnesium sulphate). Therefore, the promoting effect of leaching agent concentration on ion-exchange reaction in all regions is limited.

Therefore, the influence of leaching agent concentration on rare earth ion leaching is mainly reflected in when the concentration of leaching agent increases, the ion exchange reaction rate increases accordingly, and more rare earth ions are replaced into the leaching agent per unit time. However, the promoting effect of leaching agent concentration on ion exchange reaction is also limited. Based on the above analysis, after comprehensive consideration of factors such as leaching cycle, leaching rare earth ion concentration, and total magnesium sulphate consumption, it is concluded that under this model, the leaching agent concentration of 0.20~0.25 mol/L is more economical.

5. Conclusion

In this study, the three governing equations of solution seepage, ion exchange, and solute migration of ionic rare earth in situ leaching ore were used to construct a meso-ore body seepage channel model by using NMRI technology, and the reliability of the model was verified by indoor column leaching experiment. On this basis, the effects of injection strength and leaching agent concentration on the leaching of rare earth ions were discussed. The main conclusions are as follows:

- (1) This model can simulate the internal seepage of ionic rare earth ore bodies at mesoscale. The internal seepage of ionic rare earth ore bodies at the mesoscale is more complex, and the flow field distribution is irregular, and there are dominant channels
- (2) At the mesoscale, the ion exchange reaction in the dominant channel is completed preferentially than that in the nondominant channel region, and the migration of rare earth ions in the dominant channel with leaching agent is more affected by convection, and its migration velocity is greater than that in the nondominant channel region
- (3) Increasing the injection strength and leaching agent concentration can promote the exchange and migration of rare earth ions. Based on the limitation of the promotion effect, the injection strength of 0.5~1.0 mL/min and the concentration of

0.20~0.25 mol/L leaching agent are considered to be more economical in practical engineering

Data Availability

The data that support the findings of this study are available from the corresponding author (VS) upon reasonable request.

Conflicts of Interest

The authors declare that there are no conflicts of interest regarding the publication of this paper.

Acknowledgments

This research was supported by the National Natural Science Foundation of China (51964014) and the Education Department of Jiangxi Province (GJJ209414).

References

- [1] D. Wang, Y. Z. Rao, L. Shi, W. Xu, and T. Huang, "Relationship between permeability coefficient and fractal dimension of pore in ionic rare earth magnesium salt leaching ore," *Geofluids*, vol. 2022, Article ID 2794446, 13 pages, 2022.
- [2] L. Liu, Y. Z. Rao, C. S. Tian et al., "Adsorption performance of La (III) and Y (III) on orange peel: impact of experimental variables, isotherms, and kinetics," *Adsorption Science & Technology*, vol. 2021, article 7189639, 12 pages, 2021.
- [3] B. Fan, L. S. Zhao, Z. Y. Feng et al., "Leaching behaviors of calcium and magnesium in ion-adsorption rare earth tailings with magnesium sulfate," *Transactions of Nonferrous Metals Society of China*, vol. 31, no. 1, pp. 288–296, 2021.
- [4] Z. Q. Guo, J. F. Jin, K. Zhao, X. J. Wang, and G. L. Chen, "Status of leaching technology and theory of ion adsorption type rare earth ores," *Chinese Rare Earths*, vol. 2018, no. 1, pp. 132–141, 2018.
- [5] Z. X. Tang, M. N. Li, and D. Yang, "Application and prospect of in-situ leaching mining method in ionic rare earth ores," *Hunan Nonferrous Metals*, vol. 1998, no. 4, p. 3, 1998.
- [6] L. Tao, A. X. Wu, Y. T. Feng et al., "Coupled DEM-LBM simulation of saturated flow velocity characteristics in column leaching," *Minerals Engineering*, vol. 128, pp. 36–44, 2018.
- [7] S. H. Luo, T. Luo, G. S. Wang, J. Liu, S. Hu, and D. Zhu, "Effect of heterogeneity of leaching solution on leaching rate in ionic rare earth ore body," *The Soil*, vol. 50, no. 2, pp. 421–427, 2018.
- [8] L. Shi, Y. Z. Rao, D. Wang, M. D. Zhang, and T. Huang, "A capillary model for predicting saturated hydraulic conductivity of ion-adsorption rare earth ore based on improved Kozeny-Carman equation," *Geofluids*, vol. 2022, Article ID 2947220, 10 pages, 2022.
- [9] R. W. Bartlett, "Simulation of ore heap leaching using deterministic models," *Hydrometallurgy*, vol. 29, no. 1–3, pp. 231–260, 1992.
- [10] A. X. Wu, J. Z. Liu, S. H. Yin, and X. Yong, "The mathematical model of the solute transportation in the heap leaching and the analytic solutions," *Mining and Metallurgical Engineering*, vol. 25, no. 5, pp. 7–10, 2005.
- [11] C. Y. Wu, Y. S. Qiu, and L. M. Wang, "Numerical study on solute transport in leaching process of rare earth by lattice

- Boltzmann method," *The Chinese Journal of Process Engineering*, vol. 14, no. 5, pp. 730–736, 2014.
- [12] G. A. Sheikhzadeh, M. A. Mehrabian, S. H. Mansouri, and A. Sarrafi, "Computational modelling of the unsaturated flow of liquid in heap leaching, using the results of column tests to calibrate the model," *International Journal of Heat and Mass Transfer*, vol. 218, no. 4, pp. 277–289, 2004.
- [13] J. Z. Liu, B. H. Yang, and Y. H. Li, "Coupling mechanism and numerical simulation analysis of leaching process," *Mining and Metallurgical Engineering*, vol. 35, no. 2, pp. 114–116, 2015.
- [14] S. L. Hu, X. J. Cao, G. S. Wang, P. Long, and X. Y. Zhou, "Ion exchange model for leaching process of weathered crust leaching rare earth ore," *Mining and Metallurgical Engineering*, vol. 38, no. 4, pp. 1–5, 2018.
- [15] P. Long, G. S. Wang, J. Tian, S. L. Hu, and S. H. Luo, "Simulation of one-dimensional column leaching of weathered crust elution-deposited rare earth ore," *Transactions of Nonferrous Metals Society of China*, vol. 29, no. 3, pp. 625–633, 2019.
- [16] A. X. Wu, J. Z. Liu, and L. Y. Tang, "Simulation of coupled flowing-reaction-deformation with mass transfer in heap leaching processes," *Applied Mathematics and Mechanics*, vol. 28, no. 3, pp. 327–335, 2007.
- [17] A. X. Wu, S. H. Yin, H. J. Wang, and Y. D. Su, "Mechanism and model of solute transport in heap leaching process," *Journal of Central South University (Science and Technology)*, vol. 37, no. 2, pp. 385–389, 2006.
- [18] C. L. Tan, *Research on seepage-reaction-stress coupling in the leaching process of ion-type rare earth ore*, Jiangxi University of Science and Technology, Ganzhou, 2021.
- [19] D. Ma, H. Y. Duan, and J. X. Zhang, "Solid grain migration on hydraulic properties of fault rocks in underground mining tunnel: radial seepage experiments and verification of permeability prediction," *Tunnelling and Underground Space Technology*, vol. 126, article 104525, p. 14, 2022.
- [20] D. Ma, H. Y. Duan, J. X. Zhang et al., "Numerical simulation of water-silt inrush hazard of fault rock: a three-phase flow model," *Rock Mechanics and Rock Engineering*, vol. 55, no. 8, pp. 5163–5182, 2022.
- [21] Q. Li, D. Ma, Y. D. Zhang, Y. Liu, and Y. J. Ma, "Insights into controlling factors of pore structure and hydraulic properties of broken rock mass in a geothermal reservoir," *Lithosphere*, vol. 2022, article 3887832, 17 pages, 2022.
- [22] B. H. Yang, A. X. Wu, X. X. Miao, and J. Z. Liu, "3D characterization and analysis of pore structure of packed ore particle beds based on computed tomography images," *International Journal of Mining Science and Technology*, vol. 24, no. 3, pp. 833–838, 2014.
- [23] A. X. Wu, B. H. Yang, J. Z. Liu, and J. Zhang, "Analysis of pore evolution law during leaching process of ore bulk based on X-ray CT technology," *The Chinese Journal of Process Engineering*, vol. 7, no. 5, pp. 960–966, 2007.
- [24] X. P. Luo, Y. B. Zhang, H. P. Zhou et al., "Pore structure characterization and seepage analysis of ionic rare earth orebodies based on computed tomography images," *International Journal of Mining Science and Technology*, vol. 32, no. 2, pp. 411–421, 2022.
- [25] C. G. Huang, *Experimental study on the influence of ionic strength and pH of leaching solution on the leaching effect of ionic rare earths*, Jiangxi University of Science and Technology, Ganzhou, 2021.
- [26] C. F. Liu, F. Zhou, X. Y. Wu, J. Feng, and R. A. Chi, "Research status and prospect of leaching, seepage and mass transfer process of weathered crust leaching rare earth ores," *Chinese Rare Earths*, vol. 42, no. 1, pp. 111–121, 2021.
- [27] R. A. Chi and X. M. Liu, "Current situation and prospects of exploitation of weathered crust leach-accumulated rare earth ores," *Journal of the Chinese Society of Rare Earths*, vol. 37, no. 2, pp. 129–140, 2019.
- [28] Y. T. Li, A. B. Tu, Y. F. Zhang, M. Zhang, and R. A. Chi, "Kinetics of leaching rare earth from a weathered crust elution-deposited rare earth ore in South China with mixed ammonium salt," *Industrial Minerals & Processing*, vol. 38, no. 2, pp. 19–24, 2009.
- [29] Z. Chen, Z. Y. Zhang, N. J. Sun, H. Zhang, Z. Liu, and R. A. Chi, "Leaching kinetics of weathered crust elution-deposited rare earth ore with magnesium salt," *Metal Mine*, vol. 2018, no. 8, pp. 84–91, 2018.
- [30] M. Panah and F. Blanchette, "Simulating flow over and through porous media with application to erosion of particulate deposits," *Computers & Fluids*, vol. 166, pp. 9–23, 2018.
- [31] Z. Q. Guo, K. Zhao, J. F. Jin, Z. C. Zhu, and G. Li, "Solute transport mechanism of ion-adsorption type rare earth in-situ leaching mining," *Journal of the Chinese Society of Rare Earths*, vol. 37, no. 1, pp. 121–128, 2019.
- [32] J. Liu and B. H. Brady, "Evaluation of velocity-dependent in situ leaching processes: single-porosity model," *Metallurgical and Materials Transactions*, vol. 29, no. 6, pp. 1227–1234, 1998.
- [33] K. P. Zhou, J. L. Li, Y. J. Xu, and Y. M. Zhang, "Measurement of rock pore structure based on NMR technology," *Journal of Central South University (Science and Technology)*, vol. 43, no. 12, pp. 4796–4800, 2012.
- [34] L. M. Hu, D. T. Lin, P. W. Zhang et al., "Pore structure model for media and application in seepage analysis," *Journal of Taiyuan University of Technology*, vol. 53, no. 3, pp. 360–370, 2022.
- [35] X. W. Chai, G. Q. Li, Z. Y. Zhang, R. Chi, and Z. Chen, "Leaching kinetics of weathered crust elution-deposited rare earth ore with compound ammonium carboxylate," *Minerals*, vol. 10, no. 6, p. 516, 2020.
- [36] J. Tian, X. K. Tang, J. Q. Yin, and X. P. Luo, "Present situation of fundamental theoretical research on leaching process of weathered crust elution-deposited rare earth ore," *Nonferrous Metals Science and Engineering*, vol. 3, no. 4, pp. 48–52, 2012.
- [37] Y. F. Xiao, Y. Y. Chen, Z. Y. Feng et al., "Leaching characteristics of ion-adsorption type rare earths ore with magnesium sulfate," *Transactions of Nonferrous Metals Society of China*, vol. 25, no. 11, pp. 3784–3790, 2015.
- [38] L. H. Gao, R. R. Xing, Y. R. Zhu, and W. Y. Zhao, "Total amount of rare earth in rare earth ferroalloy was determined by EDTA titration," *Metallic Functional Materials*, vol. 29, no. 4, pp. 98–102, 2022.

Research Article

Adsorption of Arsenic, Lead, Cadmium, and Chromium Ions from Aqueous Solution Using a Protonated Chabazite: Preparation, Characterization, and Removal Mechanism

Laura Alejandra Pinedo-Torres,¹ Adrián Bonilla-Petriciolet ²,
María Elena García-Arreola ³, Yenetzi Villagrana-Pacheco,¹ Ana G. Castañeda-Miranda,⁴
and María Selene Berber-Mendoza ³

¹Instituto Politécnico Nacional, Unidad Profesional Interdisciplinaria de Ingeniería Campus Zacatecas, Zacatecas 98160, Mexico

²Instituto Tecnológico de Aguascalientes, Aguascalientes 20256, Mexico

³Centro de Investigación y Estudios de Posgrado, Facultad de Ingeniería, Universidad Autónoma de San Luis Potosí, San Luis Potosí 78210, Mexico

⁴Programa en Ingeniería y Tecnología Aplicada, Laboratorio Nacional CONACYT, SEDEAM, Universidad Autónoma de Zacatecas, Zacatecas 9800, Mexico

Correspondence should be addressed to María Selene Berber-Mendoza; selene.berber@uaslp.mx

Received 21 June 2022; Revised 1 October 2022; Accepted 6 October 2022; Published 25 January 2023

Academic Editor: Juan A. Cecilia

Copyright © 2023 Laura Alejandra Pinedo-Torres et al. This is an open access article distributed under the Creative Commons Attribution License, which permits unrestricted use, distribution, and reproduction in any medium, provided the original work is properly cited.

The adsorption of As(V), Pb(II), Cd(II), and Cr(III) ions from aqueous solutions on natural and modified chabazite was studied. The functionalization of chabazite was performed via a protonation and calcination with the aim of generating Lewis acid sites to improve its anion exchange properties. The surface and physicochemical properties of both adsorbents were studied and compared. The adsorption isotherms of tested heavy metal ions were quantified and modeled to identify the best isotherm equation. Steric parameters for the adsorption of these ions were also calculated with a monolayer statistical physics model. Natural chabazite showed the maximum adsorption capacity for Pb(II), while the modified zeolite improved its As(V) properties in 79%. These results showed that the modified zeolite was able to remove both cations and anions from aqueous solution. The application of this functionalized chabazite can be extended for the removal of other anionic pollutants from water, thus opening the possibility of preparing new adsorbents with tailored properties for water treatment.

1. Introduction

Heavy metal pollution is a relevant environmental problem worldwide due to its significant potential hazard to ecosystems and human health [1]. In particular, heavy metals dissolved in aqueous media are priority in terms of environmental protection because they are more toxic than the atomic form [2]. These soluble heavy metals include arsenic (As), lead (Pb), cadmium (Cd), and chromium (Cr), which are nonbiodegradable and have no physiological function. They have been reported as hazardous pollutants due to their toxicological profile, high solubility, environmental

persistence, and accumulation into the food chain [3, 4]. Therefore, these dissolved heavy metals are classified as potentially toxic elements (PTEs).

According to the International Agency for Research on Cancer (IARC), these PTEs are also considered as carcinogenic [5] where their main exposure routes are the inhalation of contaminated air, skin absorption, and ingestion of polluted food or water [6–9]. Consequently, it is necessary to develop cost-effective and sustainable methods and materials to reduce the concentrations of these toxic species from polluted water and industrial effluents [10]. Nowadays, the adsorption is a simple and reliable technique for water and

wastewater treatment where its success mainly depends on the preparation of an effective adsorbent [11]. The most used adsorbents are activated carbons, zeolites, silica gel, activated alumina, and biochar [12–15].

Natural zeolites offer several advantages for water treatment. They are low-cost minerals present in various parts of the world, have pore sizes $< 20 \text{ \AA}$, and, consequently, are capable of adsorbing or rejecting molecules, which make them suitable as molecular sieves [16]. Zeolites also adjust the pH of the media, and their application usually does not generate additional environmental pollution [17].

In terms of chemical composition, zeolites are aluminosilicates with a structure consisting of a tetrahedral arrangement of silicon (Si^{4+}) and aluminum (Al^{3+}) cations with four oxygen anions (O^{2-}) at the vertices. This composition generates a three-dimensional framework containing SiO_4 and AlO_4 tetrahedral building blocks with permanent negative charges [18], which are balanced by monovalent or divalent counterions (e.g., alkaline or alkaline earth metals) that have the capability of acting as adsorption sites [19]. The adsorption process is controlled by the zeolite properties like ion exchange capacity and selectivity [20].

Chabazite is a zeolite used worldwide due its high surface area and physicochemical properties as ion exchanger [21–23]. Its framework has units of six double rings (D6R) interconnected through 4 rings, forming a 3-dimensional channel system that presents large ellipsoidal cavities with apertures consisting of 8 rings with a diameter of 3.8 \AA in the cation-free condition [24, 25].

Natural chabazite can adsorb cationic species due to its negative charge. Different studies have reported the removal of different cations using this zeolite, thus obtaining a maximum adsorption capacity of 175 mg/g of Pb(II) [26]; 120 mg/g of Cd(II) [27]; 4.5 mg/g of Ni(II) [28]; $4.2\text{--}8.9 \text{ mg/g}$ of Cu(II) , Co(II) , Zn(II) , and Mg(II) [29]; and $30\text{--}45 \text{ mg/g}$ of NH_4^+ [30, 31]. It has been established that its adsorption properties to remove cationic species in water treatment follow the next selectivity: $\text{Cs}^+ > \text{NH}_4^+ > \text{K}^+ > \text{Pb}^{2+} > \text{Na}^+ > \text{Ba}^{2+} > \text{Cd}^{2+} > \text{Sr}^{2+} > \text{Cu}^{2+} > \text{Zn}^{2+}$ [32].

On the other hand, the chabazite can be tailored via different processes to improve its adsorption performance for the removal of organic molecules and negatively charged species. For example, this material can be synthesized from urban wastes like cement and used to adsorb 129 mg/g of methylene blue [33]. This zeolite with the incorporation of copper was also able to adsorb NO_x where the results showed that Cu-CHA catalysts prepared with a conventional wet ion exchange method outperformed the NO_x conversion obtained with samples prepared via chemical vapor deposition and solid-state ion exchange [34]. A chemical treatment based on hexadecyltrimethylammonium bromide (HDTMA-Br) helped to change the external surface of this zeolite from negative to positive, thus being able to adsorb 26 mg/g of $\text{Cr}_2\text{O}_7^{2-}$ [35], 6.9 mg/g of AsO_4^{3-} , and 3.3 mg/g of PO_4^{3-} [36].

A straightforward modification process to improve the properties of zeolites relies on the decationation using different interchange ions like NH_4Cl , NaCl , or $\text{Cu}(\text{NO}_3)_2$ with the subsequent calcination at $\geq 450^\circ\text{C}$. This approach has been used to modify the surface properties of zeolites with

the aim of removing anions in aqueous solution. Some examples are the removal of fluoride using clinoptilolite with a maximum adsorption capacity of 12.3 mg/g [37], the gasoline desulfurization employing 5A and 13X zeolites with a removal of 16.7 mg/g [38], and the nitrite removal from wastewater [39]. The superficial zeolite modification using NH_4Cl and a subsequent thermal treatment have been utilized to tailor synthetic chabazites for the thermal degradation of high-density polyethylene to low molecular mass hydrocarbons [40] and the adsorption of ethane (41 mg/g) and propane (81 mg/g) [41]. This material had been also employed as a catalyst in the methanol to olefins reaction (forming polyaromatic coke species) [42]. However, this approach has not been applied to improve the chabazite properties for the adsorption of anionic pollutants from water. Also, its impact on the cation adsorption properties of natural zeolites has not been analyzed in detail.

The aim of this study was to develop an effective and low-cost protocol to tailor the surface properties of the chabazite for the improvement of the adsorption of anionic species. This method was based on the decationation with NH_4Cl and protonation and subsequent calcination of natural chabazite. Results showed that this functionalization route was successful to generate Lewis acid sites (LAS) on this zeolite, thus increasing its anion adsorption properties. The performance of natural and modified zeolites was tested on the removal of As(V) , Pb(II) , Cd(II) , and Cr(III) ions. The adsorption isotherms were correlated and analyzed with the Langmuir, Freundlich, Sips, Liu, and statistical physics models. The adsorption properties of these adsorbents were compared and correlated with their ion exchange capacity and chemical composition. The mechanisms of chabazite modification and adsorption of tested ions were analyzed. Finally, this study showed that the modified chabazite can be used to remove both anions and cations of water pollutants, thus being a promising approach for low-cost water depollution.

2. Methodology

2.1. Preparation of Modified Chabazite. Natural zeolite used in this study was obtained from a mineral deposit from the state of Sonora, Mexico. The natural chabazite (labelled as CH-N) was sieved to obtain a particle size $< 125 \mu\text{m}$, and these zeolite particles were utilized in the surface modification process, which was implemented according to a method adapted from Ghasemian et al. [43]. This method involved the following steps: (a) *Homogenization*: 50 g of zeolite was mixed with 500 mL of 2 N NaCl solution, stirred at 500 rpm and room temperature for 24 h [44]. Zeolite was washed several times with deionized water and dried at 100°C for 24 h . The sample obtained from the homogenization process was represented by the label “Z-Na”. (b) *Decationation*: the dry zeolite was treated with ammonium chloride because the exchange of Na^+ is better for zeolites with NH_4^+ [45]. 12.5 g of homogenized chabazite was mixed with 250 mL of 1 N NH_4Cl at room temperature for 24 h under constant stirring. The final zeolite was washed with hot deionized water and dried at 100°C . The sample

obtained from the decationation process was labelled as “Z-NH₄⁺”. (c) *Thermal treatment*: decationated zeolite was calcined at 500°C for 3 h using a heating rate of 5°C/min. Then, the sample was washed with deionized water and dried at 100°C for 24 h. Finally, this modified zeolite (labelled as “CH-MS”) was characterized and used for the adsorption experiments. Flow diagram of this process is included as Supplementary Information.

2.2. Chemical Characterization of Zeolite. The identification of the crystalline phases present in the zeolite samples was carried out by X-ray diffraction (XRD) analysis. XRD patterns were recorded with a diffractometer Siemens D5000 at room temperature. Samples were scanned within 2θ angular range of 5–50° with a step size of 0.020° for 10 s.

The textural parameters were determined by the Brunauer-Emmett-Teller method (BET) using a surface area and pore size analyzer (Quantachrome model nova 3200e). The samples were introduced into glass cell and degassed at 200°C for 10 h. N₂ physisorption was measured at -196.15°C.

The surface morphology of the zeolite samples was examined by using a scanning electron microscope (SEM) JEOL, model JSM-6610LV equipped with a microanalysis system model DX-4 energy dispersed spectroscopy (EDS). CH-N and CH-MS samples were placed on a fine coat brand carbon coater for this analysis.

Infrared spectra were obtained using Fourier transform infrared spectrophotometer (Thermo Scientific Nicolet iS10 FTIR). First, CH-N and CH-MS samples were dried at 70°C for 24 h to remove the moisture. Spectra of the samples were recorded in the region of 4000–600 cm⁻¹. FTIR analysis was also performed to determine the acid centers of tested adsorbents via the adsorption of pyridine. Samples of CH-N and CH-MS were subjected to vacuum and then exposed to pyridine atmosphere for 24 h. FTIR spectra of pyridine-loaded samples were recorded and analyzed.

The thermogravimetric analysis (TGA) was done using a PerkinElmer equipment (model Pyris Diamond TGA/DTG) calibrated with indium and gold samples from 25 to 660°C and 1063°C, respectively. 0.2 mg of zeolite sample was analyzed in the temperature range of 25–700°C with increments of 10°C/min.

The procedure established by Corbin et al. [46] was utilized for the determination of chemical composition of CH-N and CH-MS. The samples were sieved to obtain a particle size of 0.18 mm, and then, 0.1 g was mixed with 0.2 g of LiBO₂ and 0.4 g of Li₂B₄O₇. The mixtures were placed in a graphite crucible with a drop of LiBr (25% w/w) and calcined for 30 min at 900°C in a muffle. The melted mixture was dissolved in 75 mL of HNO₃ (10% w/w), filtered and made up to 200 mL. The concentrations of dissolved metals were quantified with a Thermo Scientific Inductively Coupled Plasma Optical Emission Spectrometry (ICP-OES). Multielement solutions containing Fe, Mn, Ca, Mg, K, Si, Na, Al, Sr, Pb, Sn, Hg, Cd, Zn, As, Ni, Cr, Mo, and Ba were used to prepare the calibration curve where high purity standard solutions (1000 mg/L) of each metal and deionized water were employed for this purpose.

2.3. Surface Properties of Zeolites. The pH of the point of zero charge (PZ) of the zeolites was determined preparing solutions with pH between 2.27 and 6.75 (with a constant ionic strength of 0.01 M) via the mixing of certain volumes of 0.01 M NaOH, HNO₃, and NaNO₃ with 0.005 g of the samples at 25°C under constant stirring of 30 rpm for 5 days in an orbital shaker. Finally, the zeta potential of the zeolite particles was obtained using the zetameter (Zetasizer, Malvern model Nano series).

Cation exchange capacity (CEC) was obtained using a methodology reported by Ming & Dixon [47] where 1 g of CH-N and CH-MS samples was saturated with Na⁺ ions (using 50 mL of 1 N C₂H₃NaO₂ for 24 h) and washed, and the exchange of Na⁺ ions for NH₄⁺ ions was done using 50 mL of 1 N C₂H₇NO₂ at room temperature for 24 h. Na⁺ ion concentration was measured with an ICP-OES, and the CEC (meEq/g) was determined with the following equation:

$$\text{CIC} \left(\frac{\text{mEq}}{100\text{g}} \right) = \frac{[\text{Na}^+] V \cdot 100}{m \text{ MW}}, \quad (1)$$

where [Na +] is the Na⁺ concentration (mg/L), *V* is the volume (L), *m* is the mass of chabazite (g), and MW is the Na⁺ molecular weight (mg/mEq).

2.4. Adsorption Studies Using Zeolites. Adsorption studies were conducted with both zeolites CH-N and CH-MS in glass Erlenmeyer flasks containing 0.05 g of the adsorbent and 0.040 L of the pollutant solution. These studies were performed at pH 4 where the solution pH was adjusted by adding HNO₃ or NaOH and mixing with a glass stirrer. Note that this solution pH was selected to avoid the precipitation of Cd(II) and Pb(II) ions as hydroxides (i.e., Cd(OH)₂ and Pb(OH)₂ at pH > 5 and 6, respectively) [48, 49] and to prevent the zeolite dealumination [31, 50]. Other studies have also reported that a maximum adsorption capacity of Pb(II), Cd(II), and Cr(III) ions can be obtained with different adsorbents at pH 4 [48, 51, 52]. Initial concentrations of 1–59, 20–500, 10–112, and 5–93 mg/L for As(V), Pb(II), Cd(II), and Cr(III), respectively, were used in the adsorption experiments. These solutions were prepared with J.T. Baker standard solution of 1000 mg/L of each metal and deionized water. The suspensions (adsorbent+pollutant solution) were stirring at 50 rpm and 25 ± 0.5 °C in a thermoregulated orbital shaker (IKA model KS 4000) for 5 days. This time was enough to reach the equilibrium according to preliminary adsorption experiments at tested conditions. The quantification of metal concentrations was done using ICP-OES. The calibration curve for the quantification of these metals was obtained with solutions that were prepared using a high purity standard solution (1000 mg/L) of each adsorbate and deionized water. The removal of ions per unit mass of adsorbent (i.e., adsorption capacity) was expressed as *q_e* (mEq/g) and calculated with the mass balance given by the following equation:

$$q_e = \frac{V}{m} (C_o - C_e), \quad (2)$$

where C_o and C_e are the initial and equilibrium concentrations (mEq/L) of tested ion in the aqueous solution. Finally, the speciation of tested heavy metals was obtained by means of Hydra-Medusa speciation software at pH 0–14 and 25°C.

2.5. Isotherm Modeling. The experimental equilibrium data were modeled to analyze As(V), Pb(II), Cd(II), and Cr(III) adsorption and to explain the interactions of these heavy metal ions with CH-N and CH-MS samples. The best isotherm model for the removal of these pollutants was also identified. Therefore, four different isotherm models were tested using a nonlinear regression procedure. They corresponded to two-parameter (Langmuir and Freundlich) and three-parameter (Liu and Sips) isotherm models.

Langmuir is a monolayer adsorption model where the adsorbent saturation occurs assuming active sites with the same energy. This model considers that there is only one interaction corresponding to one active site per specie, and this isotherm is presented in equation (3) [53]. Freundlich is a multilayer adsorption model where the energy of active sites is not homogeneous, and this model is commonly applied to analyze heterogeneous systems. This isotherm model is presented in equation (4) [54]. Alternatively, Sips model can be reduced to the Freundlich and Langmuir models at low and high concentrations, respectively, and it presents the advantages of these two models since it is a combination of them. This isotherm model is given by equation (5) [55]. The Liu isotherm is a Langmuir-Freundlich type isotherm that has the advantage over the Sips model because its exponent has no restrictions in terms of its maximum value where it is >0 . This isotherm is presented in equation (6) [56]. In summary, the corresponding equations of these isotherm models are given by

$$q_e = \frac{q_L K_L C_e}{1 + K_L C_e}, \quad (3)$$

$$q_e = K_F C_e^{1/n_F}, \quad (4)$$

$$q_e = \frac{q_S K_S C_e^{n_S}}{1 + K_S C_e^{n_S}}, \quad (5)$$

$$q_e = \frac{q_{LF} (K_{LF} C_e)^{n_{LF}}}{1 + (K_{LF} C_e)^{n_{LF}}}, \quad (6)$$

where q_L , q_S , and q_{LF} are the maximum adsorption capacities of the Langmuir, Sips, and Liu equations (mEq/g); K_L , K_S , K_{LF} , and K_F are the constants of the Langmuir, Sips, Liu (L/mEq), and Freundlich (mEq/g)(L/mEq) $^{1/n_F}$ isotherms; and n_F , n_S , and n_{LF} are the dimensionless exponents (parameters related to the adsorption intensity that represents the relative distribution of the heterogeneity and the energy of the adsorption sites) of the Freundlich, Sips, and Liu equations, respectively.

A nonlinear least squares method based on an optimization algorithm was used to obtain the isotherm model

parameters. The Solver tool of Microsoft Excel software was used to minimize the sum of the square error (ERRSQ) [57]:

$$(\text{ERRSQ}): \sum_{i=1}^N (q_{t,\text{meas}} - q_{t,\text{calc}})_i^2, \quad (7)$$

where $q_{t,\text{meas}}$ is the adsorption capacity from the experiment (mEq/g), $q_{t,\text{calc}}$ is the adsorption capacity calculated with the isotherm model (mEq/g), and N is number of experimental points.

To compare and assess the performance of the isotherm models, three statistical metrics were calculated: determination coefficient (R^2), the average percentage deviation (%D), and chi-square (X^2) [57–59]. These metrics are given by the following equations:

$$R^2 = \frac{\sum_{i=1}^N (q_{t,\text{calc}} - \overline{q_{t,\text{meas}}})^2}{\sum_{i=1}^N (q_{t,\text{calc}} - \overline{q_{t,\text{meas}}})^2 + \sum_{i=1}^N (q_{t,\text{calc}} - q_{t,\text{meas}})^2}, \quad (8)$$

$$\%D = \left[\frac{1}{N} \sum_{i=1}^N \left| \frac{q_{t,\text{meas}} - q_{t,\text{calc}}}{q_{t,\text{meas}}} \right| \right] \cdot 100\%, \quad (9)$$

$$X^2 = \sum_{i=1}^N \frac{(q_{t,\text{meas}} - q_{t,\text{calc}})^2}{q_{t,\text{calc}}}. \quad (10)$$

A monolayer adsorption model [60] was also utilized in the isotherm data correlation with the aim of analyzing the main steric parameters involved in the removal of these ions. This model was defined by

$$q_e = \frac{n_{\text{ads}} N_{\text{zeolite}}}{1 + (C_{\text{med}}/C_e)^{n_{\text{ads}}}}, \quad (11)$$

where n_{ads} is the number of ions adsorbed per functional group of zeolite, N_{zeolite} (mEq/g) is the quantity of zeolite functional groups involved in the adsorption of these pollutants, and C_{med} (mEq/L) is the adsorbate concentration at the half saturation condition, respectively.

3. Results and Discussion

3.1. Surface Chemistry Characterization of CH-N and CH-MS. Figure 1 shows the X-ray diffraction patterns of both zeolites used in this study. For CH-N, it was possible to confirm the presence of the expected chabazite structure characterized by its main peaks at 9.39° (1 0 1), 20.43° (-2 1 0), and 30.37° (-3 1 1) according to the JCPDS card 34-137 [61]. This result also agreed with the calculated XRD patterns reported for this zeolite [62]. X-ray diffraction pattern of CH-MS indicated that the crystalline structure remained after the modification process, thus preserving all the intensity peaks similar to CH-N. These findings could suggest that the modification took place only on the external surface, which agreed with the previous studies [63, 64]. Additionally, it was possible to observe an increase in the intensity of the peaks in the modified zeolite. This observation agreed with other studies (e.g., [37]) where an increment of the

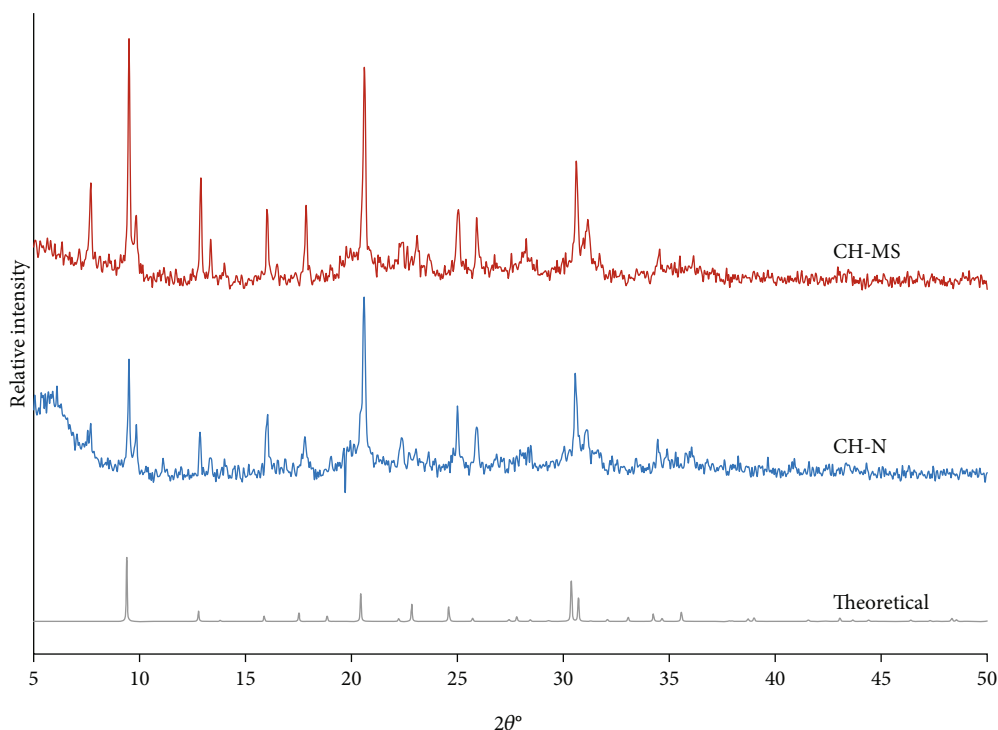


FIGURE 1: X-ray diffraction patterns of CH-N and CH-MS. Label “Theoretical” corresponds to the calculated pattern from International Zeolite Association, which was used as a reference pattern.

TABLE 1: Textural properties of CH-N and CH-MS samples.

Zeolite	Surface area (m ² /g)	Pore diameter (nm)	Pore volume (cm ³ /g)
CH-N	324.2	2.94	0.198
CH-MS	325.9	3.04	0.216

intensity after a similar modification to a natural zeolite was also identified.

The textural properties of CH-N and CH-MS are given in Table 1. According to these results, CH-N surface area (324.4 m²/g) was higher than some values reported in the literature for natural zeolites such as 2.7 m²/g for perlite consisting of zeolites X (FAU type), P (GIS type), and phillipsite [65]; 20.3, 42, and 258 m²/g for clinoptilolite [66–68]; 68 and 305 m²/g for modernite [68, 69]; and 202 m²/g for a natural chabazite from Mexico [31]. However, this value was lower than 1100 m²/g of a natural chabazite supplied by Minerals Research-Clarkson, NY, USA [70].

Regarding the texture properties of CH-N and CH-MS, the differences between their surface areas and pore diameters were 0.52% and 3.35%, which were not significant because they were within the error interval of the equipment used in sample analysis. Nevertheless, the difference in pore volume corresponded to an increment of 8.33% that was statistically significant. It is convenient to remark that the behavior of the texture properties of different zeolites submitted to the similar surface modification treatment has been associated to the changes on their micropore structure. Both increments and reductions in these textural parameters have been reported. For instance, Saucedo-Delgado et al.

[37] reported an increment of 90.6 and 22% in the surface area and pore volume of clinoptilolite. On the other hand, Albayati and Kalash [71] proved that the functionalization (via the reaction between the silylating agent and the silanol groups) of mesoporous silica MCM-41 incremented the surface area from 28.7 to 300 m²/g, while the calcined MCM-41 showed the highest surface area (i.e., 1000 m²/g). In the contrary case, a decrease of 15.5 and 23% in pore diameter and surface area of modernite was reported by Mori et al. [72], while Atiyah et al. [73] obtained surface areas of 845 and 45 m²/g for the mesoporous silica SBA-15 and its functionalized form NH₂/SBA-15, respectively, thus indicating a significant decrement of this textural parameter.

SEM micrographs of chabazites showed the typical rhombohedral crystals that were consistent with the previous studies [31, 74, 75]. By comparing these micrographs, it was possible to observe that CH-N (Figure 2(a)) presented a well-defined structure, while CH-MS (Figure 2(b)) showed partially formed rhombohedral structures. This could be explained because during the modification process, the minerals were washed several times, which could fragment the zeolite agglomerates. Chemical analysis of CH-N crystals by SEM-EDX (Figure 2(a)) indicated the presence of the characteristic elements of zeolites: Si, Al, O, Mg, Ca, K, and Na. On the other hand, EDX results showed that the exchangeable cations (Na⁺ and Ca⁺) of CH-MS (Figure 2(b)) were expelled from the framework, where this effect agreed with the result obtained by Barrer et al. [76] and Ghasemian et al. [43]. This behavior can be explained by the fact that, during the homogenization phase carried out for chabazite, Na⁺ displaced the majority of Ca²⁺. Then, the sodium ions were exchanged with

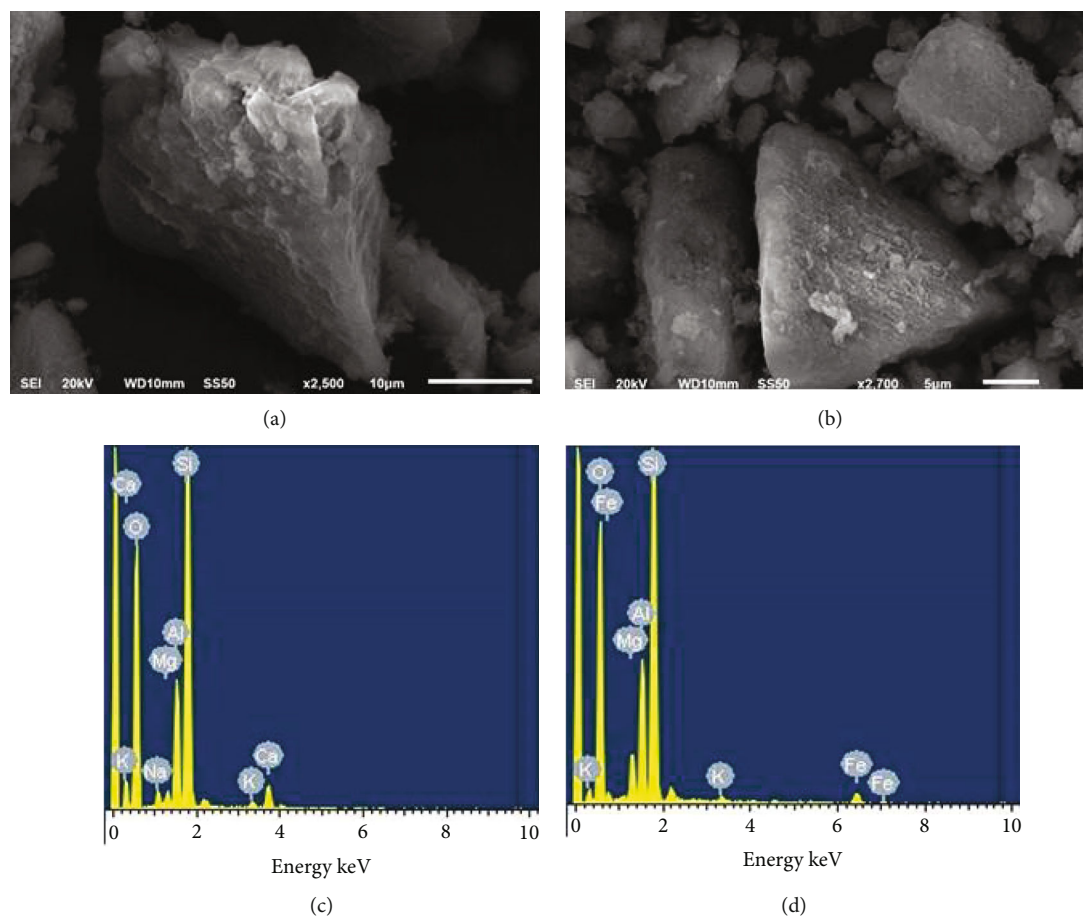


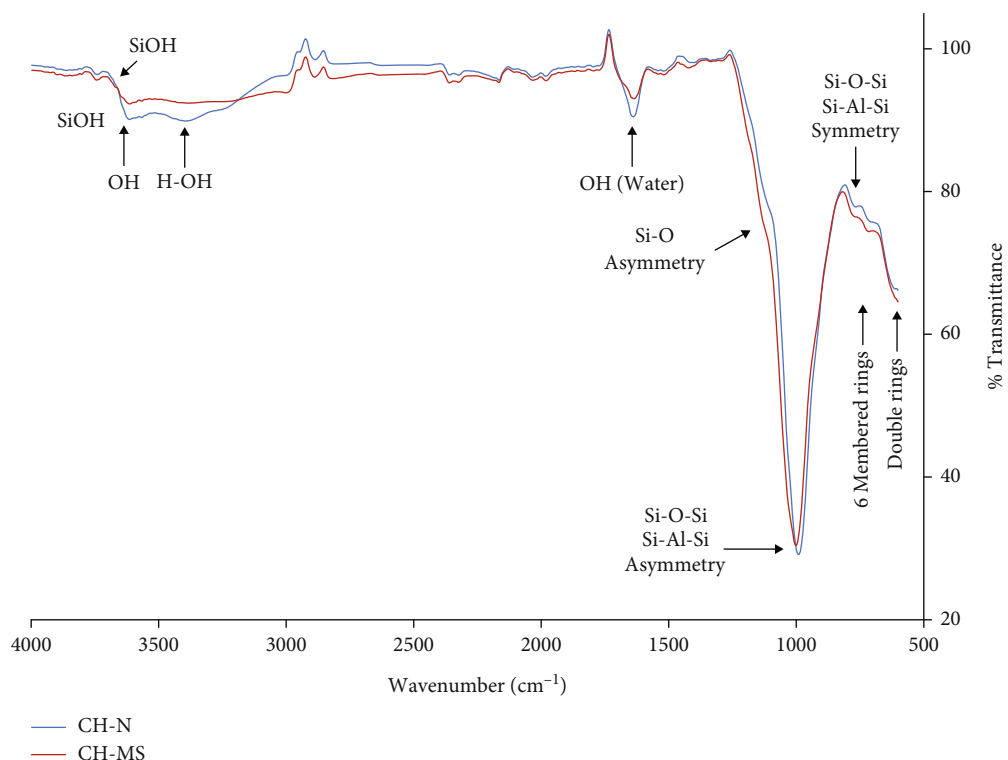
FIGURE 2: (a, b) SEM micrographs and (c, d) SEM/EDX elemental microanalysis for CH-N and CH-MS samples.

the ammonium ions when the zeolite was treated with NH_4Cl because the thermodynamic affinities for the exchange reactions in chabazite followed the next sequence: $\text{NH}_4^+ > \text{Na}^+ > \text{Ca}^{2+}$, which were given by the standard free energies of exchange [76].

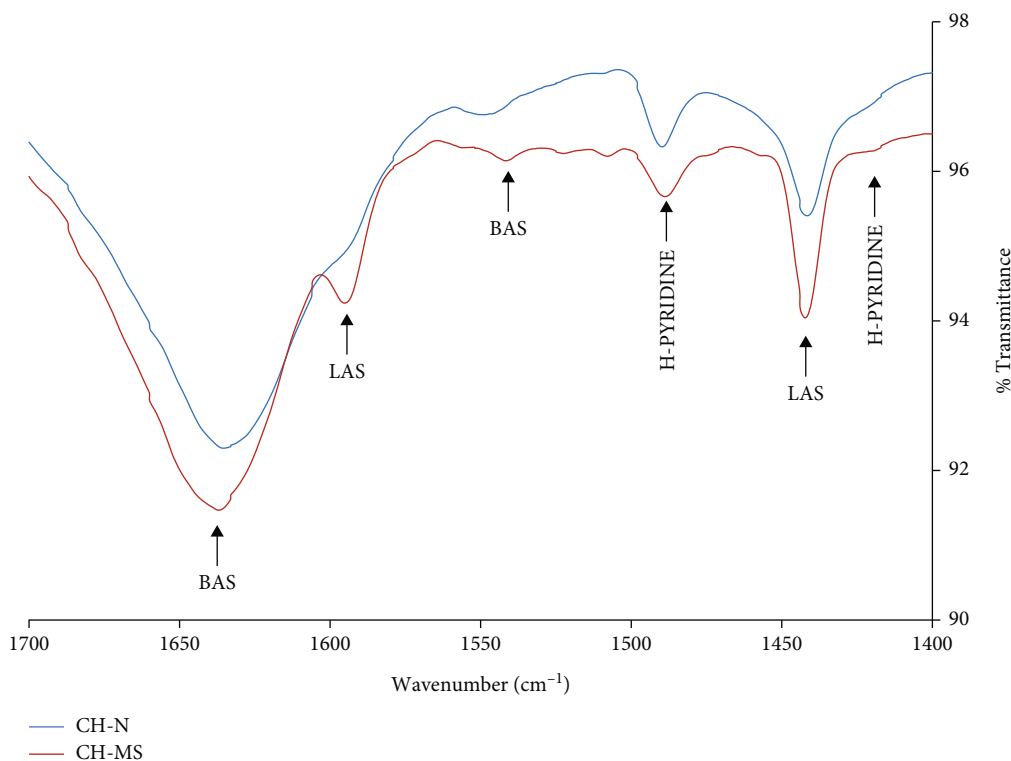
Figure 3(a) presents the FTIR spectra of CH-N and CH-MS at $4000\text{--}600\text{ cm}^{-1}$. At $750\text{--}650$ and $1250\text{--}950\text{ cm}^{-1}$, these spectra displayed the internal vibrations of TO_4 tetrahedron (T=Si and Al) named as OH stretching (indicated by the four-membered ring structure) and asymmetry stretching. The absorption band between 570 and 635 cm^{-1} indicated 6-membered rings. The external vibrations of the tetrahedron (i.e., T–O double ring, symmetry and asymmetry stretching) appeared at $650\text{--}500$, $820\text{--}750$, and $1150\text{--}1050\text{ cm}^{-1}$, respectively [77]. The absorption bands observed at 1640 , 3600 , and 3380 cm^{-1} were characteristic to the water bending vibration, isolated, and H-bonded hydroxyl groups, respectively [78]. These three bands for CH-N sample showed higher intensities than those observed for CH-MS, thus indicating that CH-N had a higher water content that was lost in the modified zeolite upon calcination. Another major difference was that CH-MS sample showed an absorption band at 3640 cm^{-1} corresponding to the hydroxyl group formed during the modification process [79]. Both types of vicinal hydroxyl groups were observed via the bands at 3640 and $3700\text{--}3740\text{ cm}^{-1}$ that was associated to the silanol nests [80].

It was possible to observe that CH-MS did not present the characteristic bands of NH_4^+ form (i.e., the Lewis bond NH_3 at 1630 cm^{-1} , while NH_4^+ is characterized by bands between 1400 and 1500 cm^{-1} and NH stretching frequencies at 3800 cm^{-1}) because they disappeared due to the heating at 290°C [81].

Figure 3(b) reports the FTIR spectra of CH-N and CH-MS samples loaded with pyridine at $1400\text{--}1700\text{ cm}^{-1}$. The absorption bands at 1640 and 1545 cm^{-1} have been attributed to the pyridine adsorption and were characteristic of the Brønsted acid sites (BAS). The bands located at ~ 1430 and 1490 cm^{-1} corresponded to hydrogen-bonded pyridine (H-pyridine), while the bands identified at 1590 and 1450 cm^{-1} have been attributed to coordinately bound pyridine, thus being an indicator of Lewis acidity [82–84]. The intensity of the absorption bands of LAS (1450 and 1590 cm^{-1}) and BAS (1640 cm^{-1}) in the spectrum of pyridine-loaded CH-MS were higher than those of the other zeolite sample. This was due to the modification where BAS and LAS sites were formed. Emeis [85] reported similar results where pyridine adsorption was studied for natural and calcined modernite at 550°C for 2 h. Other studies of Ward [86] showed an infrared spectrum of pyridine adsorbed on a rare earth Y zeolite calcined at 430 and 680°C , while Wu and Weitz [87] reported the results for a ZSM-5 zeolite modified (protonated with nitrate salt and calcined at 500°C).



(a)



(b)

FIGURE 3: FTIR spectra of CH-N and CH-MS samples (a) without and (b) with loaded pyridine.

Figures 4(a) and 4(b) show the thermogravimetric (TGA) and differential (DTG) analysis curves for CH-N and CH-MS samples. TGA results indicated that the weight

of both samples decreased considerably with the increase of temperature up to ~600°C. Then, there was a slow and progressive weight reduction. The weight loss was 16.55% for

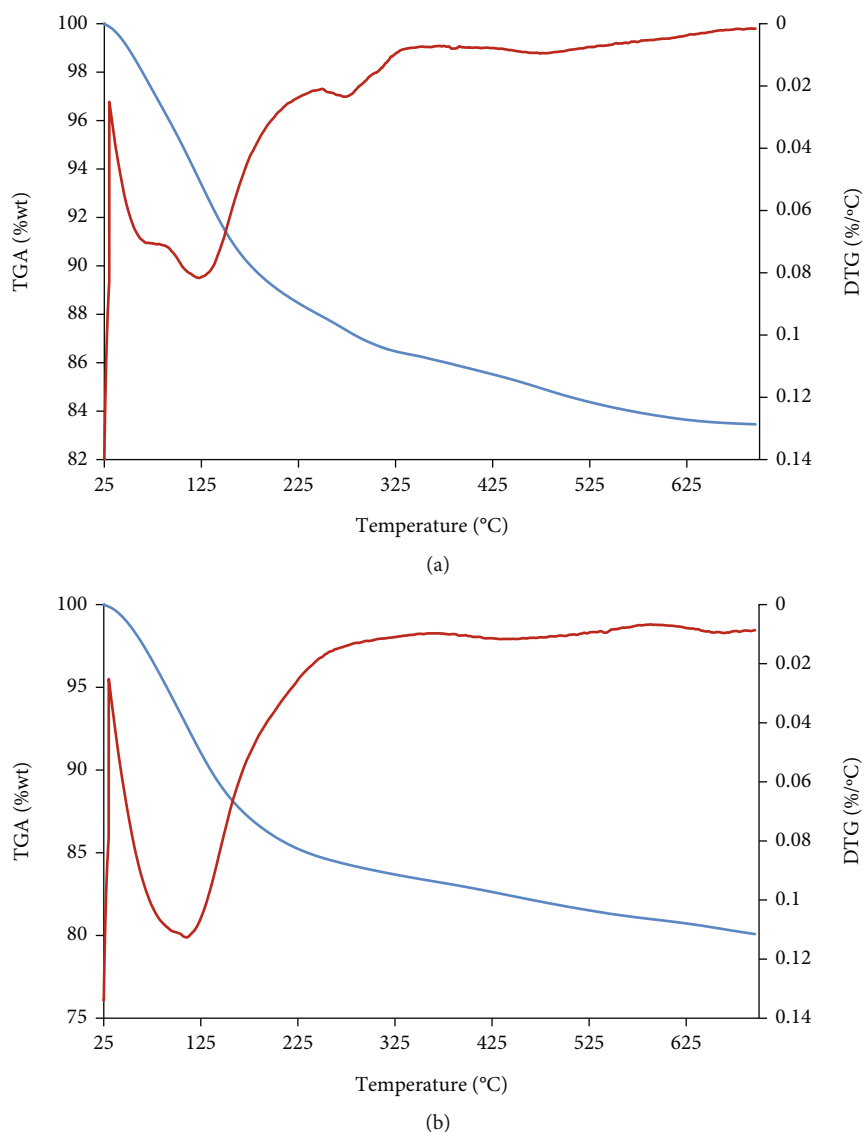


FIGURE 4: Results of TGA and DTG for the zeolite samples: (a) CH-N and (b) CH-MS.

TABLE 2: Chemical composition of the chabazite and its modified form.

Zeolite	wt%								Si/Al ratio
	Fe	Ca	Mg	K	Si	Na	Al	Others	
CH-N	3.76	5.95	4.31	3.12	60.11	3.65	18.22	0.88	3.3
CH-MS	3.75	0.00	3.98	3.00	64.65	0.00	24.10	0.52	2.8

CH-N and 19.92% for CH-MS. DTG curve showed the water loss from CH-N sample in two steps. The first step at 81°C was attributed to the humidity loss of the zeolite, while the second step at 118°C corresponded to the loss of structural water from the zeolite. The decomposition of calcium carbonate was associated to the peak at 270°C, which was consistent with the study of Stakebake [88] that indicated that this phenomenon could occur before 310°C.

For the case of CH-MS sample, the loss of water adsorbed on the zeolite (humidity) occurred at 109.98°C. It is convenient to highlight that there was no other peak cor-

responding to the loss of structural water for this sample, which occurred during the zeolite calcination at 500°C. It should be noted that other studies have reported the decomposition of NH_4Cl at 310°C [89]. Based on the DTG curve of CH-MS, it was concluded that this compound was not present in the modified zeolite. This finding could be due to the previous release of NH_3 in the calcination stage of the modification process, which was consistent with the FTIR results that confirmed the absence of this compound.

The chemical composition of CH-N and CH-MS is presented in Table 2. It can be observed that the weight

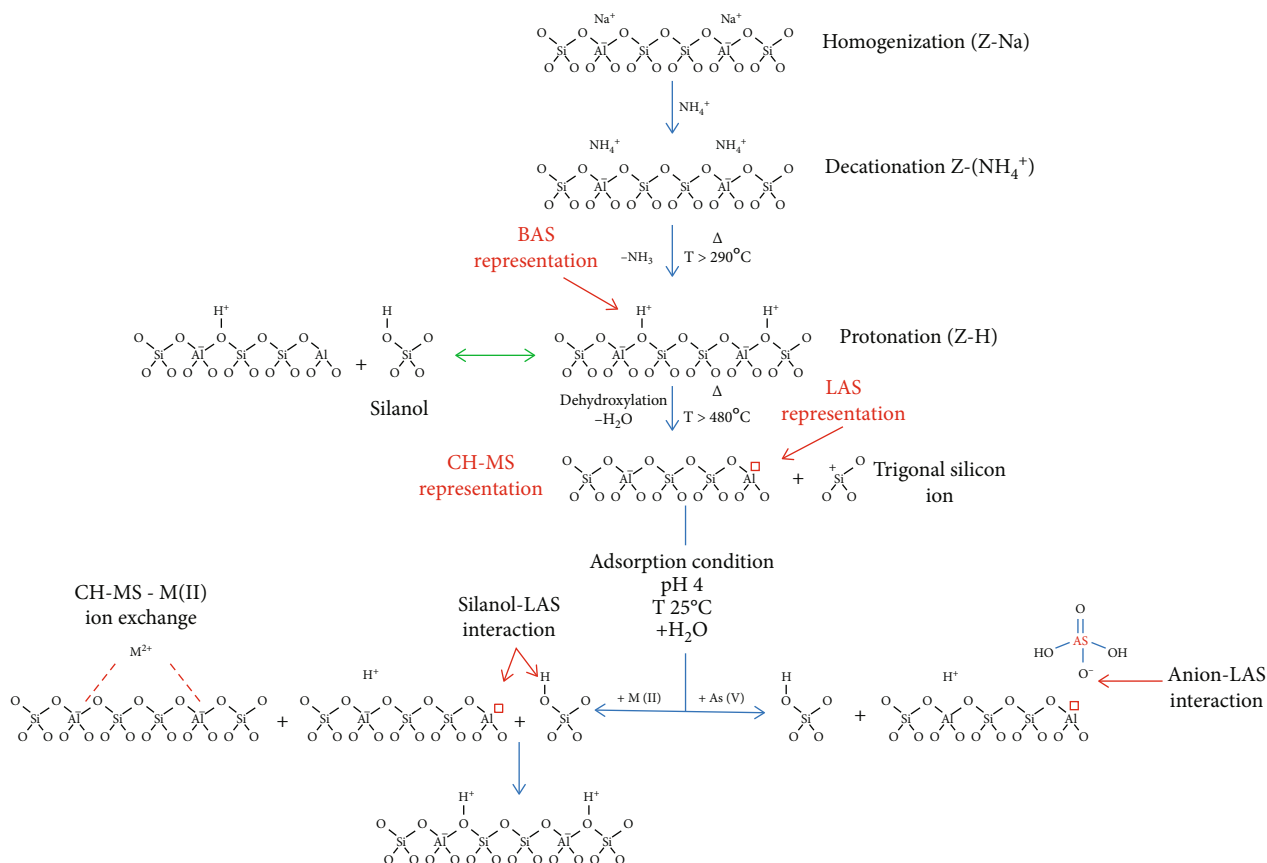


FIGURE 5: Illustrative 1D scheme of the stages of CH-N modification process where the formation of silanol, Brønsted acid sites (BAS), Lewis acid sites (LAS), and trigonal silicon ions is shown. The interaction of the CH-MS with divalent cations M(II) and anions like As(V). This figure was adapted from Uytterhoeven et al. [81] and Juzsakova et al. [45].

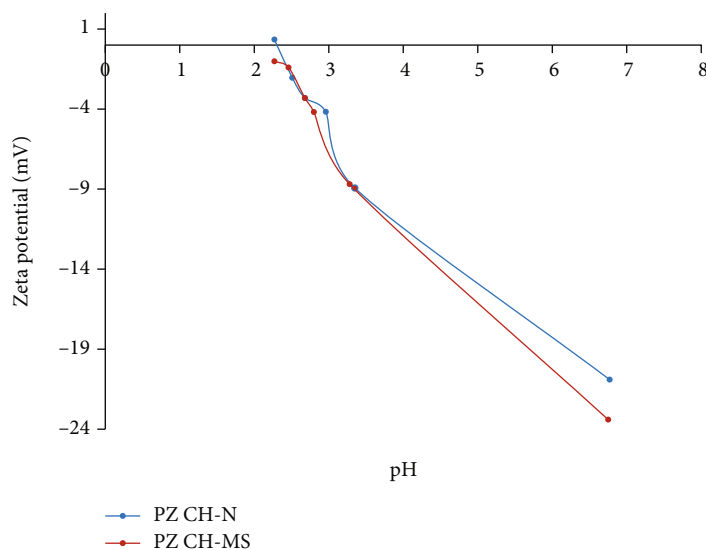


FIGURE 6: Zeta potential versus pH for CH-N and CH-MS samples.

fractions of exchangeable cations in CH-N decreased in the following order: Ca^{2+} , Mg^{2+} , Na^+ , and K^+ . On the other hand, the chemical composition confirmed the

EDX results of CH-MS (Figure 2(d)) where the exchangeable cations Na^+ and Ca^+ were expelled out from the framework.

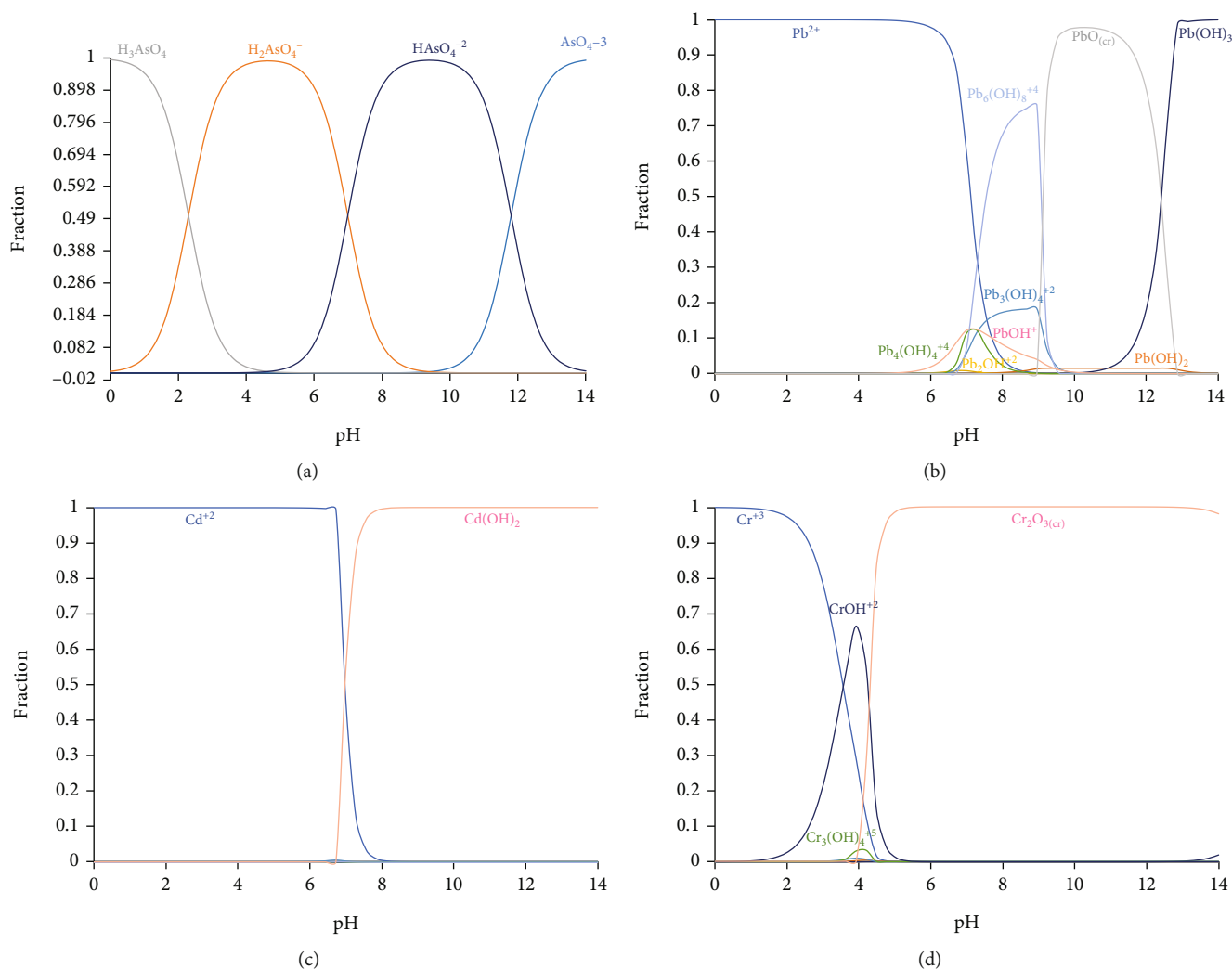


FIGURE 7: (a) Arsenic, (b) lead, (c) cadmium, and (d) chromium speciation as a function of solution pH in aqueous solution.

Table 2 shows Si/Al ratio of 3.3 for the CH-N sample that matched with the value of 3.2 found by Leyva-Ramos et al. [31], which was also between the range of 1.43-4.18, 3.2-3.8, and 2-4 obtained by Gottardi & Galli [90], Zamzow et al. [91], and Metwally & Attallah [92], respectively. Si/Al ratio of CH-MS sample was 2.8, which was lower than the value found for CH-N sample. The decrease in the Si/Al ratio of these samples coincided with the results reported by Panayotova [93] where a natural zeolite from Kardjali was modified by heating at 373°C and using 2 mol/dm³ of NaOH solution.

The significant decrease in the Si/Al ratio between CH-N and CH-MS samples was caused by the superficial modification of the zeolite, whose steps are schematized in Figure 5. After homogenization (Z-Na) and decationization (Z-NH₄⁺), NH₃ was removed by a thermal treatment at ≥290°C. This sample was named protonated form of zeolite (H-Z). This process generated BAS and was accompanied by the formation of free protons that attacked the tetrahedral aluminum lattice, thus causing the formal bond between aluminum and oxygen broken, and the corresponding formation of hydroxyl groups as silanol (Si-

OH). This process was reversible since the interaction of silanols with aluminum formed the protonated zeolite and *vice versa* [79, 94]. Note that Iler [95] established that the condensation of silanol groups was higher in the presence of excess salts at pH 4-8. Therefore, the pH 7 and the application of 2 M NH₄Cl solution in the chabazite modification process provided the optimal conditions for the formation of silanol groups. They can be eliminated with the consecutive washing of material during the modification process. Therefore, it was reflected as an increase in the proportion of Al in the zeolite framework and a change in the Si/Al ratio.

3.2. Surface Properties of Zeolites. Figure 6 shows the results of the pH of PZ for both zeolites. It was concluded that the CH-N and CH-MS surfaces were negatively charged at tested adsorption conditions. Similar findings have been reported in the literature for clinoptilolite and other zeolites treated with NH₄Cl and calcination process [86, 96].

The negative charge for CH-MS was an expected result, which can be explained considering that the modification process was carried out at high temperature (i.e., 500°C).

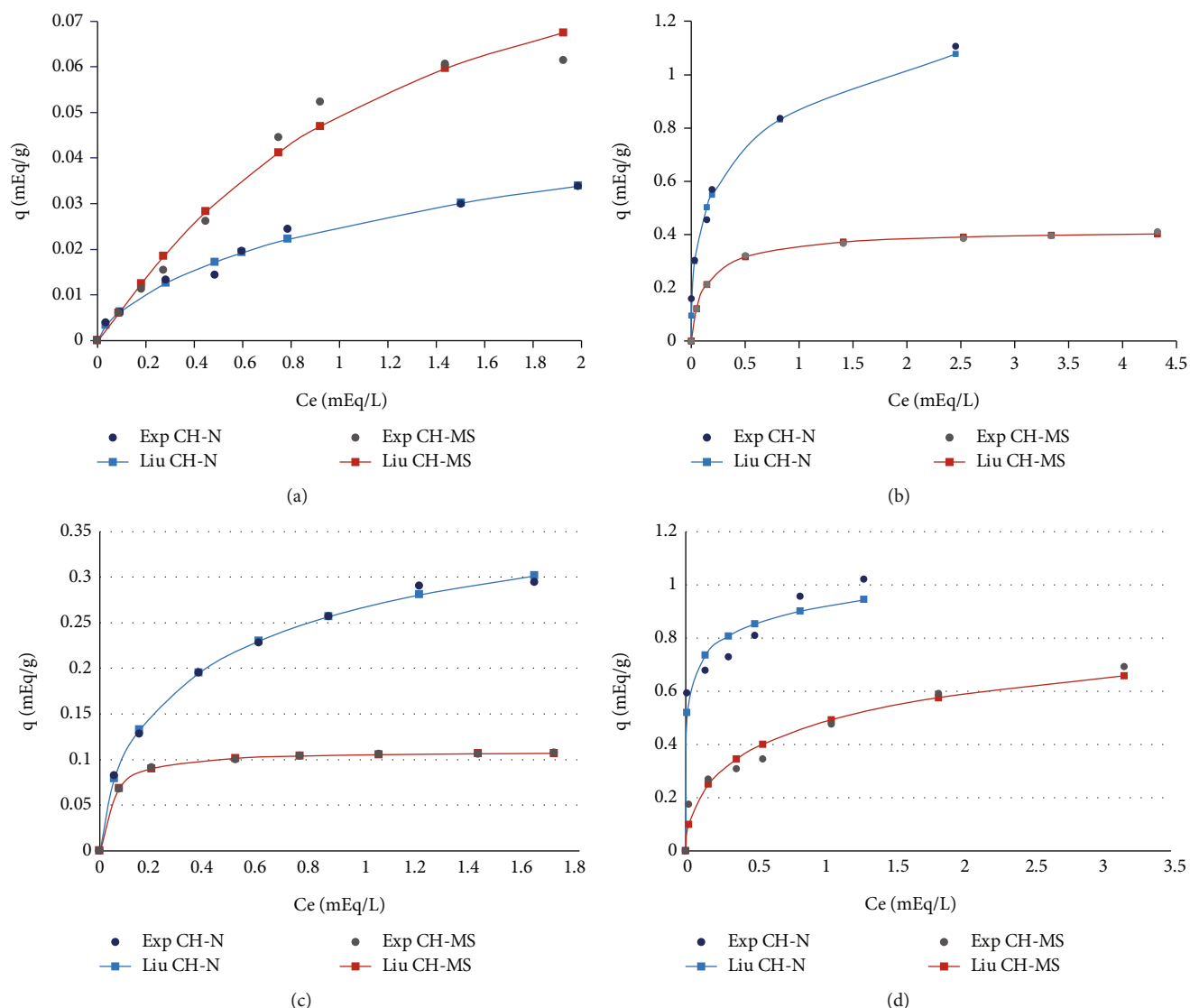


FIGURE 8: Isotherms for the adsorption of (a) As(V), (b) Pb(II), (c) Cd(II), and (d) Cr(III) on CH-N and CH-MS zeolites at pH 4 and their correlation with Liu model.

Ward [86] indicated that if the calcination process occurred at $\geq 480^\circ\text{C}$, BAS became LAS because the bonds of H-Z were very weak and easily removable (i.e., this process is called dehydroxylation or water loss). This phenomenon caused the formation of trigonal silicon ions and accessible trigonal aluminum [81] that can accept a pair of electrons, and therefore, it can adsorb anions. Figure 5 illustrates the formation of LAS where the negative charge of CH-MS is clearly outlined.

The surface interactions involved in the adsorption of anions on this modified zeolite can be explained as follows: CH-MS zeolite showed a negatively surface charge in the aqueous solutions that caused the attraction of H^+ ions from the solution, while the HO^- ions were attracted by the trigonal silicon ions, thus forming silanols. The adsorbate anions in the solution can interact via electrostatic attraction with the LAS [97] since they are the active sites in the zeolites [98]. This mechanism agreed with that

proposed by Uytterhoeven [81] for water, Lewis acid centers, and molecules with lone pairs of electrons such as NH_3 . On the other hand, the cations can be attracted by the negative charges of the CH-MS during the adsorption process. Note that the divalent cations could interact with more than a single site of the zeolite during the interface phenomenon [99]. It could be expected that the adsorption of cations on CH-MS was associated to an ion exchange. As explained, the interaction of silanol groups with acid centers of a zeolite generates a protonated zeolite. But this process was not reversible at 25°C because the zeolite was not reheated and the dehydroxylation did not occur.

CEC of CH-N and CH-MS was 1.68 and 0.53 mEq/g. These values showed a significant decrease of 68.45% of this property with respect to a CH-N sample. This result was because the ion exchange behavior of zeolites depends on the internal properties like chemical composition, framework

TABLE 3: Results of isotherm fitting using the Langmuir, Freundlich, Sips, and Liu equations for the adsorption of As(V), Pb(II), Cd(II), and Cr(III) on CH-N and CH-MS zeolites.

Ion	Zeolite	Model parameters*				R^2	%D	X^2	Model
		q_{model} (mg/g)	q_{model} (mEq/g)	K_{model}	n_{model}				
As(V)	CH-N			0.024	1.954	0.984	8.473	1.01×10^{-3}	Freundlich
		1.324	0.047	1.219		0.979	14.509	3.32×10^{-3}	Langmuir
		2.226	0.079	0.330	0.701	0.973	6.539	8.43×10^{-4}	Liu
		2.226	0.079	0.460	0.685	0.982	6.166	8.15×10^{-4}	Sips
As(V)	CH-MS			0.045	1.600	0.934	24.330	8.01×10^{-3}	Freundlich
		3.015	0.107	0.825		0.973	14.473	3.44×10^{-3}	Langmuir
		2.902	0.103	0.924	1.105	0.988	8.683	2.22×10^{-4}	Liu
		2.902	0.103	0.933	1.162	0.974	7.82	2.20×10^{-4}	Sips
Pb(II)	CH-N			0.851	3.008	0.992	11.949	0.056	Freundlich
		114.989	1.109	5.537		0.956	27.56	2.591	Langmuir
		235.960	2.277	0.307	0.0407	0.992	9.656	0.048	Liu
		232.429	2.244	0.635	0.410	0.989	9.778	0.049	Sips
Pb(II)	CH-MS			0.314	4.885	0.962	10.525	0.026	Freundlich
		42.279	0.408	7.576		0.995	2.219	1.27×10^{-3}	Langmuir
		43.656	0.421	5.365	0.864	0.997	1.136	4.36×10^{-4}	Liu
		43.656	0.421	6.976	0.864	0.998	1.135	4.36×10^{-4}	Sips
Cd(II)	CH-N			0.273	2.582	0.997	4.194	4.98×10^{-3}	Freundlich
		18.716	0.333	4.250		0.983	5.967	8.38×10^{-3}	Langmuir
		25.236	0.449	1.796	0.660	0.997	2.048	7.95×10^{-4}	Liu
		25.236	0.449	1.472	0.6604	0.995	2.047	7.95×10^{-4}	Sips
Cd(II)	CH-MS			0.104	8.139	0.882	4.564	1.63×10^{-3}	Freundlich
		6.126	0.109	23.016		0.995	0.716	5.29×10^{-5}	Langmuir
		6.126	0.109	22.54	1.051	0.996	0.632	4.76×10^{-5}	Liu
		6.126	0.109	26.10	1.047	0.996	0.631	4.77×10^{-5}	Sips
Cr(III)	CH-N			0.876	9.718	0.838	7.111	0.035	Freundlich
		19.680	0.855	190.38		0.441	12.302	0.090	Langmuir
		45.773	1.990	0.451	0.194	0.962	8.401	0.034	Liu
		44.719	1.944	0.889	0.195	0.809	8.397	0.035	Sips
Cr(III)	CH-MS			0.455	2.457	0.986	11.058	0.078	Freundlich
		17.259	0.750	2.049		0.914	20.917	0.671	Langmuir
		25.495	1.108	0.629	0.544	0.966	12.965	0.075	Liu
		24.434	1.062	0.842	0.559	0.941	13.310	0.0811	Sips

* q_{model} (q_L , q_{LF} , and q_S) is the maximum adsorption capacities of the Langmuir, Liu, and Sips equations. K_{model} (K_L , K_{LF} , K_S , and K_F) is the constant of the Langmuir, Liu, Sips (L/mEq), and Freundlich (mEq/g) (L/mEq)^{1/n_F} equations. n_{model} (n_{LF} , n_S , and n_F) is the dimensionless exponent of the Liu, Sips, and Freundlich equations.

structure, and charge density [100], besides the external properties like size, shape, charge, and concentration of ions [101]. As established by Jacobs and Leuven [102], the average reaction rate per site will be related with the chemical composition, thus generating an increment almost linearly of the frequency of silanol groups with a decrement of Si/Al ratio of the framework [103], which was coupled with the

formation of LAS containing trigonal silicon ions. This explained that the change in the Si/Al ratio of CH-MS sample caused a decrement of the number of active sites because of the formation of the silanol groups and the trigonal silicon ions. This pointed out that the silanol groups were not active centers such these cannot serve as adsorption sites [80]. Although LAS were active sites, they can attract

TABLE 4: Maximum adsorption capacities for the removal of As(V), Pb(II), Cd(II), and Cr(III) using different materials.

Ion	Adsorbent	q_{\max} (mg/g)	Isotherm model	Reference
As(V)	Clinoptilolite and modernite natural and modified with Fe	9.2×10^{-3} 0.062	Freundlich	Baskan & Pala [126] Velazquez-Peña et al. [128] Elizalde-González et al. [127]
	Chabazite modified with Fe and Zr	0.068	Freundlich	Velazquez-Peña et al. [128]
	Hydrated cement	1.92	Langmuir	Bibi et al. [129]
	Bone char	2.45	Langmuir	Alkurdi et al. [118]
	Activated carbon from oat hulls	3.09	Langmuir	Chuang et al. [134]
	Graphene oxide modified by iron-manganese binary oxide (FeMnOx/RGO)	11.5	Langmuir	Zhu et al. [135]
	Magnetite nanoparticle coated zeolite	19.39	Freundlich	Liu et al. [130]
	Carbon nanotubes coated with zirconium oxide	124.6		Liu et al. [131]
Pb(II)	Clinoptilolite	14.25-22.60	Freundlich	Kragović et al. [136] Mozgawa & Bajda [137]
	Cocoa pod husk and watermelon rind	20.10-98.06	Rendlich-Peterson	Liu et al. [138]
	Clinoptilolite natural and its NH_4^+ and Na^+ forms	120.2-142.8	Langmuir	Leyva-Ramos et al. [139]
	Chabazite	175	—	Kesraoui-Ouki et al. [26]
	Synthesized zeolite from lithium leach residue via hydrothermal method	487.80	Langmuir	Lv et al. [140]
	Carbon foam	491.0	Sips	Lee et al. [141]
	Synthesized zeolite from bagasse fly ash	625.0	Langmuir	Jangkorn et al. [142]
Cd(II)	Erionite and clinoptilolite	2.54-4.63	Sips	Hernández-Montoya et al. [120]
	Peanut husk and corn stalk industrial waste	7.68-12.63	Langmuir	Rozumová et al. [143] Zheng et al. [107]
	Carbon nanotubes oxidized with HNO_3	11.1	—	Li et al. [144]
	Chabazite	13.26	Freundlich	Panuccio et al. [145]
	Synthesized coal fly ash zeolite	26.25	Langmuir	Javadian et al. [146]
	Fly ash treated with NaOH	48.31	Langmuir	Buema et al. [147]
	Activated carbon derived from bagasse	49.07	Freundlich	Mohan & Singh [148]
	Grape pomace activated carbon	75.61	Langmuir	Sardella et al. [149]
Cr(III)	Fibrous activated carbons	3.52	Langmuir	Aggarwal et al. [150]
	Granulated activated carbon	13.31	Langmuir	Aggarwal et al. [150]
	MnO_2 -modified magnetic biochar derived from palm kernel cake	19.92	Langmuir	Maneechakr & Mongkollertlop [151]
	Natural clinoptilolite	21.20	—	Mozgawa & Bajda [137]
Cr(VI)	Multiwalled carbon nanotube	13.2	—	Kumar et al. [152]
	Magnetic zeolite/chitosan composites	25.67	Langmuir	Liu et al. [153]
	Porous Fe_3O_4 hollow microspheres/graphene oxide composite	32.33	Langmuir	Liu et al. [154]
	Functionalized multiwalled carbon nanotube with $\text{H}_2\text{SO}_4/\text{HNO}_3$ solution	85.83	—	Kumar et al. [152]
	Ionic liquid impregnated exfoliated graphene oxide	285.71	Temkin	Kumar et al. [155]

anions. As a result of the interaction of BAS and LAS, the zeolites present a superacidity [104] since both sites act synergistically potentiating the acidity [105]. As established by Barthomeuf [106], an acidic environment in zeolites affects the number of interchange sites, their location, density, and efficiency.

The value of CEC of CH-N was within the range of values reported for natural chabazites from Japan, Christmas

Arizona, and a zeolite provided by American Colloid Co., which showed values of 1.87, 1.95, and between 0.08 and 2.61 mEq/g, respectively [20, 70, 107]. The decrease in CEC agreed with Ferrer [108] that used a clinoptilolite submitted to the same surface treatment and subsequent calcination at 500°C. These authors reported CEC values of 11.76 and 6.33 mEq/g for natural and modified materials, respectively. This treatment generated a change of 46% in this property,

which was lower than that obtained with chabazite. In this direction, Moreno-Tost et al. [109] use Cu-exchanged morденite and clinoptilolite with the subsequent calcination at 550°C. These authors found a change in the CEC of 86% with respect to a natural clinoptilolite and 68% for natural modernite.

3.3. Analysis and Modeling of Adsorption Isotherms. Figure 7 shows the speciation diagrams of the different metals in the aqueous solution as a function of solution pH. The predominant ionic forms for tested adsorbates at pH 4 were Pb^{2+} and Cd^{2+} for Pb(II) and Cd(II), while H_2AsO_4^- and $(\text{CrOH})^{2+}$ were the dissolved species for As(V) and Cr(III) during the adsorption experiments. Therefore, the experimental isotherms of the adsorption of As(V), Pb(II), Cd(II), and Cr(III) on CH-N and CH-MS samples are reported in Figure 8, and the fitting results using the models of Langmuir, Freundlich, Sips, and Liu are shown in Table 3.

The adsorption capacity on CH-N and CH-MS followed the next sequence: $\text{Pb(II)} > \text{Cr(III)} > \text{Cd(II)} > \text{As(V)}$, which agreed with the results obtained by Caputo and Pepe [32]. Experimental data showed that As(V) adsorption capacity was 0.034 and 0.061 mEq/g for CH-N and CH-MS, respectively, thus indicating that the zeolite functionalization improved in 79% its removal performance for this ion. Pb(II) adsorption capacities of CH-N and CH-MS were 1.10 and 0.41 mEq/g, respectively, while the Cd(II) and Cr(III) adsorption capacities of these zeolites were 0.29 and 0.11 mEq/g and 1.02 and 0.69 mEq/g, respectively. These reductions (33–67%) in the adsorption capacities of these cations were directly related to CEC decreased 68.45% due to the zeolite modification and the generation of BAS and LAS on the adsorbent surface. These adsorption capacities were not attributed to the surface area and pore diameter of tested zeolites, since both samples showed similar textural parameters.

The maximum exchange degree of Pb(II) on CH-N was an expected result, which can be explained according to the Eisenman-Sherry theory [110, 111]. Particularly, Pb(II) ion has a lower value of hydration enthalpy and a higher value of equilibrium constant (which is generally utilized as a measure of the cation exchange selectivity) in chabazite than those reported for the other two cations.

The chabazite has four classes of cation sites, named C1, C2, C3, and C4, where C1 sites are located in the center of the small cage (D6R) and they can be accessed through 6-membered ring, thus representing 20% of the overall CEC of this zeolite. C2-C4 sites are located in the large ellipsoidal cavities, and they can be accessed via 8-membered ring [112, 113]. According to the Double Selectivity Model (DSM) proposed by Pepe et al. [114], these types of sites are named group “I” and group “II.” It could be expected that large ions like $(\text{CrOH})^{2+}$ could not access to C1, while Pb(II) and Cd(II) can interact with these sites [115, 116]. So, the reduction of CEC in the modified zeolite was mainly associated to the loss of active sites in group I and group II, which were involved in the generation of Lewis acid centers. This phenomenon affected the final adsorption properties of the modified zeolite for cationic species. It is also important to mention that the significant reduction (up to 67%) of Pb(II)

TABLE 5: Calculated steric parameters for the adsorption of Cd(II), Pb(II), Cr(III), and As(V) on CH-N and CH-MS zeolites.

Adsorbate	Zeolite	n_{ads}	Interpretation
As(V)	CH-N	0.69	Multianchorage
	CH-MS	1.68	Multi-ionic
Pb(II)	CH-N	0.41	Multianchorage
	CH-MS	0.88	Multianchorage
Cd(II)	CH-N	0.68	Multianchorage
	CH-MS	0.89	Multianchorage
Cr(III)	CH-N	0.76	Multianchorage
	CH-MS	0.39	Multianchorage

adsorption properties of CH-MS was associated to Na^+ ions that were expelled out from the zeolite framework during the modification process. Previous studies have reported that Na^+ can be completely exchangeable by Pb^{2+} , thus explaining the adsorption capacities of natural chabazite [116, 117].

Table 3 indicates that the q_L values obtained with the Langmuir model were lower than q_{LF} and q_S values calculated by the Liu and Sips models. These findings agreed with other studies reported for the adsorption of As(V), Pb(II), Cd(II), and Cr(III) ([118–121]). On the other hand, the n_F values of the Freundlich model ranged from 1.60 to 9.71 for the adsorption of tested ions, thus indicating a favorable removal process [54, 122]. The Langmuir constant K_L can be associated to the bonding energy between the zeolite and ions [123], and this parameter ranged from 1.21 to 190.38 (L/mEq), thus suggesting a good adsorption affinity between the zeolite and tested ions.

In terms of modeling, X^2 has been widely used to analyze the error distributions of data sets and to identify the most suitable equation for the calculation of adsorption isotherms [58, 124, 125]. Therefore, X^2 was employed to characterize the performance of tested isotherm models for both zeolites. This statistical metric indicated that the three-parameter isotherm models (i.e., Liu and Sips) showed the better fit of experimental data, thus presenting X^2 values lower than those obtained for the two-parameter isotherm models of Langmuir and Freundlich. Herein, it is convenient to recall that the use of the Sips equation is usually restricted to the fact that its dimensionless heterogeneity factor n_S must be between 0 and 1 [55, 122]. Results reported in Table 3 indicated that the calculated n_S values for As(V), Pb(II), Cd(II), and Cr(III) adsorption on chabazite modified did not comply with this restriction. Therefore, the Liu isotherm ($X^2 = 4.76 \times 10^{-5} - 0.075$) was selected as the best model to correlate these experimental adsorption isotherms (see Figure 8).

For illustration, Table 4 shows a comparison of the maximum adsorption capacity for the removal of different ions using several adsorbents. Overall, the results confirmed that the protonated chabazite was more effective for the removal of As(V) than other zeolites reported in the literature like clinoptilolite, modernite, and chabazite [126–128], as well as other waste materials like hydrated cement and bone char [118, 129]. However, the adsorption capacities of CH-N and CH-

MS were lower than the values reported for advanced materials like graphene oxide and carbon nanotubes [130, 131].

This study confirmed that the functionalization of zeolites to remove anions is a promising approach to improve the performance of these materials in water treatment. For example, the clinoptilolite modified with NH_4Cl plus its subsequent thermal treatment at 500°C increased its fluoride adsorption capacity by 2.33-fold with respect to the natural zeolite [37]. Other study showed that a natural zeolite rock treated at 800°C increased its anion adsorption capacity with respect to the uncalcined zeolite [39]. Another example is the thermal treatment (at ≥ 500) of different mesoporous silica sieves like MCM-41, MCM-48, SBA-15, and Co/MCM-41 to improve the removal of sulfur from diesel [132, 133].

With respect to the performance of natural chabazite for the removal of cations, its Pb(II) adsorption properties are competitive and can outperform the results obtained using watermelon rind and other zeolites like natural and modified clinoptilolite and chabazite [26, 138, 139]. Even after its functionalization, the protonated chabazite showed a Pb(II) adsorption capacity higher than those of cocoa pod husk and natural clinoptilolite [136–138]. However, this modified zeolite can be outperformed by, for example, carbon foam and zeolites synthesized by complex processes from lithium leach residue and bagasse fly ash ([135, 141, 142]).

For the case of Cd(II) adsorption, CH-MS can outperform erionite and clinoptilolite [120], while the adsorption properties of CH-N were better than those reported for carbon nanotubes and biomass wastes like peanut husk and corn stalk [143, 144, 156]. However, fly ash treated with NaOH outperformed this zeolite [147]. Also, the adsorption capacities of natural and modified chabazite for Cd(II) removal were significantly lower than those obtained with activated carbon [148, 149].

For the case of Cr(III) and Cr(VI) adsorption, CH-MS outperformed different activated carbons, magnetic zeolite/chitosan composites, multiwalled carbon nanotube, and natural clinoptilolite [137, 150–152]. On the other hand, the adsorption properties of CH-N were higher than those reported for magnetic zeolite/chitosan composites and porous Fe_3O_4 hollow microspheres/graphene oxide composite [153, 154]. However, its removal performance was lower than the reported for functionalized multiwalled carbon nanotube with $\text{H}_2\text{SO}_4/\text{HNO}_3$ solution and ionic liquid impregnated exfoliated graphene oxide [152, 155].

In summary, these results indicated that CH-MS could be considered a promising adsorbent for the removal of anions and cations from polluted water. This adsorbent could be applied in the depollution of other matrices like soil or mining waste, which also contain both types of ionic pollutants.

With respect to the interpretation of the adsorption mechanism, the steric parameters related to the adsorption of Cd(II), Pb(II), Cr(III), and As(V) on CH-N and CH-MS are reported in Table 5. In particular, n_{ads} ranged from 0.41 to 0.76 for the adsorption of cations and $n_{\text{ads}} = 0.69$ for the anion adsorption on CH-N. These results suggested that the removal of Cd(II), Pb(II), Cr(III), and As(V) can be classified as multi-anchorage where two adsorption sites from this zeolite could participate during the removal process [60]. For the case of

modified chabazite, the calculated n_{ads} values ranged from 0.39 to 0.89 for the adsorption of heavy metal cations, while n_{ads} was 1.68 for the adsorption of As(V) anions (see Table 5). These results indicated that the Pb(II), Cd(II), and Cr(III) adsorption prevailed as multi-anchorage, and a multi-ionic adsorption occurred for the As(V) removal with CH-MS sample. The amount of adsorption sites of CH-N that were involved in the adsorption of these pollutants was 0.12–1.19 mEq/g, while the adsorption sites of CH-MS that participated in the adsorption were 0.04–0.48 mEq/g. These calculations were consistent with characterization results and CEC values that indicated the loss of some adsorption sites due to the zeolite modification protocol. As illustrated in Figure 5, the framework vacancy generated during the surface modification of chabazite allowed that its adsorption sites could interact with more than one As(V) anion, thus causing a multi-ionic adsorption of this pollutant.

4. Conclusions

This study has proved that a low-cost and straightforward protocol can be used to modify and tailor the surface properties of chabazite for the adsorption of anionic pollutants from aqueous solutions. This zeolite surface modification allowed to generate Lewis acid centers that could act as electron pair acceptors, thus increasing up to 79% the As(V) adsorption properties. However, the adsorption of Pb(II), Cd(II), and Cr(III) cations of this modified chabazite decreased 33–67%. This reduction of the cation adsorption properties was generated by a decrement of its cation exchange capacity and the loss of Na^+ exchange sites from zeolite surface. Statistical physics calculations indicated that the adsorption of all these ions on natural chabazite was a multi-anchorage phenomenon, while the As(V) adsorption on modified chabazite was a multi-ionic process. A reduction of the number of zeolite adsorption sites after surface functionalization was confirmed that affected the removal of cationic species. Natural chabazite can be considered an outstanding adsorbent for the Pb(II) removal with adsorption capacities higher than 100 mg/g. The application of this modified chabazite can be extended for the removal of other relevant anion pollutants from water. Further studies should be also focused on its application to depollute other real-life matrices (e.g., soil and wastewater) containing both anionic and cationic toxic compounds.

Data Availability

The data used to support the findings of this study are included within the article.

Conflicts of Interest

The authors declare that they have no conflicts of interest.

Acknowledgments

This work was funded by the Consejo Nacional de Ciencia y Tecnología (National Council of Science and Technology),

CONACYT, Mexico, through Grant PN 2015-01-1616 (attention to national problems financed by CONACYT).

Supplementary Materials

The supplementary information describes through a flow diagram the steps of chabazite modification. (*Supplementary Materials*)

References

- [1] J. G. Paithankar, S. Saini, S. Dwivedi, A. Sharma, and D. K. Chowdhuri, "Heavy metal associated health hazards: an interplay of oxidative stress and signal transduction," *Chemosphere*, vol. 262, article 128350, 2021.
- [2] S. Tasharrofi, Z. Rouzitalab, D. M. Maklavany et al., "Adsorption of cadmium using modified zeolite-supported nanoscale zero-valent iron composites as a reactive material for PRBs," *Science of the Total Environment*, vol. 736, article 139570, 2020.
- [3] S. Afroze and T. K. Sen, "A review on heavy metal ions and dye adsorption from water by agricultural solid waste adsorbents," *Water, Air, & Soil Pollution*, vol. 229, no. 7, pp. 1–50, 2018.
- [4] E. Gutiérrez-Segura, M. Solache-Ríos, A. Colín-Cruz, and C. Fall, "Comparison of cadmium adsorption by inorganic adsorbents in column systems," *Water, Air, & Soil Pollution*, vol. 225, no. 6, pp. 1–13, 2014.
- [5] International Agency for Research on Cancer, "Beryllium, cadmium, mercury, and exposures in the glass," in *Apresentado Em: IARC Working Group on the Evaluation of Carcinogenic Risks to Humans*, pp. 1–415, IARC monographs on the evaluation of carcinogenic risks to humans, Lyon, 1993.
- [6] M. Chen, Z. Xie, Y. Yang, B. Gao, and J. Wang, "Effects of calcium on arsenate adsorption and arsenate/iron bioreduction of ferrihydrite in stimulated groundwater," *International Journal of Environmental Research and Public Health*, vol. 19, no. 6, p. 3465, 2022.
- [7] J. Y. Chung, S. D. Yu, and Y. S. Hong, "Environmental source of arsenic exposure," *Journal of Preventive Medicine and Public Health*, vol. 47, no. 5, pp. 253–257, 2014.
- [8] G. Genchi, M. S. Sinicropi, G. Lauria, A. Carocci, and A. Catalano, "The effects of cadmium toxicity," *International Journal of Environmental Research and Public Health*, vol. 17, no. 11, p. 3782, 2020.
- [9] N. Saint-Jacques, L. Parker, P. Brown, and T. J. Dummer, "Arsenic in drinking water and urinary tract cancers: a systematic review of 30 years of epidemiological evidence," *Environmental Health*, vol. 13, no. 1, pp. 1–32, 2014.
- [10] M. Ulmanu, E. Marañón, Y. Fernández, L. Castrillón, I. Anger, and D. Dumitriu, "Removal of copper and cadmium ions from diluted aqueous solutions by low cost and waste material adsorbents," *Water, Air, and Soil Pollution*, vol. 142, no. 1, pp. 357–373, 2003.
- [11] S. Wang and Y. Peng, "Natural zeolites as effective adsorbents in water and wastewater treatment," *Chemical Engineering Journal*, vol. 156, no. 1, pp. 11–24, 2010.
- [12] S. E. Bailey, T. J. Olin, R. M. Bricka, and D. D. Adrian, "A review of potentially low-cost sorbents for heavy metals," *Water Research*, vol. 33, no. 11, pp. 2469–2479, 1999.
- [13] M. Boehler, B. Zwickenpflug, J. Hollender, T. Ternes, A. Joss, and H. Siegrist, "Removal of micropollutants in municipal wastewater treatment plants by powder-activated carbon," *Water Science and Technology*, vol. 66, no. 10, pp. 2115–2121, 2012.
- [14] R. Chikri, N. Elhadiri, M. Benchanaa, and Y. el maguana, "Efficiency of sawdust as low-cost adsorbent for dyes removal," *Journal of Chemistry*, vol. 2020, Article ID 8813420, 17 pages, 2020.
- [15] R. T. Yang, *Adsorbents: Fundamentals and Applications*, John Wiley & Sons, 2003.
- [16] L. F. de Magalhães, G. R. da Silva, and A. E. C. Peres, "Zeolite application in wastewater treatment," *Adsorption Science & Technology*, vol. 2022, article 4544104, pp. 1–26, 2022.
- [17] P. Misaelides, "Application of natural zeolites in environmental remediation: a short review," *Microporous and Mesoporous Materials*, vol. 144, no. 1-3, pp. 15–18, 2011.
- [18] M. Moshoeshoe, M. S. Nadiye-Tabbiruka, and V. Obuseng, "A review of the chemistry, structure, properties and applications of zeolites," *Am. J. Mater. Sci.*, vol. 7, no. 5, pp. 196–221, 2017.
- [19] E. Koudelková, Y. Ghrib, F. S. de Oliveira Ramos, P. Čičmanec, and R. Bulánek, "Adsorption and separation of the C3 hydrocarbons on cationic FER zeolites: effect of dual sites existence," *Microporous and Mesoporous Materials*, vol. 279, pp. 416–422, 2019.
- [20] S. Kesraoui-Ouki, C. R. Cheeseman, and R. Perry, "Natural zeolite utilisation in pollution control: a review of applications to metals' effluents," *Journal of Chemical Technology & Biotechnology: International Research in Process, Environmental AND Clean Technology*, vol. 59, no. 2, pp. 121–126, 1994.
- [21] M. W. Ackley, S. U. Rege, and H. Saxena, "Application of natural zeolites in the purification and separation of gases," *Microporous and Mesoporous Materials*, vol. 61, no. 1-3, pp. 25–42, 2003.
- [22] M. Servatan, P. Zarrintaj, G. Mahmodi et al., "Zeolites in drug delivery: progress, challenges and opportunities," *Drug Discovery Today*, vol. 25, no. 4, pp. 642–656, 2020.
- [23] J. Zhang, R. Singh, and P. A. Webley, "Alkali and alkaline-earth cation exchanged chabazite zeolites for adsorption based CO₂ capture," *Microporous and Mesoporous Materials*, vol. 111, no. 1-3, pp. 478–487, 2008.
- [24] W. M. Meier, D. H. Olson, and C. Baerlocher, "Atlas of Zeolite Structure Types," *Zeolites*, vol. 17, no. (1-2), 1996.
- [25] J. V. Smith, "Topochemistry of zeolites and related materials. 1. Topology and geometry," *Chemical Reviews*, vol. 88, no. 1, pp. 149–182, 1988.
- [26] S. Kesraoui-Ouki, C. Cheeseman, and R. Perry, "Effects of conditioning and treatment of chabazite and clinoptilolite prior to lead and cadmium removal," *Environmental Science & Technology*, vol. 27, no. 6, pp. 1108–1116, 1993.
- [27] S. M. Yakout and E. H. Borai, "Adsorption behavior of cadmium onto natural chabazite: batch and column investigations," *Desalination and Water Treatment*, vol. 52, no. 22-24, pp. 4212–4222, 2014.
- [28] S. K. Ouki and M. Kavannagh, "Performance of natural zeolites for the treatment of mixed metal-contaminated effluents," *Waste Management & Research*, vol. 15, no. 4, pp. 383–394, 1997.
- [29] E. Erdem, N. Karapinar, and R. Donat, "The removal of heavy metal cations by natural zeolites," *Journal of Colloid and Interface Science*, vol. 280, no. 2, pp. 309–314, 2004.

- [30] G. Galamini, G. Ferretti, V. Medoro, N. Tesaro, B. Faccini, and M. Coltorti, "Isotherms, kinetics, and thermodynamics of NH_4^+ adsorption in raw liquid manure by using natural chabazite zeolite-rich tuff," *Water*, vol. 12, no. 10, p. 2944, 2020.
- [31] R. Leyva-Ramos, J. E. Monsivais-Rocha, A. Aragon-Piña et al., "Removal of ammonium from aqueous solution by ion exchange on natural and modified chabazite," *Journal of Environmental Management*, vol. 91, no. 12, pp. 2662–2668, 2010.
- [32] D. Caputo and F. Pepe, "Experiments and data processing of ion exchange equilibria involving Italian natural zeolites: a review," *Microporous and Mesoporous Materials*, vol. 105, no. 3, pp. 222–231, 2007.
- [33] X. Song, Y. Zhang, X. Cui, F. Liu, and H. Zhao, "Preparation and characterization of chabazite from construction waste and application as an adsorbent for methylene blue," *Adsorption Science & Technology*, vol. 2021, article 9994079, pp. 1–13, 2021.
- [34] J. Wang, H. Zhao, G. Haller, and Y. Li, "Recent advances in the selective catalytic reduction of NO_x with NH_3 on Cu-Chabazite catalysts," *Applied Catalysis B: Environmental*, vol. 202, pp. 346–354, 2017.
- [35] M. I. Gallegos-García, *Modificación química de una zeolita tipo chabazita para la remoción de aniones en solución acuosa*, [Doctoral thesis], UASLP, 2016.
- [36] K. Barczyk, W. Mozgawa, and M. Król, "Studies of anions sorption on natural zeolites," *Spectrochimica Acta Part A: Molecular and Biomolecular Spectroscopy*, vol. 133, pp. 876–882, 2014.
- [37] B. G. Saucedo-Delgado, D. A. De Haro-Del Rio, L. M. González-Rodríguez et al., "Fluoride adsorption from aqueous solution using a protonated clinoptilolite and its modeling with artificial neural network-based equations," *Journal of Fluorine Chemistry*, vol. 204, pp. 98–106, 2017.
- [38] L. Zhu, X. Lv, S. Tong et al., "Modification of zeolite by metal and adsorption desulfurization of organic sulfide in natural gas," *Journal of Natural Gas Science and Engineering*, vol. 69, article 102941, 2019.
- [39] A. T. Ahmed and H. Almohamadi, "Chemical and microstructural studies for using natural zeolite in advanced wastewater treatment," *International journal of Environmental Science and Technology*, pp. 1–8, 2022.
- [40] V. J. Fernandes, A. S. Araujo, R. A. Medeiros et al., "Kinetic parameters of polyethylene degradation by the natural zeolite chabazite," *Journal of Thermal Analysis and Calorimetry*, vol. 56, no. 3, pp. 1279–1282, 1999.
- [41] G. Piccini, M. Alessio, J. Sauer et al., "Accurate adsorption thermodynamics of small alkanes in zeolites. Ab initio theory and experiment for H-chabazite," *The Journal of Physical Chemistry C*, vol. 119, no. 11, pp. 6128–6137, 2015.
- [42] B. R. Florindo, G. L. Catuzo, and L. Martins, "Porosity of CHA zeolite driving the formation of polyaromatic coke species in the methanol to olefins reaction," *Journal of the Brazilian Chemical Society*, vol. 32, pp. 1051–1059, 2021.
- [43] N. Ghasemian, C. Falamaki, and M. Kalbasi, "Clinoptilolite zeolite as a potential catalyst for propane-SCR- NO_x : performance investigation and kinetic analysis," *Chemical Engineering Journal*, vol. 236, pp. 464–470, 2014.
- [44] C. D. R. Oliveira and J. Rubio, "Adsorption of ions onto treated natural zeolite," *Materials Research*, vol. 10, no. 4, pp. 407–412, 2007.
- [45] T. Juzsakova, A. Csavdari, Á. Rédey et al., "Study on the alkylation mechanism of isobutane with 1-butene using environmental friendly catalysts," *Environmental Engineering and Management Journal*, vol. 13, no. 9, pp. 2343–2347, 2014.
- [46] D. R. Corbin, B. F. Burgess, A. J. Vega, and R. D. Farlee, "Comparison of analytical techniques for the determination of silicon and aluminum content in zeolites," *Analytical Chemistry*, vol. 59, no. 22, pp. 2722–2728, 1987.
- [47] D. W. Ming and J. B. Dixon, "Quantitative determination of clinoptilolite in soils by a cation-exchange capacity method," *Clays and Clay Minerals*, vol. 35, no. 6, pp. 463–468, 1987.
- [48] L. A. Bernal-Jácome, L. Olvera-Izaguirre, M. Gallegos García, R. Delgado-Delgado, and M. Á. Espinosa Rodríguez, "Adsorption of lead (II) from aqueous solution using adsorbents obtained from nanche stone (*Byrsonima crassifolia*)," *Journal of the Mexican Chemical Society*, vol. 64, no. 4, pp. 301–315, 2020.
- [49] D. Nityanandi and C. V. Subbhuraam, "Adsorptive removal of Pb (II) ions from aqueous solution using a coir-based product (puresorbe)," *Adsorption Science & Technology*, vol. 24, no. 2, pp. 177–192, 2006.
- [50] U. Wingenfelder, C. Hansen, G. Furrer, and R. Schulin, "Removal of heavy metals from mine waters by natural zeolites," *Environmental Science & Technology*, vol. 39, no. 12, pp. 4606–4613, 2005.
- [51] A. Bedemo, B. S. Chandravanshi, and F. Zewge, "Removal of trivalent chromium from aqueous solution using aluminum oxide hydroxide," *Springerplus*, vol. 5, no. 1, pp. 1–11, 2016.
- [52] M. H. Ehrampoush, M. Miria, M. H. Salmani, and A. H. Mahvi, "Cadmium removal from aqueous solution by green synthesis iron oxide nanoparticles with tangerine peel extract," *Journal of Environmental Health Science and Engineering*, vol. 13, no. 1, pp. 1–7, 2015.
- [53] I. Langmuir, "The adsorption of gases on plane surfaces of glass, mica and platinum," *Journal of the American Chemical Society*, vol. 40, no. 9, pp. 1361–1403, 1918.
- [54] H. M. F. Freundlich, "Over the adsorption in solution," *The Journal of Physical Chemistry*, vol. 57, no. 385471, pp. 1100–1107, 1906.
- [55] R. Sips, "On the structure of a catalyst surface," *The Journal of Chemical Physics*, vol. 16, no. 5, pp. 490–495, 1948.
- [56] Y. Liu, H. Xu, S. F. Yang, and J. H. Tay, "A general model for biosorption of Cd^{2+} , Cu^{2+} and Zn^{2+} by aerobic granules," *Journal of Biotechnology*, vol. 102, no. 3, pp. 233–239, 2003.
- [57] M. Rahman, A. Pal, K. Uddin, K. Thu, and B. B. Saha, "Statistical analysis of optimized isotherm model for maxsorb iii/ethanol and silica gell/water pairs," *Evergreen*, vol. 5, no. 4, pp. 1–12, 2018.
- [58] B. Boulinguiez, P. Le Cloirec, and D. Wolbert, "Revisiting the determination of Langmuir parameters. Application to Tetrahydrothiophene adsorption onto activated carbon," *Langmuir*, vol. 24, no. 13, pp. 6420–6424, 2008.
- [59] R. Leyva-Ramos, A. Jacobo-Azuara, P. E. Diaz-Flores, R. M. Guerrero-Coronado, J. Mendoza-Barron, and M. S. Berber-Mendoza, "Adsorption of chromium(VI) from an aqueous solution on a surfactant-modified zeolite," *Colloids and Surfaces A: Physicochemical and Engineering Aspects*, vol. 330, no. 1, pp. 35–41, 2008.
- [60] O. Amrhar, L. El Gana, and M. Mobarak, "Calculation of adsorption isotherms by statistical physics models: a review,"

- Environmental Chemistry Letters*, vol. 19, no. 6, pp. 4519–4547, 2021.
- [61] D. K. Arkhipenko, G. P. Valueva, and T. N. Moroz, “Determination of the space group of chabazite,” *Journal of Structural Chemistry*, vol. 36, no. 1, pp. 171–174, 1995.
- [62] M. M. Treacy and J. B. Higgins, *Collection of simulated xrd powder patterns for zeolites fifth (5th)*, Elsevier, 5th edition, 2007.
- [63] A. K. Bansiwala, S. S. Rayalu, N. K. Labhasetwar, A. A. Juwarkar, and S. Devotta, “Surfactant-modified zeolite as a slow release fertilizer for phosphorus,” *Journal of Agricultural and Food Chemistry*, vol. 54, no. 13, pp. 4773–4779, 2006.
- [64] A. Mohammadi, B. Bina, A. Ebrahimi, Y. Hajizadeh, M. M. Amin, and H. Pourzamani, “Effectiveness of nanozeolite modified by cationic surfactant in the removal of disinfection by-product precursors from water solution,” *International journal of environmental health engineering*, vol. 1, no. 1, p. 3, 2012.
- [65] M. Osacký, H. Pálková, P. Hudec, A. Czimerová, D. Galusková, and M. Vítková, “Effect of alkaline synthesis conditions on mineralogy, chemistry and surface properties of phillipsite, P and X zeolitic materials prepared from fine powdered perlite by-product,” *Microporous and Mesoporous Materials*, vol. 294, article 109852, 2020.
- [66] M. R. Abukhadra, M. G. Basyouny, A. M. El-Sherbeeney, and M. A. El-Meligy, “The effect of different green alkali modification processes on the clinoptilolite surface as adsorbent for ammonium ions; characterization and application,” *Microporous and Mesoporous Materials*, vol. 300, article 110145, 2020.
- [67] E. Alvarez-Ayuso, A. Garcia-Sánchez, and X. Querol, “Purification of metal electroplating waste waters using zeolites,” *Water Research*, vol. 37, no. 20, pp. 4855–4862, 2003.
- [68] B. E. Alver and M. Sakızci, “Hydrogen (H₂) adsorption on natural and cation-exchanged clinoptilolite, mordenite and chabazite,” *International Journal of Hydrogen Energy*, vol. 44, no. 13, pp. 6748–6755, 2019.
- [69] A. Al-Mamoori, M. Alsalbokh, S. Lawson, A. A. Rownaghi, and F. Rezaei, “Development of bismuth-mordenite adsorbents for iodine capture from off-gas streams,” *Chemical Engineering Journal*, vol. 391, article 123583, 2020.
- [70] A. S. Sheta, A. M. Falatah, M. S. Al-Sewailam, E. M. Khaled, and A. S. H. Sallam, “Sorption characteristics of zinc and iron by natural zeolite and bentonite,” *Microporous and Mesoporous Materials*, vol. 61, no. 1-3, pp. 127–136, 2003.
- [71] T. M. Albayati and K. R. Kalash, “Polycyclic aromatic hydrocarbons adsorption from wastewater using different types of prepared mesoporous materials MCM-41 in batch and fixed bed column,” *Process Safety and Environmental Protection*, vol. 133, pp. 124–136, 2020.
- [72] N. Mori, S. Nishiyama, S. Tsuruya, and M. Masai, “Deactivation of zeolites in n-hexane cracking,” *Applied Catalysis*, vol. 74, no. 1, pp. 37–52, 1991.
- [73] N. A. Atiyah, T. M. Albayati, and M. A. Atiya, “Interaction behavior of curcumin encapsulated onto functionalized SBA-15 as an efficient carrier and release in drug delivery,” *Journal of Molecular Structure*, vol. 1260, article 132879, 2022.
- [74] C. Giampaolo, L. Mengarelli, E. Torracca, and C. Spencer, “Zeolite characterization of “Vico red tuff with black scoria” ignimbrite flow: the extractive district of Civita Castellana (Viterbo, Italy),” *Il Nuovo Cimento B*, vol. 123, pp. 1459–1476, 2008.
- [75] K. M. Ibrahim, H. N. Khoury, and R. Tuffaha, “Mo and Ni removal from drinking water using zeolitic tuff from Jordan,” *Minerals*, vol. 6, no. 4, p. 116, 2016.
- [76] R. M. Barrer, J. A. Davies, and L. V. C. Rees, “Thermodynamics and thermochemistry of cation exchange in chabazite,” *Journal of Inorganic and Nuclear Chemistry*, vol. 31, no. 1, pp. 219–232, 1969.
- [77] Y. Akdeniz and S. Ülkü, “Thermal stability of Ag-exchanged clinoptilolite rich mineral,” *Journal of Thermal Analysis and Calorimetry*, vol. 94, no. 3, pp. 703–710, 2008.
- [78] H. Aysan, S. Edebali, C. Ozdemir, M. C. Karakaya, and N. Karakaya, “Use of chabazite, a naturally abundant zeolite, for the investigation of the adsorption kinetics and mechanism of methylene blue dye,” *Microporous and Mesoporous Materials*, vol. 235, pp. 78–86, 2016.
- [79] J. W. Ward, “The nature of active sites on zeolites: II. Temperature dependence of the infrared spectra of hydrogen Y zeolite,” *Journal of Catalysis*, vol. 9, no. 4, pp. 396–402, 1967.
- [80] E. A. Paukshtis, M. A. Yaranova, I. S. Batueva, and B. S. Bal'zhinimaev, “A FTIR study of silanol nests over mesoporous silicate materials,” *Microporous and Mesoporous Materials*, vol. 288, article 109582, 2019.
- [81] J. B. Uytterhoeven, L. G. Christner, and W. K. Hall, “Studies of the hydrogen held by solids. VIII. The decationated zeolites,” *The Journal of Physical Chemistry*, vol. 69, no. 6, pp. 2117–2126, 1965.
- [82] J. W. Ward, “The nature of active sites on zeolites: III. The alkali and alkaline earth ion-exchanged forms,” *Journal of Catalysis*, vol. 10, no. 1, pp. 34–46, 1968.
- [83] C. Jia, P. Massiani, and D. Barthomeuf, “Characterization by infrared and nuclear magnetic resonance spectroscopies of calcined beta zeolite,” *Journal of the Chemical Society, Faraday Transactions*, vol. 89, no. 19, pp. 3659–3665, 1993.
- [84] R. Silva-Rodrigo, T. López-Goerne, V. Bertin-Mardel, R. Gómez-Romero, and P. Salas-Castillo, “Propiedades ácidas de los catalizadores de Pt-Sn/Al₂O₃ preparados por sol-gel,” *Revista Mexicana de Ingeniería Química*, vol. 4, no. 2, pp. 141–145, 2005.
- [85] C. A. Emeis, “Determination of integrated molar extinction coefficients for infrared absorption bands of pyridine adsorbed on solid acid catalysts,” *Journal of Catalysis*, vol. 141, no. 2, pp. 347–354, 1993.
- [86] J. W. Ward, “The nature of active sites on zeolites: VIII. Rare earth Y zeolite,” *Journal of Catalysis*, vol. 13, no. 3, pp. 321–327, 1969.
- [87] W. Wu and E. Weitz, “Modification of acid sites in ZSM-5 by ion-exchange: an in-situ FTIR study,” *Applied Surface Science*, vol. 316, pp. 405–415, 2014.
- [88] J. L. Stakebake, “Characterization of natural chabazite and 5A synthetic zeolites: part I. Thermal and outgassing properties,” *Journal of Colloid and Interface Science*, vol. 99, no. 1, pp. 41–49, 1984.
- [89] H. G. Stewart, T. D. Humphries, D. A. Sheppard et al., “Ammonium chloride–metal hydride based reaction cycle for vehicular applications,” *Journal of Materials Chemistry A*, vol. 7, no. 9, pp. 5031–5042, 2019.
- [90] G. Gottardi and E. Galli, *Natural Zeolites*, Springer Science & Business Media, 2012.

- [91] M. J. Zamzow, B. R. Eichbaum, K. R. Sandgren, and D. E. Shanks, "Removal of heavy metals and other cations from wastewater using zeolites," *Separation Science and Technology*, vol. 25, no. 13-15, pp. 1555-1569, 1990.
- [92] S. S. Metwally and M. F. Attallah, "Impact of surface modification of chabazite on the sorption of iodine and molybdenum radioisotopes from liquid phase," *Journal of Molecular Liquids*, vol. 290, article 111237, 2019.
- [93] M. I. Panayotova, "Use of zeolite for cadmium removal from wastewater," *Journal of Environmental Science & Health Part A*, vol. 35, no. 9, pp. 1591-1601, 2000.
- [94] B. V. Liengme and W. K. Hall, "Studies of hydrogen held by solids. Part 11.—Interaction of simple olefins and pyridine with decationated zeolites," *Transactions of the Faraday Society*, vol. 62, pp. 3229-3243, 1966.
- [95] R. K. Iler, "The colloid chemistry of silica and silicates," *Soil Science*, vol. 80, no. 1, p. 86, 1955.
- [96] A. Corma, "Catálisis con zeolitas: desde el laboratorio a su aplicación industrial," *Arbor*, vol. 187, no. Extra_1, pp. 83-102, 2011.
- [97] H. L. Jamieson, H. Yin, A. Waller, A. Khosravi, and M. L. Lind, "Impact of acids on the structure and composition of Linde type A zeolites for use in reverse osmosis membranes for recovery of urine-containing wastewaters," *Microporous and Mesoporous Materials*, vol. 201, pp. 50-60, 2015.
- [98] J. Turkevich, F. Nozaki, and D. N. Stamires, "Proc. 3rd Internat. Congress Catalys., Amsterdam, 1964. North-Holland publishing co," *Amsterdam*, vol. 1, pp. 586-599, 1965.
- [99] F. N. Murrieta-Rico, J. Antúnez-García, R. I. Yocupicio-Gaxiola, D. H. Galván, J. C. González, and V. Petranovskii, "Zeolites as initial structures for the preparation of functional materials," *Journal Of Applied Research And Technology*, vol. 20, no. 1, pp. 92-116, 2022.
- [100] F. Yi, D. Xu, Z. Tao et al., "Correlation of Brønsted acid sites and Al distribution in ZSM-5 zeolites and their effects on butenes conversion," *Fuel*, vol. 320, article 123729, 2022.
- [101] D. Kalló, "Applications of natural zeolites in water and wastewater treatment," *Reviews in Mineralogy and Geochemistry*, vol. 45, no. 1, pp. 519-550, 2001.
- [102] P. A. Jacobs and K. U. Leuven, "Acid zeolites: an attempt to develop unifying concepts (P. H. Emmett award address, 1981)," *Catalysis Reviews*, vol. 24, no. 3, pp. 415-440, 1982.
- [103] P. A. Jacobs, W. J. Mortier, and J. B. Uytterhoeven, "Properties of zeolites in relation to their electronegativity: acidity, carboniogenic activity and strength of interaction in transition metal complexes," *Journal of Inorganic and Nuclear Chemistry*, vol. 40, no. 11, pp. 1919-1923, 1978.
- [104] P. A. Jacobs, *Carboniogenic Activity of Zeolites*, Elsevier Scientific Publishing Company, Amsterdam/Oxford/New York, 1977.
- [105] S. Li, A. Zheng, Y. Su et al., "Brønsted/Lewis acid synergy in dealuminated HY zeolite: a combined solid-state NMR and theoretical calculation study," *Journal of the American Chemical Society*, vol. 129, no. 36, pp. 11161-11171, 2007.
- [106] D. Barthomeuf, "Zeolite acidity dependence on structure and chemical environment. Correlations with catalysis," *Materials Chemistry and Physics*, vol. 17, no. 1-2, pp. 49-71, 1987.
- [107] Y. Zeng, H. Woo, G. Lee, and J. Park, "Removal of chromate from water using surfactant modified Pohang clinoptilolite and Haruna chabazite," *Desalination*, vol. 257, no. 1-3, pp. 102-109, 2010.
- [108] R. Ferrer-Luna, *Estudio sobre la estabilización fisicoquímica de metales pesados en suelo contaminado por jales mineros usando zeolita Clinoptilolita*, [Master's thesis], UANL, 2018.
- [109] R. Moreno-Tost, J. Santamaría-González, E. Rodríguez-Castellón et al., "Selective catalytic reduction of nitric oxide by ammonia over Cu-exchanged Cuban natural zeolites," *Applied Catalysis B: Environmental*, vol. 50, no. 4, pp. 279-288, 2004.
- [110] G. Eisenman, "Cation selective glass electrodes and their mode of operation," *Biophysical Journal*, vol. 2, no. 2, pp. 259-323, 1962.
- [111] H. S. Sherry, "The ion-exchange properties of zeolites. I. Univalent ion exchange in synthetic faujasite," *The Journal of Physical Chemistry*, vol. 70, no. 4, pp. 1158-1168, 1966.
- [112] A. Alberti, E. Galli, G. Vezzalini, E. Passaglia, and P. F. Zanazzi, "Position of cations and water molecules in hydrated chabazite. Natural and Na-, Ca-, Sr- and K-exchanged chabazites," *Zeolites*, vol. 2, no. 4, pp. 303-309, 1982.
- [113] M. Calligaris, G. Nardin, L. Randaccio, and P. C. Chiaramonti, "Cation-site location in a natural chabazite," *Acta Crystallographica Section B: Structural Crystallography and Crystal Chemistry*, vol. 38, no. 2, pp. 602-605, 1982.
- [114] F. Pepe, D. Caputo, and C. Colella, "The double selectivity model for the description of ion-exchange equilibria in zeolites," *Industrial & Engineering Chemistry Research*, vol. 42, no. 5, pp. 1093-1097, 2003.
- [115] M. Calligaris and G. Nardin, "Cation site location in hydrated chabazites. Crystal structure of barium- and cadmium-exchanged chabazites," *Zeolites*, vol. 2, no. 3, pp. 200-204, 1982.
- [116] F. Lucolano, D. Caputo, F. Pepe, and C. Colella, "A thermodynamic model of chabazite selectivity for Pb^{2+} ," in *Studies in Surface Science and Catalysis*, vol. 155, pp. 339-346, Elsevier, 2005.
- [117] E. Torracca, P. Galli, M. Pansini, and C. Colella, "Cation exchange reactions of a sedimentary chabazite," *Microporous and Mesoporous Materials*, vol. 20, no. 1-3, pp. 119-127, 1998.
- [118] S. S. Alkurdi, R. A. Al-Juboori, J. Bundschuh, L. Bowtell, and A. Marchuk, "Inorganic arsenic species removal from water using bone char: a detailed study on adsorption kinetic and isotherm models using error functions analysis," *Journal of Hazardous Materials*, vol. 405, article 124112, 2021.
- [119] A. Günay, E. Arslankaya, and I. Tosun, "Lead removal from aqueous solution by natural and pretreated clinoptilolite: adsorption equilibrium and kinetics," *Journal of Hazardous Materials*, vol. 146, no. 1-2, pp. 362-371, 2007.
- [120] V. Hernández-Montoya, M. A. Pérez-Cruz, D. I. Mendoza-Castillo, M. R. Moreno-Virgen, and A. Bonilla-Petriciolet, "Competitive adsorption of dyes and heavy metals on zeolitic structures," *Journal of Environmental Management*, vol. 116, pp. 213-221, 2013.
- [121] T. Guimarães, L. D. Paquini, B. R. L. Ferraz, L. P. R. Profeti, and D. Profeti, "Efficient removal of Cu(II) and Cr(III) contaminants from aqueous solutions using marble waste powder," *Journal of Environmental Chemical Engineering*, vol. 8, no. 4, article 103972, 2020.
- [122] É. C. Lima, M. H. Dehghani, A. Guleria et al., "Adsorption: fundamental aspects and applications of adsorption for

- effluent treatment," *In Green Technologies for the Defluoridation of Water*, Elsevier, pp. 41–88, 2021.
- [123] M. I. Panayotova, "Kinetics and thermodynamics of copper ions removal from wastewater by use of zeolite," *Waste Management*, vol. 21, no. 7, pp. 671–676, 2001.
- [124] M. Arshadi, M. J. Amiri, and S. Mousavi, "Kinetic, equilibrium and thermodynamic investigations of Ni(II), Cd(II), Cu(II) and Co(II) adsorption on barley straw ash," *Water Resources And Industry*, vol. 6, pp. 1–17, 2014.
- [125] Y. He, L. Zhang, X. An, G. Wan, W. Zhu, and Y. Luo, "Enhanced fluoride removal from water by rare earth (La and Ce) modified alumina: adsorption isotherms, kinetics, thermodynamics and mechanism," *Science of the Total Environment*, vol. 688, pp. 184–198, 2019.
- [126] M. B. Baskan and A. Pala, "Removal of arsenic from drinking water using modified natural zeolite," *Desalination*, vol. 281, pp. 396–403, 2011.
- [127] M. P. Elizalde-González, J. Mattusch, W. D. Einicke, and R. Wennrich, "Sorption on natural solids for arsenic removal," *Chemical Engineering Journal*, vol. 81, no. 1-3, pp. 187–195, 2001.
- [128] G. C. Velazquez-Peña, M. Solache-Ríos, M. T. Olguin, and C. Fall, "As(V) sorption by different natural zeolite frameworks modified with Fe, Zr and FeZr," *Microporous and Mesoporous Materials*, vol. 273, pp. 133–141, 2019.
- [129] S. Bibi, A. Farooqi, K. Hussain, and N. Haider, "Evaluation of industrial based adsorbents for simultaneous removal of arsenic and fluoride from drinking water," *Journal of Cleaner Production*, vol. 87, pp. 882–896, 2015.
- [130] C. H. Liu, Y. H. Chuang, T. Y. Chen et al., "Mechanism of arsenic adsorption on magnetite nanoparticles from water: thermodynamic and spectroscopic studies," *Environmental Science & Technology*, vol. 49, no. 13, pp. 7726–7734, 2015.
- [131] D. Liu, S. Deng, A. Maimaiti et al., "As(III) and As(V) adsorption on nanocomposite of hydrated zirconium oxide coated carbon nanotubes," *Journal of Colloid and Interface Science*, vol. 511, pp. 277–284, 2018.
- [132] A. T. Khadim, T. M. Albayati, and N. M. C. Saady, "Removal of sulfur compounds from real diesel fuel employing the encapsulated mesoporous material adsorbent Co/MCM-41 in a fixed-bed column," *Microporous and Mesoporous Materials*, vol. 341, article 112020, 2022.
- [133] C. Sentorun-Shalaby, S. K. Saha, X. Ma, and C. Song, "Mesoporous-molecular-sieve-supported nickel sorbents for adsorptive desulfurization of commercial ultra-low-sulfur diesel fuel," *Applied Catalysis B: Environmental*, vol. 101, no. 3-4, pp. 718–726, 2011.
- [134] C. L. Chuang, M. Fan, M. Xu et al., "Adsorption of arsenic(V) by activated carbon prepared from oat hulls," *Chemosphere*, vol. 61, no. 4, pp. 478–483, 2005.
- [135] J. Zhu, Z. Lou, Y. Liu, R. Fu, S. A. Baig, and X. Xu, "Adsorption behavior and removal mechanism of arsenic on graphene modified by iron–manganese binary oxide (FeMnO_x/RGO) from aqueous solutions," *RSC advances*, vol. 5, no. 83, pp. 67951–67961, 2015.
- [136] M. Kragović, A. Daković, Ž. Sekulić et al., "Removal of lead from aqueous solutions by using the natural and Fe(III)-modified zeolite," *Applied Surface Science*, vol. 258, no. 8, pp. 3667–3673, 2012.
- [137] W. Mozgawa and T. Bajda, "Spectroscopic study of heavy metals sorption on clinoptilolite," *Physics and Chemistry of Minerals*, vol. 31, no. 10, pp. 706–713, 2005.
- [138] C. Liu, H. H. Ngo, and W. Guo, "Watermelon rind: agrowaste or superior biosorbent?," *Applied Biochemistry and Biotechnology*, vol. 167, no. 6, pp. 1699–1715, 2012.
- [139] R. Leyva-Ramos, M. S. Berber Mendoza, J. Mendoza Barrón, and A. Aragón Piña, "Intercambio iónico de Pb (II) en solución acuosa sobre clinoptilolita modificada por intercambio catiónico," *Revista de la Sociedad Química de México*, vol. 48, no. 2, pp. 130–136, 2004.
- [140] Y. Lv, B. Ma, Y. Liu, C. Wang, and Y. Chen, "Adsorption behavior and mechanism of mixed heavy metal ions by zeolite adsorbent prepared from lithium leach residue," *Microporous and Mesoporous Materials*, vol. 329, article 111553, 2022.
- [141] C. G. Lee, J. W. Jeon, M. J. Hwang et al., "Lead and copper removal from aqueous solutions using carbon foam derived from phenol resin," *Chemosphere*, vol. 130, pp. 59–65, 2015.
- [142] S. Jangkorn, S. Youngme, and P. Praipipat, "Comparative lead adsorptions in synthetic wastewater by synthesized zeolite A of recycled industrial wastes from sugar factory and power plant," *Heliyon*, vol. 8, no. 4, p. e09323, 2022.
- [143] L. Rozumová, O. Životský, J. Seidlerová, O. Motyka, I. Šafařík, and M. Šafaříková, "Magnetically modified peanut husks as an effective sorbent of heavy metals," *Journal of Environmental Chemical Engineering*, vol. 4, no. 1, pp. 549–555, 2016.
- [144] Y. H. Li, S. Wang, Z. Luan, J. Ding, C. Xu, and D. Wu, "Adsorption of cadmium(II) from aqueous solution by surface oxidized carbon nanotubes," *Carbon*, vol. 41, no. 5, pp. 1057–1062, 2003.
- [145] M. R. Panuccio, A. Sorgonà, M. Rizzo, and G. Cacco, "Cadmium adsorption on vermiculite, zeolite and pumice: batch experimental studies," *Journal of Environmental Management*, vol. 90, no. 1, pp. 364–374, 2009.
- [146] H. Javadian, F. Ghorbani, H. A. Tayebi, and S. H. Asl, "Study of the adsorption of cd (II) from aqueous solution using zeolite-based geopolymer, synthesized from coal fly ash; kinetic, isotherm and thermodynamic studies," *Arabian Journal of Chemistry*, vol. 8, no. 6, pp. 837–849, 2015.
- [147] G. Buema, N. Lupu, H. Chiriac et al., "Performance assessment of five adsorbents based on fly ash for removal of cadmium ions," *Journal of Molecular Liquids*, vol. 333, article 115932, 2021.
- [148] D. Mohan and K. P. Singh, "Single-and multi-component adsorption of cadmium and zinc using activated carbon derived from bagasse an agricultural waste," *Water Research*, vol. 36, no. 9, pp. 2304–2318, 2002.
- [149] F. Sardella, M. Gimenez, C. Navas, C. Morandi, C. Deiana, and K. Sapag, "Conversion of viticultural industry wastes into activated carbons for removal of lead and cadmium," *Journal of Environmental Chemical Engineering*, vol. 3, no. 1, pp. 253–260, 2015.
- [150] D. Aggarwal, M. Goyal, and R. C. Bansal, "Adsorption of chromium by activated carbon from aqueous solution," *Carbon*, vol. 37, no. 12, pp. 1989–1997, 1999.
- [151] P. Manechakr and S. Mongkollertlop, "Investigation on adsorption behaviors of heavy metal ions (Cd²⁺, Cr³⁺, Hg²⁺ and Pb²⁺) through low- cost/active manganese dioxide-modified magnetic biochar derived from palm kernel cake

- residue,” *Journal of Environmental Chemical Engineering*, vol. 8, no. 6, article 104467, 2020.
- [152] A. S. K. Kumar, S. J. Jiang, and W. L. Tseng, “Effective adsorption of chromium (VI)/Cr (III) from aqueous solution using ionic liquid functionalized multiwalled carbon nanotubes as a super sorbent,” *Journal of Materials Chemistry A*, vol. 3, no. 13, pp. 7044–7057, 2015.
- [153] X. Liu, Y. Zhang, Y. Liu, and T. Zhang, “Green method to synthesize magnetic zeolite/chitosan composites and adsorption of hexavalent chromium from aqueous solutions,” *International Journal of Biological Macromolecules*, vol. 194, pp. 746–754, 2022.
- [154] M. Liu, T. Wen, X. Wu et al., “Synthesis of porous Fe₃O₄ hollow microspheres/graphene oxide composite for Cr (VI) removal,” *Dalton Transactions*, vol. 42, no. 41, pp. 14710–14717, 2013.
- [155] A. S. K. Kumar, S. S. Kakan, and N. Rajesh, “A novel amine impregnated graphene oxide adsorbent for the removal of hexavalent chromium,” *Chemical Engineering Journal*, vol. 230, pp. 328–337, 2013.
- [156] L. Zheng, Z. Dang, X. Yi, and H. Zhang, “Equilibrium and kinetic studies of adsorption of Cd(II) from aqueous solution using modified corn stalk,” *Journal of Hazardous Materials*, vol. 176, no. 1-3, pp. 650–656, 2010.